Active and Passive Mid-infrared Photonic Devices in ZnSe Based Materials

John Robert Macdonald BSc (Hons.)

Submitted for the degree of Doctor of Philosophy

Institute of Photonics and Quantum Sciences

School of Engineering and Physical Sciences

Heriot-Watt University

May – 2013

Abstract

The work described in this thesis details the development of mid-infrared waveguide laser sources created through the fabrication of waveguide structures in Cr^{2+}: ZnSe using ultrafast laser inscription (ULI). Current quantum cascade laser (QCL) technology in the 2 – 5 µm region offer compact and robust sources suited to use outside the laboratory but the technology does not offer the high average powers, >100 mW, and wide tuneability, 2 – 3.3 µm of Cr^{2+}: ZnSe laser sources. The development of a Cr^{2+}: ZnSe waveguide laser source provides an environmentally robust product with access to powers and tuneable ranges greater than that provided by QCL systems.

The first phase of the investigation produced the first successful refractive index modification of ZnSe using ULI. Both positive and negative refractive index changes were achieved and utilised to fabricate a range of waveguides in ZnSe and Cr^{2+}: ZnSe. Low loss near-infrared waveguides were demonstrated through exploitation of the positive refractive index change. Low loss mid-infrared depressed cladding waveguides were subsequently demonstrated utilising the negative refractive index change. These waveguides were characterised at wavelengths of 1928, 2300 and 3390 nm as representative of pump and signal wavelengths in Cr^{2+}: ZnSe laser systems.

Finally, the newly fabricated Cr^{2+}: ZnSe waveguides were constructed into waveguide laser cavities and pumped with a thulium fibre laser source operating at 1928 nm. Laser operation is demonstrated in both waveguides devices at wavelengths of 2573 and 2486 nm with a maximum achieved output power of 285 mW and a slope efficiency of 45%. Furthermore, a tuneable laser source is constructed in the Littman-Metcalf configuration exhibiting a maximum tuning range of 510 nm, 2330-2840 nm, with output powers exceeding 25 mW across the full range.

These waveguide laser devices offer an environmentally robust and compact source in the 2 – 3 µm region with improvements upon maximum power and tuneability ranges in current quantum cascade laser sources. The waveguide laser sources reported open the door to products offering the robust nature of QCL sources with the higher powers and 2 – 3 µm tuneability associated with current bulk Cr^{2+}: ZnSe laser systems.

Acknowledgements

Firstly, I would like to thank my supervisor, Professor Ajoy Kar, for his continuing support and advice throughout my PhD. Without his guidance this would certainly not have been possible and his enthusiasm has made the experience all the more enjoyable.

I thank EPSRC for my studentship which provided the means for me to undertake this work.

I would also like to thank all the members of the Nonlinear Optics Group over the past four years. In particular: Robert Thomson, Nicholas Psaila and Graeme Brown for the training they provided in ULI; Henry Bookey and John McCarthy for all the help provided with various mid-infrared sources and equipment; and Stephen Beecher for answering a long list of questions about physics, electronics and coffee. I am indebted to Debaditya Choudhury for all his assistance in making the group visits to India so memorable.

Sincere thanks to Patrick Berry and Kenneth Schepler at Air Force Research Laboratory, WPAFB, USA for many useful discussions and the Cr^{2+}: ZnSe samples. Their knowledge on transition metal doped II-VI semiconductors has been invaluable during the course of my PhD.

My thanks go to all the Heriot-Watt technical staff, specifically Neil Ross, Peter Heron and Mark Stewart for the dicing of material substrates and the endless number of optomechanical parts they produced on short notice. So many of the experiments performed over the course of my work would not have progressed without their skills.

My family, especially my parents Lorna and Ian Macdonald, deserve special thanks for their encouragement before and throughout my PhD. My holidays home to Arran have always been a vital form of respite. I would not have made it this far without their help.

My time at Heriot-Watt would not have been the same without my officemates. I thank John McCarthy, Richard Carter and Stephen Beecher for the stimulating chat, whisky tastings and comic relief.

My friends outside of Heriot-Watt deserve heartfelt thanks for offering much needed diversions, in particular Gayle Duggan, Oliver Littlejohn, Michael MacFarlane, Keir Murdo and Stuart Macdonald. I am fortunate that this is in no way an exhaustive list.

Finally, I would like to thank my fiancée Clare for her endless patience, advice and love. I am truly lucky to have someone so special in my life.

Contents

List of abbreviations

AR – Anti-Reflection

BBO – Barium Borate

BIBO – Bismuth Borate

CVD – Chemical Vapour Deposition

CW – Continuous Wave

DFG – Difference Frequency Generation

ECDL – External Cavity Diode Laser

FHD – Flame Hydrolysis

FWHM – Full Width Half Maximum

FWM – Four Wave Mixing

HPCVD – High Pressure Chemical Vapour Deposition

HR – Highly Reflective

IEEE – Institute of Electrical and Electronic Engineers

KGW – Potassium Gadolinium Tungstate

MOPA – Master Oscillator Power Amplifier

MPI – Multi-Photon Ionisation

NA – Numerical Aperture

OPO – Optical Parametric Oscillator

PLD – Pulsed Laser Deposition

PPKTP – Periodically Poled Potassium Titanyl Phosphate

PPLN – Periodically Poled Lithium Niobate

QCL – Quantum Cascade Laser

SHG – Second Harmonic Generation

SLM – Spatial Light Modulator

SPM – Self Phase Modulation

TM – Transition Metal

ULI - Ultrafast Laser Inscription

UV - Ultraviolet

YAG – Yttrium Aluminium Garnet

List of Publications by the Author

Journal Papers

[1] **J. R. Macdonald**, R. R. Thomson, S. J. Beecher, N. D. Psaila, H. T. Bookey, and A. K. Kar, "Ultrafast laser inscription of near-infrared waveguides in polycrystalline ZnSe," Opt. Lett. 35, 4036-4038 (2010).

[2] A. Rodenas, A. Benayas, **J. R. Macdonald**, J. Zhang, D. Y. Tang, D. Jaque, and A. K. Kar, "Direct laser writing of near-IR step-index buried channel waveguides in rare earth doped YAG," *Opt. Lett.*, **36**. 3395-3397, (2011).

[3] Y. Ren, N. Dong, **J. Macdonald**, F. Chen, H. Zhang, and A. K. Kar, "Continuous wave channel waveguide lasers in Nd:LuVO4 fabricated by direct femtosecond laser writing," *Opt. Express*, **20**, 1969-1974 (2012).

[4] **J. R. Macdonald**, S. J. Beecher, P. A. Berry, K. L. Schepler and A. K. Kar, "Compact Mid-infrared Cr: ZnSe Channel Waveguide Laser," *Applied Physics Letters*, **102**, 161110 (2013).

Conference Papers

[1] **J. R. Macdonald**, R. R Thomson, N. D. Psaila, S. J. Beecher, H. T. Bookey and A. K. Kar, "Ultrafast laser inscription of low loss waveguides in polycrystalline ZnSe," in IEEE Photonics Society, 23rd Annual Meeting 2010, pp.56-57.

[2] P. Berry, **J. Macdonald**, A. Kar, and K. Schepler, "Ultrafast Laser Inscription of Waveguide Structures in Cr^{2+}:ZnSe," in Advances in Optical Materials, Istanbul, Turkey, (Optical Society of America, 2011), paper AIFB5.

[3] **J. R. Macdonald**, P. A. Berry, K. L. Schelper, and A. Kar, "Directly Written Mid-Infrared Waveguides in Zinc Selenide," in Advances in Optical Materials, San Diego, USA, (Optical Society of America, 2012), paper IF1A.3.

List of Figures

Chapter 1 – Introduction

1.1 Background

The invention of the laser in 1960 [1] provided access to a new coherent light source which has since played a significant role in wide range of scientific and technological fields. These unique light sources have had a profound impact on the world we live in through technologies such as laser material processing, fibre optic communication networks, laser spectroscopy and laser surgery to name but a few. In fact, lasers have been so successful as to also enter our everyday lives in a number of commercial products including DVD and BluRay players, fibre optic broadband and laser printers. Over the last 50 years, a variety of laser sources have emerged covering a broad but far from exhaustive range of the electromagnetic spectrum.

Following the first ruby laser operating in the visible range of the spectrum, the number of sources grew rapidly with gas, fibre, dye and semiconductor lasers emerging. By the 1990s there was a wide range of sources across the visible and near infrared utilising rare earth doped glasses and crystals as well as an array of semiconductor sources. The mid-infrared region (2 – 12 μm) of the electromagnetic spectrum is of particular interest to applications in laser spectroscopy and remote sensing due to the location of absorption lines of many organic and inorganic molecules, known as the molecular fingerprint region. However, at wavelengths beyond the near infrared few sources existed beyond lead salt lasers, which required cryogenic cooling, and a sparse collection of gas lasers such as CO_2, CO and HeNe.

With the advent of the quantum cascade laser (QCL) [2], a range of custom mid-infrared laser sources became available, suitable for a host of applications in remote sensing and spectroscopy. This includes medical applications in breath analysis, environmental applications such as pollutant detection and defence interests in explosives detection. Latterly in 2002, the realisation of a QCL capable of operating with continuous wave (CW) output at room temperature [3], served to increase their suitability to spectroscopy applications outside of the laboratory.

Advances in QCL technology have brought increased accessibility to a wide variety of new sources in the mid-infrared. However, the technology offers limited availability of widely tuneable sources at high average powers > 100 mW, especially in the 2 – 5 μm range [4, 5]. An exciting technology explored for this wavelength range was mid-infrared transition metal (TM) ion lasers. An early example of this is the Co^{2+}: MgF_2 laser which demonstrated room temperature operation from 1.75 to 2.50 μm [6, 7]. Unfortunately, these lasers offered few practical benefits with small emission cross-sections and high non-radiative decay [6]. However, TM ion sources came of age with the development of TM ion doped II-VI semiconductors [8]. A selection of sources utilising Co^{2+}, Cr^{2+}, Ni^{2+} and Fe^{2+} in substrates such as ZnSe, ZnTe, CdSe, ZnS and $Cd_{1-x}Mn_xTe$ were demonstrated [8-10]. To date, these gain media have produced sources covering 1.9 – 5.5 μm, each with gain bandwidths spanning approximately 1 micron [11-14] and offering continuous tuneability with power outputs over 100 mW across the wavelength range. Indeed many sources have achieved output powers in excess of 10 W [15] and commercial products are now readily available [16]. These bulk systems lack the robust nature of QCLs and various research groups continue to research compact and more vibration insensitive solutions such as fibre and waveguide geometry [17-19].

1.1.1 Ultrafast laser inscription of waveguides

Arguably the most prominent example of a dielectric waveguide is the optical fibre, the use of which now forms the backbone of modern telecommunication systems. The key principle of a waveguide, such as an optical fibre, lies at the ability to ‘guide’ light along the structure’s length whilst maintaining the electric field distribution. Optical fibres rose to prominence in the 1960s through the work of Charles Kao and George Hockham which theorised that optical fibres could be realised with less than 20 $dB \cdot km^{-1}$ attenuation making them suitable for telecommunications [20]. This was soon realised by Corning® in 1970 with a 17 $dB \cdot km^{-1}$ attenuation optical fibre and since then performance has improved to achieve attenuations of under 0.2 $dB \cdot km^{-1}$ [21]. These advances led to Charles Kao receiving a share of the Nobel Prize for Physics in 2009 [22].

Parallel to these advances in optical fibres came the development of integrated optical devices utilising waveguide technology [23, 24]. This early integrated optical technology relied on waveguides in thin film structures and as the technology matured more complex optical circuitry has been developed through a number of techniques. The wide variety of techniques that have emerged for the fabrication of waveguide structures includes thin film deposition techniques such as; Flame Hydrolysis Deposition (FHD), Chemical Vapour Deposition (CVD) and Pulsed Laser Deposition (PLD). Photo-lithographic techniques can then be employed to achieve the desired waveguide structures, however ion exchange or in-diffusion techniques are also well established methods for defining the ultimate waveguide structure [25].

Direct-write fabrication of waveguides has also been well established as a waveguide fabrication technique. CW direct-write technology typically employs an ultraviolet (UV) laser with a photosensitive substrate material which under UV irradiation induces an increase in material refractive index at the surface of the substrate. With the more recent proliferation of ultrafast laser systems such as the Ti: Sapphire laser, a new technique for directly written waveguides has been developed in ultrafast laser inscription. Since the first demonstration in 1996 by Davis *et al.* [26], ULI has emerged as a powerful and flexible tool for the fabrication of integrated optical devices. Ultrashort pulses are focused below the surface of a transparent material substrate, inducing nonlinear absorption processes inside the bulk material resulting in an energy transfer to the material lattice. Under the correct conditions and with careful control of the inscription laser parameters this energy transfer may manifest as a refractive index change. In turn, the sample can be translated through the laser focus in order to inscribe a waveguide structure. Early work predominantly employed regeneratively amplified Ti: Sapphire sources operating at short pulse durations of approximately 100 fs and low repetition rates of 1-5 kHz [27, 28]. However, with the increased availability of short pulse mode-locked fibre laser systems higher repetition rates have been more commonly utilised and inscription of low loss waveguides with longer pulse durations of 300-700 fs have been demonstrated [29-31]. Unlike the other techniques described above, ULI offers fabrication of truly 3 dimensional structures making it suitable for integration with modern multi-core fibre geometry [32]. The ability to fabricate subsurface structures allows this 3-D technology to create structures of arbitrary

cross-sections making it a powerful tool for the development of a range of photonic devices. In addition to this unique capability, ULI offers fabrication without cleanroom facilities and the maskless processing lends itself to rapid prototyping of devices.

1.2 Thesis outline

Chapter 2 provides an introduction to the technology of ultrafast laser inscription. The key nonlinear effects present in ultrafast laser inscription are specified, along with a description of the required experimental setup and details of laser systems used throughout this body of work. Finally, the development of the field is discussed with some examples of the applications of ultrafast laser inscription.

Chapter 3 presents the initial experiments in the application of ultrafast laser inscription in ZnSe substrates. The challenges associated with fabricating ULI devices in highly nonlinear materials are detailed. In particular, the role of pulse duration is investigated and treated as a key parameter in the inscription. The first channel waveguides fabricated in ZnSe by ULI are reported and characterised in the near infrared at 800 nm and 1550 nm. Single mode guiding is demonstrated at both wavelengths with propagation losses of 1.1 dB $\cdot cm^{-1}$ at 1550 nm.

Chapter 4 reports the fabrication of mid-infrared waveguides in ZnSe using ultrafast laser inscription. A broad investigation into inscription parameters is described and a localised reduction in the refractive index of ZnSe is demonstrated. The manipulation of the refractive index of ZnSe is presented through a direct comparison of structures utilising positive and negative index changes respectively. Fabrication of mid-infrared waveguides in ZnSe is then achieved through inscription of a cladding region of reduced refractive index. The waveguides are characterised in the mid-infrared with near single mode performance achieved at 1928 and 3390 nm.

Chapter 5 provides an introduction into transition metal doped II-VI semiconductors with a specific focus on Cr^{2+}: ZnSe. The inscription technology applied in ZnSe is developed for successful fabrication in Cr^{2+}: ZnSe and used to develop depressed cladding structures with a double clad architecture. Also described is the development of a mid-infrared circular cross-section depressed cladding waveguide with a range of

diameters spanning 80 – 160 µm. Finally, device characterisation in the mid-infrared at 1928, 2300 and 3390 nm is presented.

Chapter 6 reports the first channel waveguide laser in Cr^{2+}: ZnSe. The mid-infrared waveguides outlined in Chapter 5 are built into compact laser cavities. Laser performance utilising the double clad Cr^{2+}: ZnSe waveguide is detailed before improved performance is demonstrated using the circular cross-section waveguide structure. A maximum output power of 285 mW is reported with a slope efficiency of 45%.

Chapter 7 describes the construction of tuneable Cr^{2+}: ZnSe waveguide laser systems. Littrow configuration and Littman-Metcalf configuration external cavity lasers are constructed and the performance of both laser systems is reported. A maximum tuneability range of 510 nm is achieved using the Littman-Metcalf configuration with power output over 20 mW across the tuning range.

Finally, **Chapter 8** presents the conclusions reached for the body of work and proposed future work in this area.

1.2.1 Summary

The overarching aim of the work presented in this thesis was to develop a robust mid-infrared channel waveguide laser fabricated using ultrafast laser inscription (ULI). The work encompasses the development of successful ULI technology in ZnSe before the fabrication of a number of waveguide devices. The challenges of ULI fabrication in highly nonlinear materials are reported and a study into the role of pulse duration in ULI is conducted. The success of ULI fabrication in ZnSe is extended to Cr^{2+}: ZnSe with the development of mid-infrared waveguide structures aimed at providing a suitable mid-infrared waveguide gain medium. Successful mid-infrared waveguide structures were then used to construct waveguide laser cavities and demonstrate mid-infrared laser output. The material processing, laser development and laser characterisation form the main body of work that will be described in this thesis.

Chapter 2 - Ultrafast laser inscription

In order to properly describe the interaction of light with a dielectric medium in a case such as ultrafast laser inscription it is necessary to understand how light propagates in such a medium. The propagation of light in a non-magnetic, non-conducting medium is dictated by Maxwell's equations:

$$\nabla \times E(r,t) = -\frac{\partial B(r,t)}{\partial t} \qquad \textit{Equation 2.1}$$

$$\nabla \times H(r,t) = \frac{\partial D(r,t)}{\partial t} \qquad \textit{Equation 2.2}$$

$$\nabla \cdot B(r,t) = 0 \qquad \textit{Equation 2.3}$$

$$\nabla \cdot D(r,t) = 0 \qquad \textit{Equation 2.4}$$

where *E* is the electric field, *H* is the magnetic field, *D* is the electric flux and *B* is the magnetic flux.

$$D(r,t) = \varepsilon_0 E(r,t) + P(r,t) \qquad \textit{Equation 2.5}$$

$$B(r,t) = \mu_0 H(r,t) \qquad \textit{Equation 2.6}$$

where ε_o is the electric permittivity of free space, P is the polarisation of light and μ_0 is the magnetic permeability of free space. When solved, these equations produce the familiar wave equation for light:

$$\nabla^2 E + \frac{1}{c^2}\frac{\partial^2 E}{\partial t^2} = -\mu_0 \frac{\partial^2 P}{\partial t^2} \qquad \textit{Equation 2.7}$$

where c is the speed of light. In the case of small electric fields, the polarisation vector is linearly related to the electric field, E, by the first order polarisation susceptibility tensor, $\chi^{(1)}$:

$$P = \varepsilon_0 \chi^{(1)} E \qquad \textit{Equation 2.8}$$

However, as the magnitude of an electric field approaches that of the substrate material atomic field the behaviour becomes nonlinear. In order to simplify this we will assume an isotropic medium and work with the scalar terms rather than tensors. From here we can use a Taylor expansion to provide a general description of the nonlinear response with large electric fields:

$$P = \varepsilon_0 (\chi^{(1)} E + \chi^{(2)} E^2 + \chi^{(3)} E^3 \ldots) \qquad \textit{Equation 2.9}$$

where $\chi^{(j)}$ is the j^{th} order susceptibility. In centrosymmetric materials the second order susceptibility is zero and Equation 2.9 can be simplified to the third order as:

$$P = \varepsilon_0 (\chi^{(1)} + \frac{3}{4}\chi^{(3)} |E|^2) E \qquad \textit{Equation 2.10}$$

where $|E|$ is a time average of the electric field. Equation 2.7 can then be simplified using Equation 2.10 and through the relation $c = \sqrt{\frac{1}{\mu\varepsilon}}$ to get:

$$\nabla^2 \mathrm{E} + \frac{\mathrm{n}^2}{\mathrm{c}^2}\frac{\partial^2 \mathrm{E}}{\partial \mathrm{t}^2} = 0 \qquad \textit{Equation 2.11}$$

Where we now define the refractive index as:

$$n = \sqrt{1 - \chi^{(1)} - \frac{3}{4}\chi^{(3)}|E|^2} \qquad \textit{Equation 2.12}$$

and therefore,

$$n = n_0 + n_2 I \qquad \textit{Equation 2.13}$$

The short pulse durations used for ULI generate extremely high peak irradiances when focused, typically greater than 10^{15} W·m^{-2}. As a result the nonlinear properties of the target material become very important. The nonlinear component of the material refractive index, n_2, is particularly influential in the inscription process as its contribution to the material refractive index is proportional to the incident intensity of light as shown in Equation 2.13.

When operating at wavelengths substantially below the material band-gap, as is the case for ULI, the value of n_2 is generally positive. Therefore, a Gaussian beam propagating through a given medium will experience a higher refractive index at the centre of the beam where the intensity is highest. This leads to the formation of a positive lens and as a result the beam experiences "self-focusing". Eventually the beam collapses to a point that produces intensities high enough to cause photo-ionisation. The subsequent plasma generated by this photo-ionisation causes defocusing of the beam and the balancing of these two effects leads to the process known as filamentation [33, 34]. This effect is directly proportional to the beam power and a critical power for the onset of filamentation can be defined as shown in Equation 2.14.

$$P_{Crit} = \frac{\alpha\lambda^2}{4\pi n_0 n_2} \qquad \textit{Equation 2.14}$$

where λ is the laser wavelength and α is a numerically calculated value for the applicable spatial distribution of the beam, 1.8962 for a Gaussian beam [35]. Importantly this critical power does not depend on the size of the beam diameter but only on the peak power of the beam. A larger diameter beam will have a weaker Kerr-lens than a smaller diameter beam of the same power; however, this only contributes to the distance over which the beam is focused and not to the onset of filamentation.

Ultrafast laser inscription (ULI) relies on nonlinear absorption processes in order to transfer energy to a material substrate lattice. Properly controlled this energy transfer can manifest as a localised refractive index change in the substrate. This chapter will introduce the important nonlinear processes and review the ULI system utilised throughout the following body of work.

2.1 Linear and non-linear absorption

A laser source used for ULI has an output wavelength at which the target material is transparent. This means that the energy of the incident photons is not sufficient to promote a valence electron into the conduction band of the material. For this reason, nonlinear processes are required in order for the required energy transfer to occur. This is a key property of ULI and one that is necessary for the fabrication of sub-surface, 3-D structures. Through avoiding linear absorption it is possible to localise absorption to a subsurface point. Figure 2.1, demonstrates how important this is by depicting the difference in material absorption in a linear or non-linear absorption regime.

Figure 2.1. Linear absorption vs nonlinear absorption. The top beam, incident from the right shows fluorescence with a single photon absorption regime whereas the bottom beam incident from the left shows the smaller, point-like fluorescence resulting from a nonlinear2-photon absorption process. Picture taken from B. Amos [36].

It is evident that the linear absorption case has affected much of the target material, whereas the nonlinear 2-photon absorption has allowed a pinpoint of material to be targeted.

2.2 Energy absorption in a transparent medium

An ultrashort laser pulse of sub-band-gap energy propagating through a transparent medium is influenced strongly by the nonlinear properties of the material due to the high irradiances present. This may include processes such as four-wave mixing (FWM), self-phase modulation (SPM) and, perhaps most importantly, self-focusing. Beyond these processes there are further nonlinear phenomena that are responsible for the absorption processes that ULI relies on. The fundamental process is referred to as laser induced breakdown and relies on a photo-ionisation as a means of transferring energy into the material. The initial photo-ionisation effects in ULI can be divided into two categories. The first is multi-photon ionisation, (MPI), and the second is tunnelling ionisation. MPI occurs when an intense electric fields allows the absorption of multiple photons simultaneously in order to promote an electron out of its bound state. Tunnelling ionisation occurs when an intense electric field is comparable to the Coulomb potential experienced by the bound electron, allowing it to tunnel out of the bound state. The preliminary theoretical outline of these photo-ionisation mechanisms was provided in 1964 by Keldysh [37].The model described by Keldysh resulted in the use of a parameter which determines the dominant mechanism for photo-ionisation. This is known as the Keldysh parameter, γ, and is defined by:

$$\gamma = \frac{\omega}{e}\sqrt{\frac{nmc\varepsilon_0 E_g}{I}} \qquad \text{Equation 2.15}$$

where ω is the laser frequency, e is the electron charge, m is the mass of the electron and E_g is the band-gap energy of the material. When $\gamma < 1.5$ the dominant mechanism is tunnelling ionisation and when $\gamma > 1.5$, multi-photon ionisation dominates. There also exists an intermediate state which occurs when $\gamma \approx 1.5$. Each mechanism is illustrated below along with the corresponding Keldysh parameter in Figure 2.2

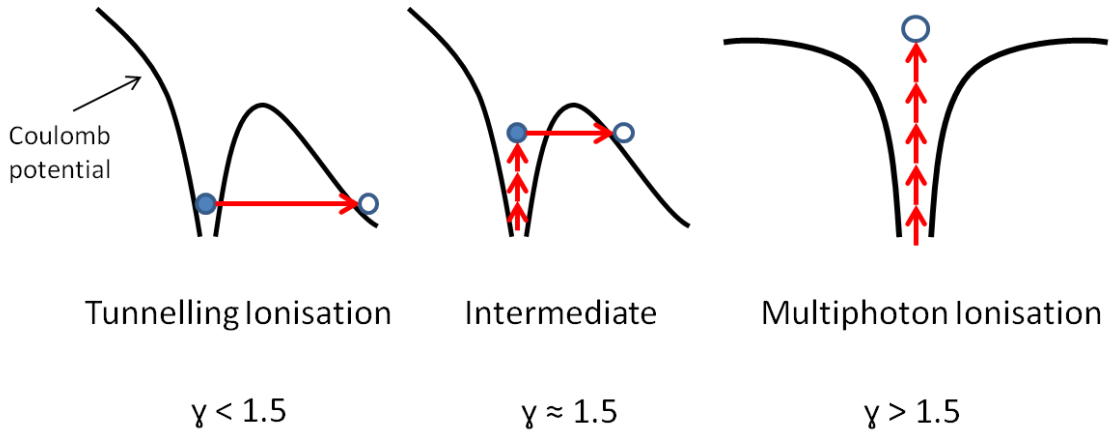

Figure 2.2. Diagrams representing the nonlinear processes that contribute to absorption of an incident ultrafast pulse: (a) Tunnelling ionisation, (b)An intermediate state and (c) Multiphoton ionisation process. The solid blue dots represent a bound electron and the hollow blue dots represent liberated electrons. The black lines represent the Coulomb potential and red arrows depict the action of a photon on an electron.

Another important ionisation process is avalanche ionisation. Once a bound electron has been liberated by one of the photo-ionisation mechanisms described above it is able to absorb energy linearly from the inscription laser. When the electron has sufficient energy, above that of the coulomb potential, it may then liberate another electron through impact ionisation. Whilst under illumination, the liberated electrons can continue to impact ionise other electrons and hence the population of electrons in the conduction band grows exponentially. As this mechanism proceeds through linear absorption the overall process of laser induced breakdown can be seen to be 'seeded' by MPI and/or tunnelling ionisation before being dominated by avalanche ionisation.

2.3 The inscription process

2.3.1 Inscription geometry

The process of ULI most basically employs an ultrafast laser source and a translation stage on which the sample substrate is mounted. There are two geometries in which this can be arranged: longitudinal and transverse.

Longitudinal geometry

In this arrangement the sample is translated along the inscription beam axis, Figure 2.3. This provides a symmetrical beam cross-section along the inscription path and can therefore result in a symmetric waveguide structure. However, the length over which waveguides can be inscribed is limited to the working distance of the lens used. As ULI generally employs high numerical aperture (NA) lenses, this severely limits the maximum length of the resultant structures.

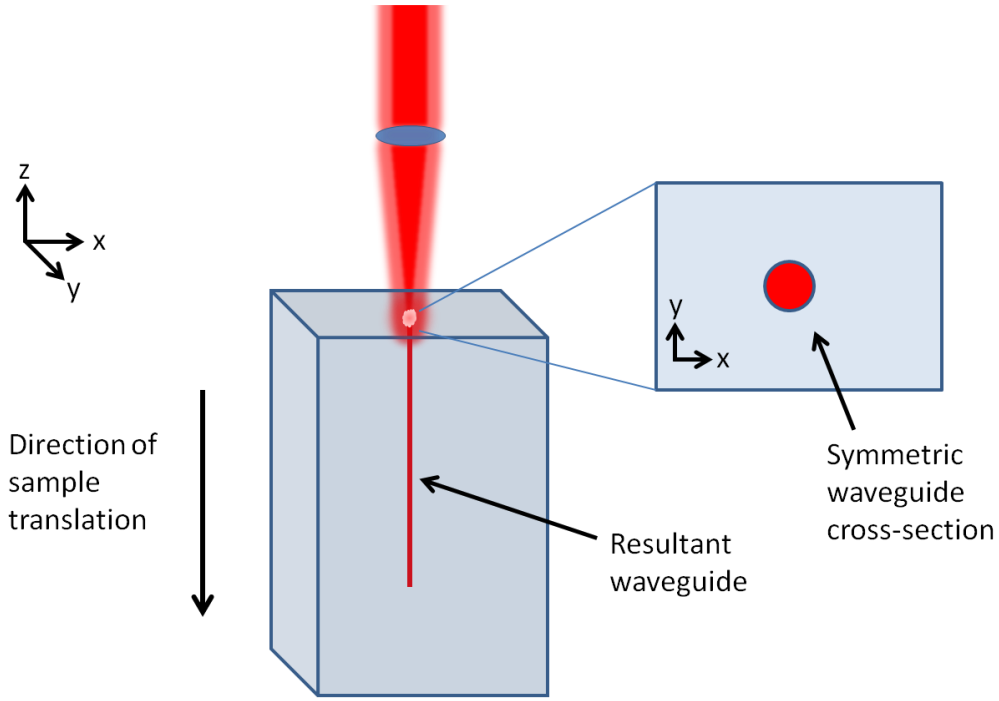

Figure 2.3. Longitudinal inscription geometry in which the waveguide is inscribed by translating the sample along the beam propagation axis. The result is a structure with a symmetric cross-section due to the circular symmetry of the inscription beam about this axis.

Transverse Geometry

In the transverse geometry the sample is translated perpendicularly to the beam propagation axis, as shown in Figure 2.4. This overcomes the restriction in structure length experienced in the longitudinal geometry as the sample can be translated over any distance allowed by the translation stages. However, this geometry results in an asymmetry in the resultant structure cross-section. Unlike the case for longitudinal

geometry the intensity distribution of the inscription beam in the inscription axis is no longer symmetric. For the transverse geometry the intensity distribution of the focal volume is elongated in the beam axis and as such creates a highly asymmetric cross-section for any structure inscribed. This is the case unless the inscription lens used has a high NA (e.g. NA = 1.0) as an increase in NA reduces the asymmetry of the focal volume. Although using a lens of this sort lessens asymmetry, the depth of inscription is severely limited and the scale of the fabricated structures are often too small for the application requirements. It is for these reasons that beam shaping and cross-section manipulation must be employed to achieve more appropriate devices.

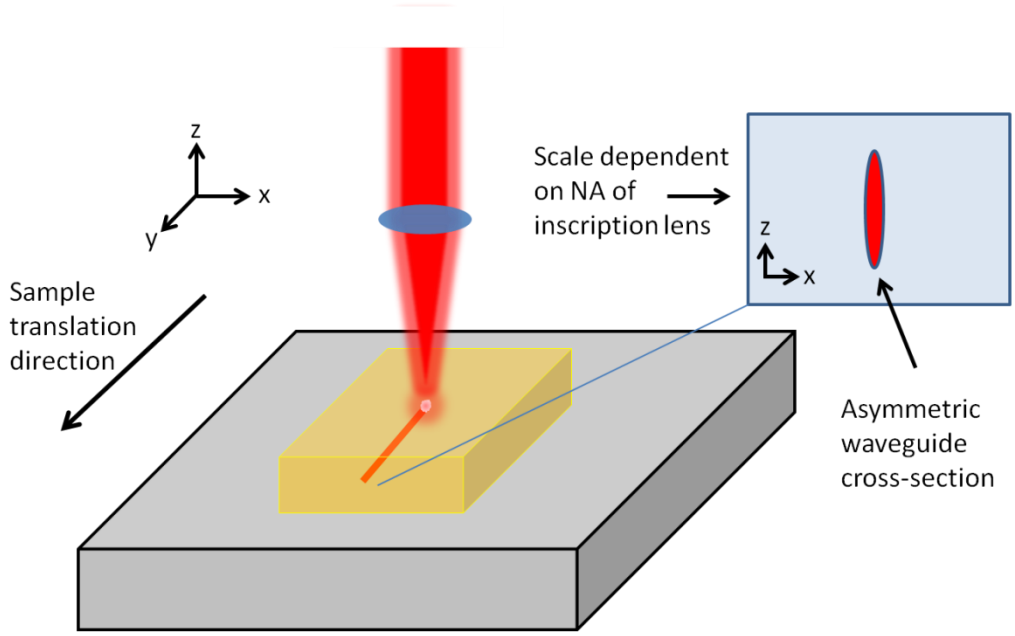

Figure 2.4. Transverse inscription geometry in which the inscription direction is perpendicular to the beam axis. This allows for any inscription length within the maximum movement range of the translation stages. However, in this geometry the inscribed structure cross-section is asymmetric due to the asymmetric intensity distribution of the focal volume in the X-Z plane, this is illustrated in the inset window.

2.3.2 Beam shaping and cross-section manipulation

In order to exploit the benefits of the longitudinal inscription geometry it is necessary to employ beam shaping techniques to compensate for the asymmetry in the focal volume. As ULI depends on nonlinear processes the cross-sectional area of the focal volume will not directly translate to that of the inscribed region. However, it is clear that a large degree asymmetry would still result in an asymmetric structure. Several methods have been investigated and employed by the field in order to compensate for this asymmetry and the main methods are summarised below:

The slit method

Arguably the simplest method, the slit technique was first demonstrated by Cheng *et al.* [38] in 2003 then later applied to waveguide fabrication by Ams *et al.*[39] in 2003, and utilises a slit aperture placed before the inscription lens. Assuming the slit is placed in close proximity to the lens the incident beam will fill the lens in one axis and underfill in the other axis. As a result the two axes experience a different effective NA for the lens. It is therefore possible, through calibration of the slit, to control the shape of the focal volume and correct of any asymmetry. However, this method has limitations in that the asymmetry correction is only applied in one axis and the slit must be adjusted if inscription is required along another axis. This is particularly problematic if the inscribed structure requires any bends reasonably far from the inscription axis as the slit cannot be simply adjusted to accommodate this. Figure 2.5 and 2.6 show the configuration of this system and a model of the focal volume energy distribution for slit adjustment.

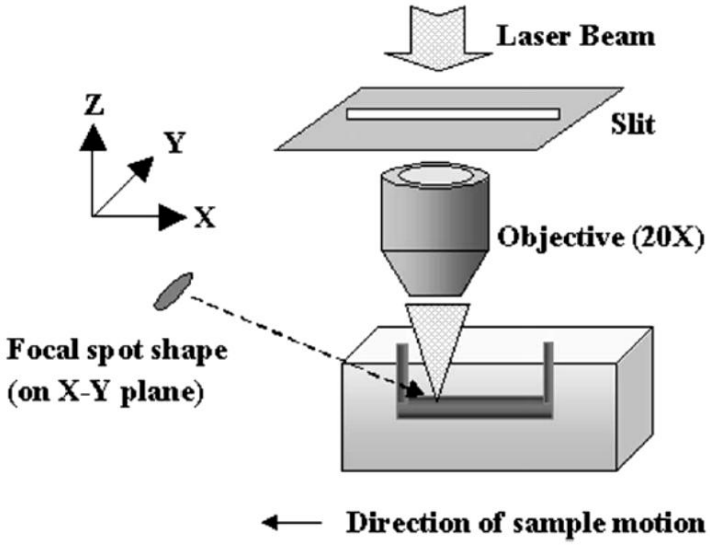

Figure 2.5. Slit method configuration used by Cheng et al. for the inscription of near symmertric cross-section structures.[38]

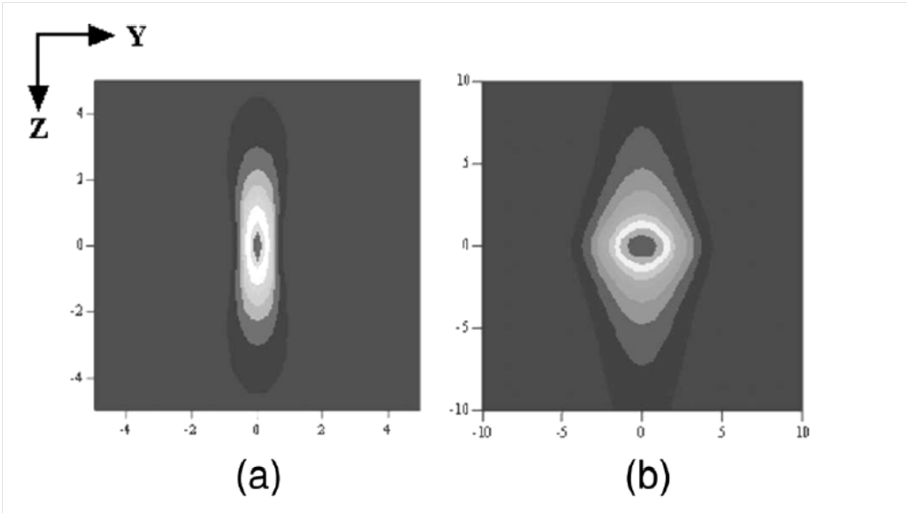

Figure 2.6. Simulation of focal volume energy distribution (a) without slit and (b) with slit. In both cases the inscription beam propagates in the z-axis from above the figures shown. The use of the slit shows an increase in symmetry for the focal volume which is desirable for the fabrication of near symmetrical waveguide structures. Image taken from Cheng et al.[38] The field of view in both images is 20 × 20 µm.

A significant development of the slit technique using a spatial light modulator (SLM) was demonstrated by Salter *et al.* in 2012 [40]. In this case the slit is replaced by an SLM which allows the energy distribution in the focal volume to be controlled by altering the spatial distribution of the beam before the inscription lens. The SLM

performs the same role as the traditional slit aperture but provides the added benefit of being adaptable during the inscription process in order to fabricate bends in the waveguide structure if necessary.

Cylindrical telescope

Demonstrated first by Osellame *et al.*[41], the cylindrical telescope techniques employs two cylindrical lenses in order to correct the focal volume asymmetry. Through altering the distance between the two cylindrical lenses the beam diameter can be changed in the axis perpendicular to the inscription direction. Similarly to the slit method this changes the effective NA of the lens in this axis and so allows a near-symmetric cross-section to be generated in the focal volume after the lens. The apparatus used by Osellame *et al.* for this technique is shown in Figure 2.7.

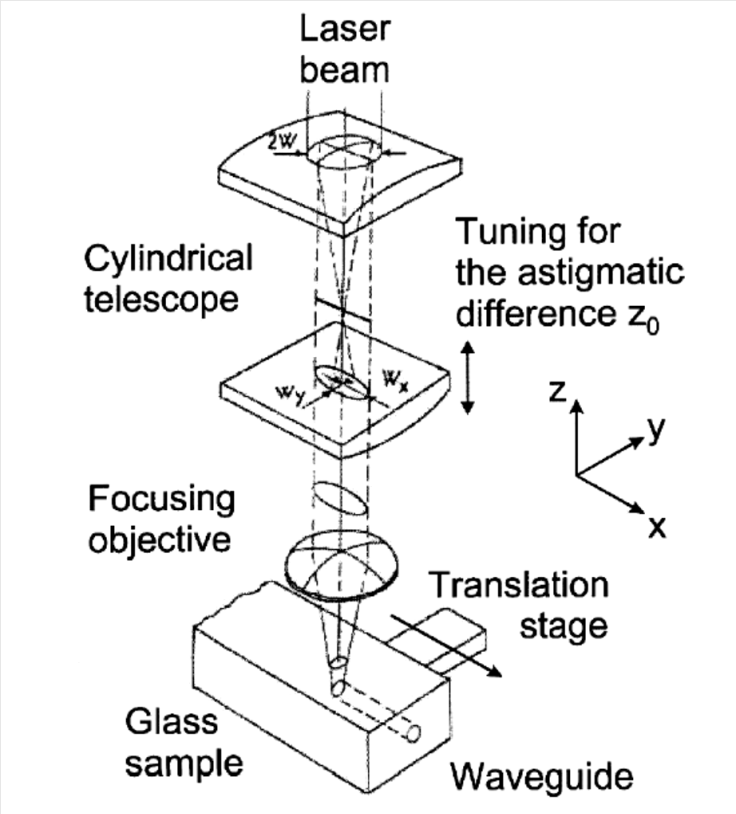

Figure 2.7.Cylindrical telescope apparatus for correction of focal volume asymmetry. Figure taken from Osellame et al.[41].

Deformable mirror

The technique of using a deformable mirror was first applied to control the cross-section of ULI waveguides in 2008 by Thomson *et al.* [42]. The technique has also been developed, incorporating a spatial light modulator, as a method of aberration correction to achieve diffraction limited structures in material substrates [43]. In principle, the technique relies on the manipulation of the beam shape before the focusing objective in order to create a more symmetrical focal volume. This is similar in effect to using the deformable mirror to recreate the function of the slit in 'the slit method' however the deformable mirror offers the advantage that it may be adjusted during inscription to incorporate bends in the waveguide structure. Such manipulation is not possible using 'the slit method'. Figure 2.8 shows a schematic diagram of the apparatus used by Thomson *et al.* for this inscription method.

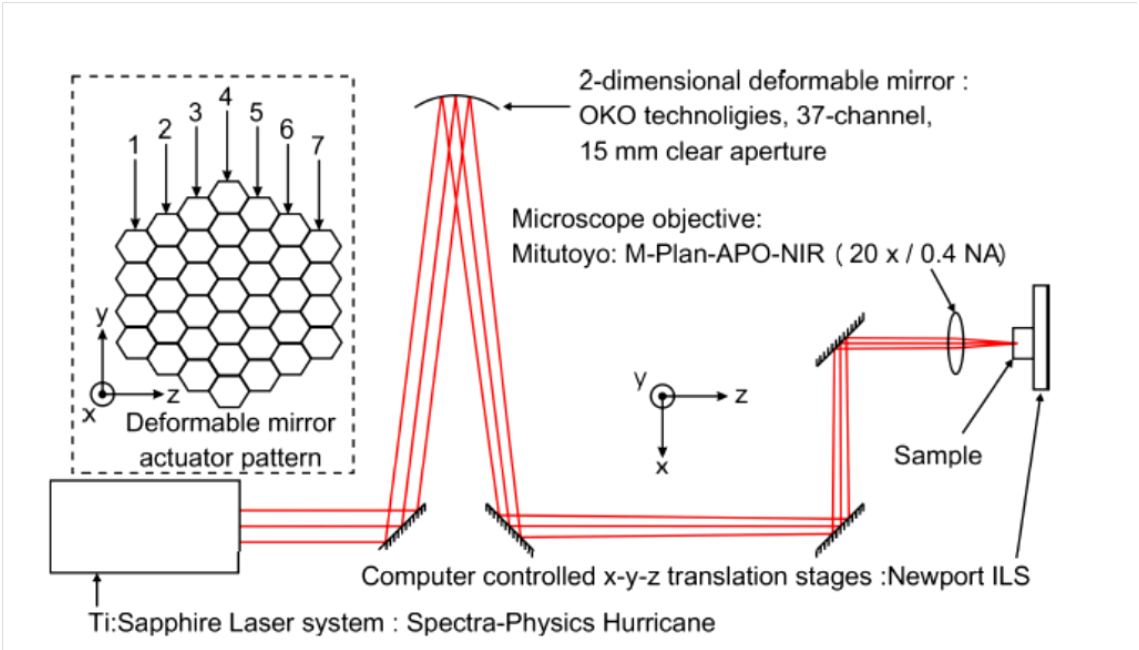

Figure 2.8. Schematic diagram of waveguide inscription utilising a deformable mirror to control the cross-section of the resultant structure. Image taken from Thomson et al. [42].

Multiscan

First demonstrated by Nasu *et al*. [44], the multiscan technique does not involve any manipulation of the inscription beam or focusing geometry. Instead it relies on introducing an additional degree of freedom in the inscription process. All the aforementioned techniques involve a single translation or "scan" of the substrate through the inscription beam. However, as shown in Figure 2.9, the multiscan technique employs a series of these scans, written one after the other, to build up a near homogenous modified region of the desired cross-section. The separation of these individual scans is treated as another fabrication parameter and requires investigation when working with a new material. It can also be seen in Figure 2.9 that the waveguide height is determined by the confocal parameter of the inscription beam and that the waveguide width is then determined by the number and separation of individual scan elements.

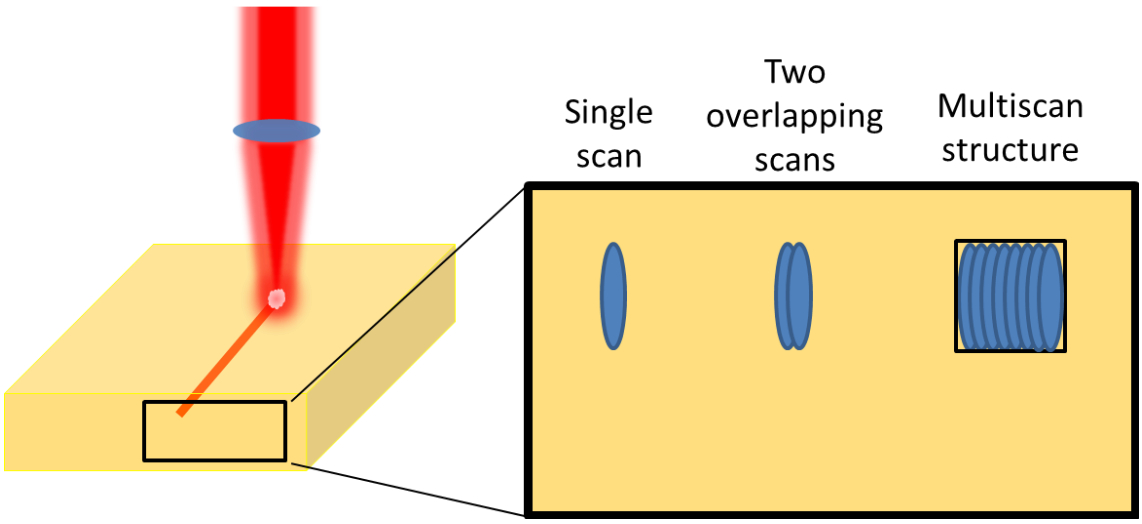

Figure 2.9. Graphical representation of the multiscan technique used to create a near homogenous, symmetrical waveguide cross-section. The blue ellipses represent a modified region inscribed through a single translation of the laser focus through the substrate. The scale of these structures vary depending on the NA of the inscription lens.

2.3.3 Inscription parameters

The inscription process is dependent upon a number of parameters which influence the nature of the resultant inscribed structure. The following table lists the key variables that must be considered throughout the fabrication process.

Inscription beam wavelength	The inscription beam wavelength has a direct correlation with the multiphoton absorption process. Depending on the band-gap of the target substrate, the inscription beam wavelength will determine the order of the multiphoton process, i.e. 2-photon, 3-photon or n-photon absorption. As a result, the wavelength used for inscription influences the respective roles of multiphoton ionisation and tunnelling ionisation.
Pulse energy	The pulse energy used for inscription is obviously one of the key parameters. The amount of energy contained in each pulse from the inscription laser can ultimately determine the amount of energy transferred into the substrate. Control of the inscription pulse energy may allow the desired material modification to be achieved.
Pulse repetition frequency	The pulse repetition frequency mainly affects thermal influences on the inscription process. At low repetition rates there is little or no thermal accumulation and therefore each pulse interacts with cold material. At high repetition rates the opposite is true and thermal accumulation can affect the fabricated structure.
Focusing lens/objective	The focusing lens affects the focal volume and its cross-section. Firstly, this is linked to the cross-section of the modified region in the substrate and secondly it controls the peak irradiance incident on the substrate material.
Inscription beam polarisation	The polarisation of the inscription source affects the efficiency of absorption in the material and therefore the threshold energy for modification. It has also been found to affect the quality, i.e. propagation losses, of waveguides [30], and microfluidic channels with evidence that it influences the formation of nanograting structures [45].

Pulse duration	The effect of pulse duration on inscription is complex and has been shown to drastically alter the nature of the material modification and the resultant losses of waveguides [30, 46, 47]
Thermal accumulation	At high repetition rates the duration between subsequent pulses is short enough that the material does not cool completely before another pulse is absorbed. This leads to an accumulation of heat in the material which can affect the structure cross-section and guiding regions. [48, 49]
Translation velocity	The velocity the sample is translated through the beam affects the extent of overlap between subsequent pulses. This is inherently linked to repetition rate. However, the relationship becomes more complicated at high repetition rates where thermal accumulation adds complexity beyond simply pulse overlap and flux [48-50].
Pulse chirp and pulse front tilt	The spatio-temporal profile of pulses has been shown to have an effect in the inscription process resulting in a non-reciprocity in writing directions parallel and perpendicular to the direction of the pulse front tilt, often referred to as the "quill effect" [51].

Material properties

Material band gap	The band gap of the material has a fundamental effect in relation to the inscription wavelength. These two properties together determine the order of the multi-photon process and hence the relative contributions of multi-photon ionisation and tunnelling ionisation as discussed in Section 2.2.
Crystal geometry	Inscription in a crystal substrate can produce in non-reciprocal results dependent on the direction of inscription with respect to the crystal axes [51]
Material thermal conductivity	The thermal conductivity of the material has a bearing on the occurrence of heat accumulation. It is clear that a material with high thermal conductivity will not experience heat accumulation as readily as one with a low thermal conductivity as the localised increase in heat will be conducted into the surrounding material at a quicker rate.

Nonlinearity	Nonlinear effects can greatly alter the propagation of the laser and the desired nature of the focal volume. For example, self-focusing or defocusing could occur in the substrate outside the desired focal region, causing filamentaion or a complete failure reach a threshold for modification. Frequency conversion could also occur due to processes such as second harmonic generation (SHG) and SPM. This could lead to linear absorption of the higher frequencies or a change in the MPI contribution.

2.4 Type I and Type II waveguides

We have seen that the fabrication of waveguides is possible through translating a substrate through the inscription beam in order to create a modified region of a desired cross-section. However, this is not the only way to fabricate waveguide structures via ULI and often not the most appropriate.

The method of creating a modified region which acts as the core of the waveguide surrounded by an unmodified material 'cladding' is referred to as a Type I structure. It is also possible to inscribe two regions of damage surrounding an unirradiated region which may act as the waveguide core. This is made possible by regions of strain in the material lattice induced by inscribed damage regions or 'tracks', which through the strain-optic effect manifest a change in refractive index. These are referred to as Type II structures and are depicted in Figure 2.10.

-

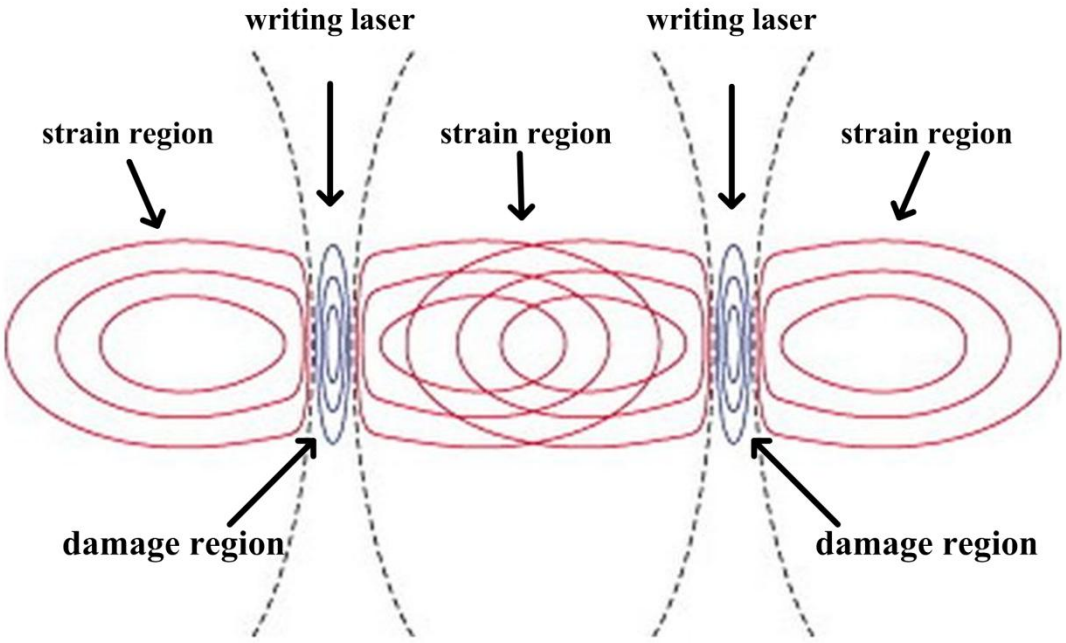

Figure 2.10. Graphical representation of Type II waveguides formed by the strain regions from two damage tracks written in the material substrate. Image taken from Burghoff et al.[52]with added annotations.

This fabrication method is often favoured for active waveguides as the core/guiding region of the structure is left unirradiated and therefore the photoluminescent properties are often unchanged for applications utilising the active properties of the material [53]. However, it has also been demonstrated that Type I waveguides can be fabricated with negligible change to the photoluminescent properties of the core/modified region [54].

2.4.1 Negative refractive index change

The material modification in ULI has so far been detailed as a localised positive change (or increase) in the refractive index of the substrate material however it is also possible to affect a negative change (or reduction). The inscription of such a region is comparable to the formation of Type I modification in that the negative change in refractive index is generally produced in the irradiated material region. This can be

exploited for the inscription of waveguide cladding regions and has been demonstrated in crystalline and glass materials [55, 56].

2.5 Micro-channels and selective etching

In addition to the modification of a material's refractive index, ULI processing has been employed to great effect for the fabrication of microfluidic channels [57, 58]. The process is similar to that of waveguide fabrication with an additional etching process after inscription. With the correct inscription parameters, modified regions of certain material substrates have been shown to exhibit substantially increased etch rates during the chemical wet etch process [45, 59]. There is evidence to suggest that this increase in etch rate is due to the formation of nanograting channels that allow the flow of etchants more readily [45]. This technique showcases the 3-dimensional (3-D) capabilities of ULI allowing the fabrication of arbitrarily shaped sub-surface micro-channels and reservoirs [60].

2.6 Applications of ultrafast laser inscription

The flexibility of ULI has provided a host of applications for the technology through is compatibility with many different materials. The technology has been used to fabricate devices in a wide range substrates including: single crystals such as lithium niobate, yttrium aluminium garnet (YAG), vanadates [61], and double tungstates [62, 63]; ceramic materials [64]; and a many different glasses [29, 65-67]. The benefit of rapid prototyping has led to applications in integrated optics, nonlinear optics, microfluidics and waveguide lasers. Some examples that demonstrate the technology's main strengths of rapid prototyping, flexibility and 3-D capability are given below.

2.6.1 Microfluidic cell sorter

Taking full advantage of the 3-D capabilities of ULI, this device uses microfluidic channels of varying dimensions and reservoirs with inlets and outlets, see Figure 2.11. The device was created in a silica chip using ULI to increase the etch rate of the material, as described in Section 2.5. The irradiated volume was then removed through

wet-etching, leaving the desired microchannels and reservoirs of the device. This device was demonstrated as a non-invasive cell separator for different mammalian cells and published in 2012 [60].

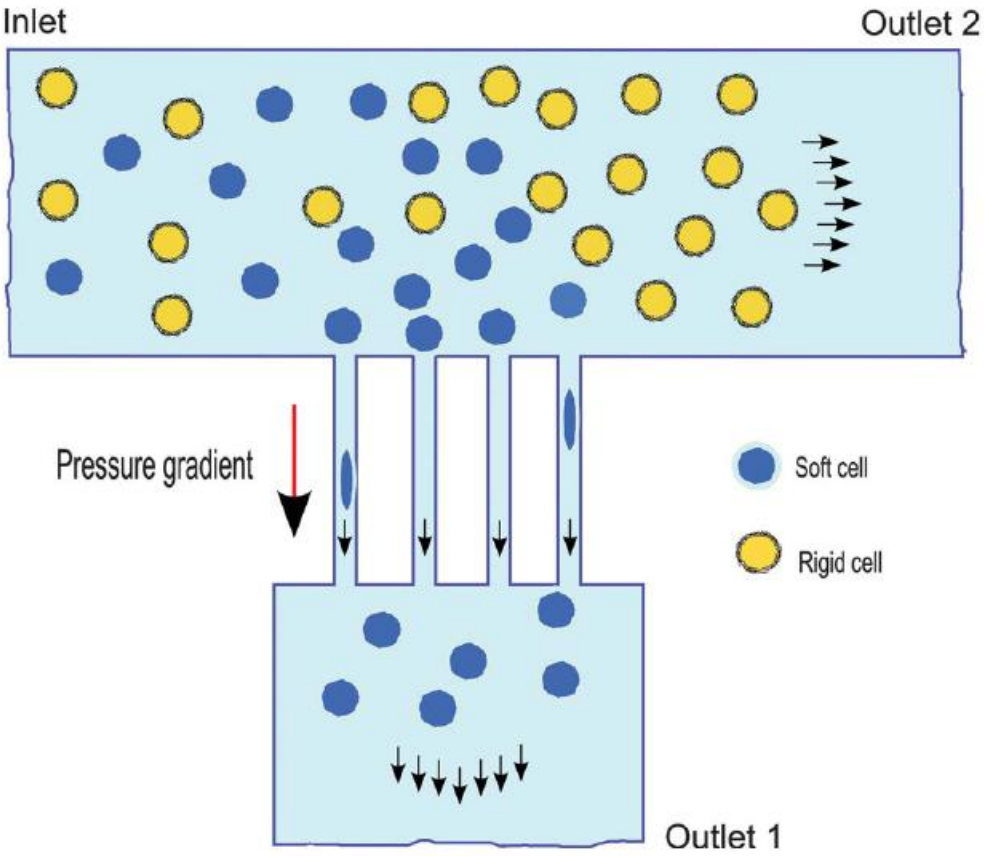

Figure 2.11. Schematic of a 3-D microfluidic cell separator with ULI aided, selectively etched channels and reservoirs. Image taken from Choudhury et al. [60].

2.6.2 Photonic lantern

Another demonstration of the truly 3-D capabilities of ULI is the photonic lantern device fabricated by Thomson *et al.*[68]. Figure 2.12 and 2.16 show the 3-D structure transitioning from multi-mode to single-mode and vice versa as well as the mode intensity distributions observed while adjusting the coupling of 1539 nm light into each end respectively.

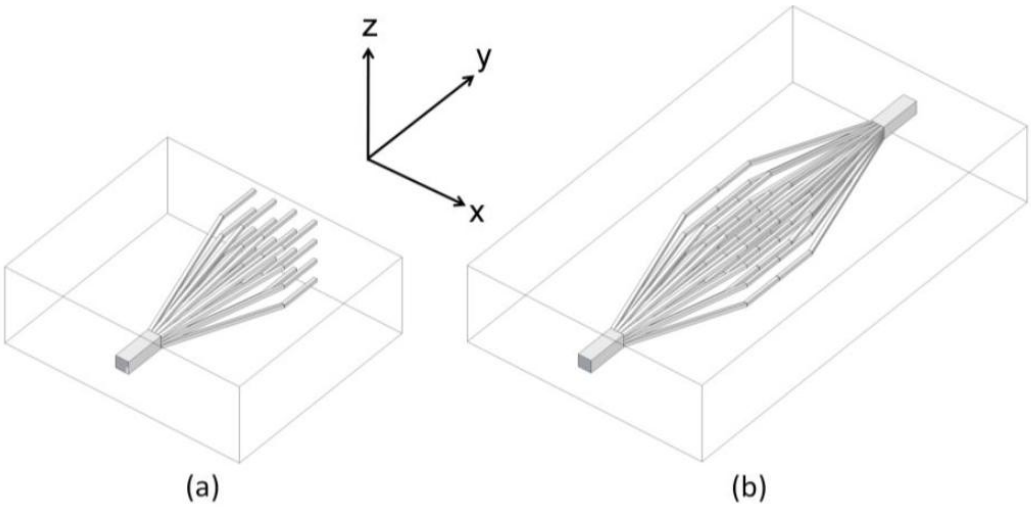

Figure 2.12. Schematic diagram of (a) ULI inscribed multi-mode to single-mode array photonic lantern and (b) two adjoined photonic lanterns providing multi-mode to single-mode array to multi-mode geometry. Image taken from Thomson et al. [68].

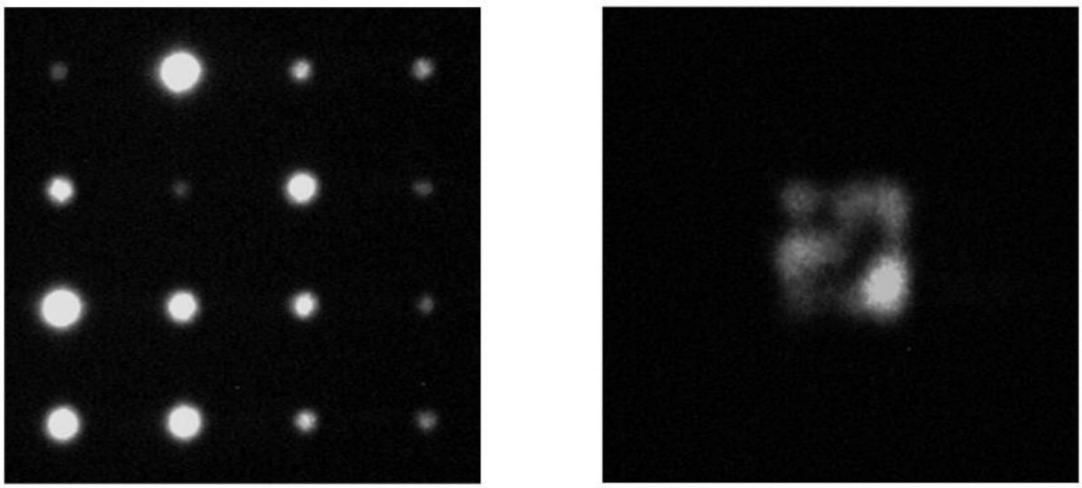

Figure 2.13. Image of photonic lantern outputs with single-mode array (left) and multi-mode spatial field distribution (right).Images taken from Thomson et al. [68].

2.7 Summary

This chapter has presented the main concepts behind ultrafast laser inscription and provided an introduction to the key techniques and experimental parameters. The flexibility of the technology has been demonstrated with devices ranging from simple waveguide structures to complex 3-D photonic devices and microfluidic lab-on-chip solutions. I believe that it is this inherent flexibility and rapid prototyping capability that are the main strengths of the technology.

Chapter 3 - Refractive index modification of ZnSe using ultrafast laser inscription

ULI has now successfully been used to inscribe waveguides in a large range of different materials spanning glasses, ceramics and single crystal materials [54, 69-72]. An interesting application of this has been the rapid prototyping and development of channel waveguide technology in nonlinear glasses and crystals for the exploitation of their nonlinear properties and phenomena such as frequency conversion, Raman gain and spectral broadening. To this end, low-loss waveguides have been demonstrated in crystals such as barium borate (BBO), periodically poled lithium niobate (PPLN), Bismuth Borate (BIBO), periodically poled potassium titanyl phosphate (PPKTP), and potassium gadolinium tungstate (KGW) [63, 73-76]. Another exciting prospect is the application of ULI technology to semiconductors and compound semiconductors. Channel waveguide technology has been demonstrated for the unitary semiconductors Si and Ge [77, 78]. These consisted of silica capillaries filled with the crystalline Si or Ge using high-pressure chemical vapour deposition (HPCVD). Furthermore, Nejadmalayeri *et al.* [79], have demonstrated ULI waveguide structures in silicon. However, compound semiconductors such as ZnSe often possess superior optical transmission, with ZnSe providing high transmission from 500 nm to 22 µm as shown in Figure 3.1. Compound semiconductors can also exhibit high optical χ^2 nonlinearities [80], which unitary and amorphous semiconductors lack due to their centrosymmetric structure. A further advantage is their ability to host transition metal dopants. Indeed, II-VI semiconductors have been demonstrated as mid-infrared laser sources with Cr^{2+} and Fe^{2+} ions providing gain media for 2 – 3 µm and 3.5 – 5.0 µm respectively [8, 11]. These properties are all motivating factors towards the development of compound semiconductor integrated photonic structures and ULI, with its proven flexibility, is well placed as a technology to investigate a solution to the problem of channel waveguide geometry in these materials.

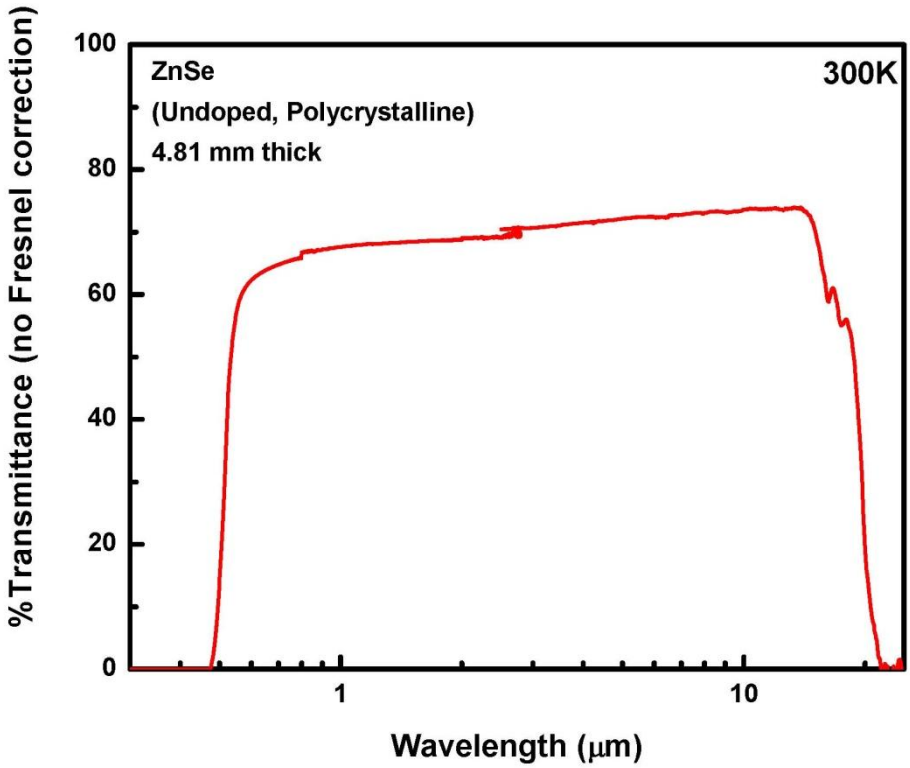

Figure 3.1. Optical transmission of undoped, polycrystalline ZnSe. The sample length was 4.8 mm and the transmission has not been corrected for Fresnel. With Fresnel reflections removed the transmission would be near 100% across the transmission window. Image taken from [81].

A major challenge associated with ULI in highly nonlinear materials is that the high peak powers utilised during ULI can induce unwanted nonlinear phenomena,[30] such as self-focusing, frequency conversion and filamentation, which greatly distort the pulse propagation, [30, 33]. A good example of this are the previous attempts of ULI in ZnSe which have failed to reach a required threshold for modification [82] despite using high pulse energies of >30 μJ. When we consider that the pulse duration and high NA lens (NA = 0.55) used in this case was 120 fs the peak intensity generated would be over 1×10^{15} $W \cdot cm^{-2}$. This suggests that these detrimental nonlinear effects are responsible for halting the desired index modification processes rather than lack of peak power. As self-focusing and filamentation depend on the third order nonlinearities of the material, it is important to consider the dispersion in the nonlinear refractive index, n_2, Figure 3.2, of ZnSe before attempting ULI with a particular laser source. It can be seen that the n_2 value of ZnSe at 800 nm is approximately 100 times greater than fused silica and 10 times greater than the optical crystal $LiNbO_3$[83], which has shown successful

fabrication of waveguides using ULI [31]. It can also be seen that the n_2 value of ZnSe is near a local maximum at 800 nm and in fact a fabrication beam with a longer wavelength, e.g. > 1000 nm, would be more appropriate.

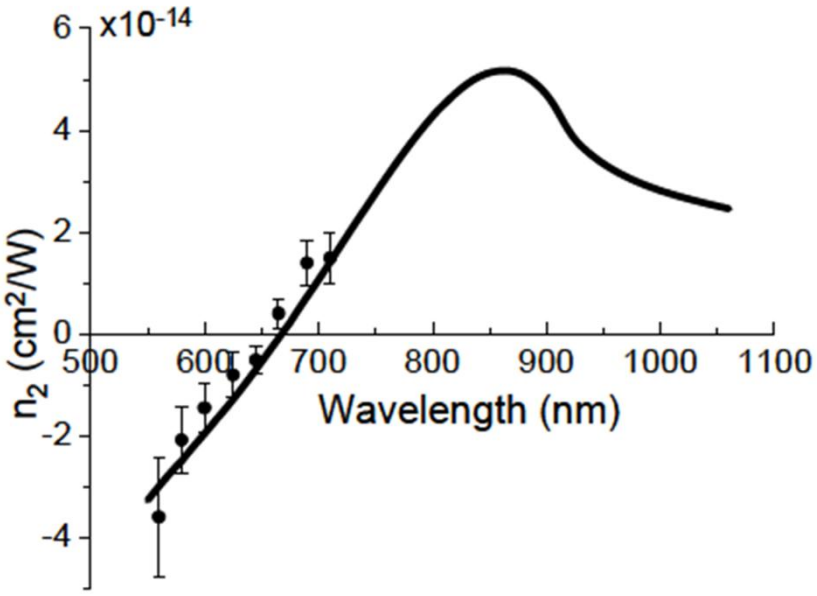

Figure 3.2. Dispersion of n_2 of ZnSe with wavelength. The graph points represent measured data and the black curve represents calculated theoretical values. Figure taken from Sheik-Bahae et al.[6].

3.1 Inscription lasers and apparatus

The Nonlinear Optics Group at Heriot-Watt University has two purpose built ultrafast laser inscription systems. A description of both systems is given in this section.

3.1.1 Fianium® inscription laser

Initial laser inscription work discussed in the following chapter was carried out using a custom model Fianium® fibre master oscillator power amplifier (MOPA) system. The laser architecture comprised of a fibre oscillator and pre-amplifier followed by a pulse picker. The pulse picker allows variation of the pulse repetition rate between 200 to 700 kHz before a final amplifier stage providing average powers of over 500 mW

throughout the range of repetition rates. A fixed compressor on the laser output allowed reduction in the pulse chirp generating pulse durations of 300 – 450 fs depending upon the selected repetition rate.

3.1.2 IMRA® inscription laser

The inscription laser used for the majority of this project was an IMRA® µJewel D400 fibre MOPA system. The laser architecture is similar to that of the Fianium® system described above with a key difference in that the pulse compressor on the output is adjustable. The repetition rate of the laser is adjustable from 100 kHz up to 5 MHz with an average output power of over 250 mW for repetition rates lower than 500 kHz and 350 mW for repetition rates upwards of 500 kHz. The adjustable pulse compressor allows control of the linear chirp on the laser output. This can be used to optimise the output for the shortest manageable pulse duration by reducing the linear chirp of the pulse. On the other hand it can also be used to achieve a longer pulse duration by limiting the recompression of the pulse after the final amplifier stage. Using this adjustable compressor it is possible to achieve pulse duration in the range of 400 fs to 3 picoseconds. Figure 3.3 - Figure 3.5 show the apparatus used for the IMRA inscription laser with the key components labelled.

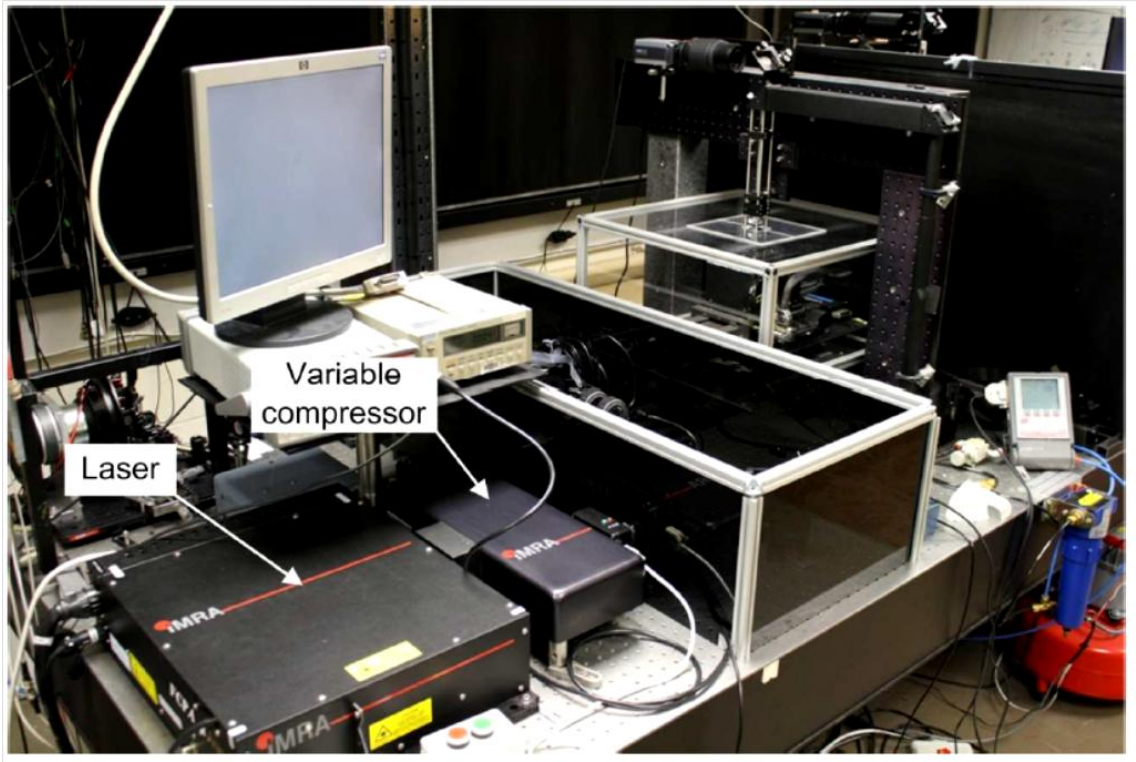

Figure 3.3. IMRA fabrication laser with external variable pulse compressor.

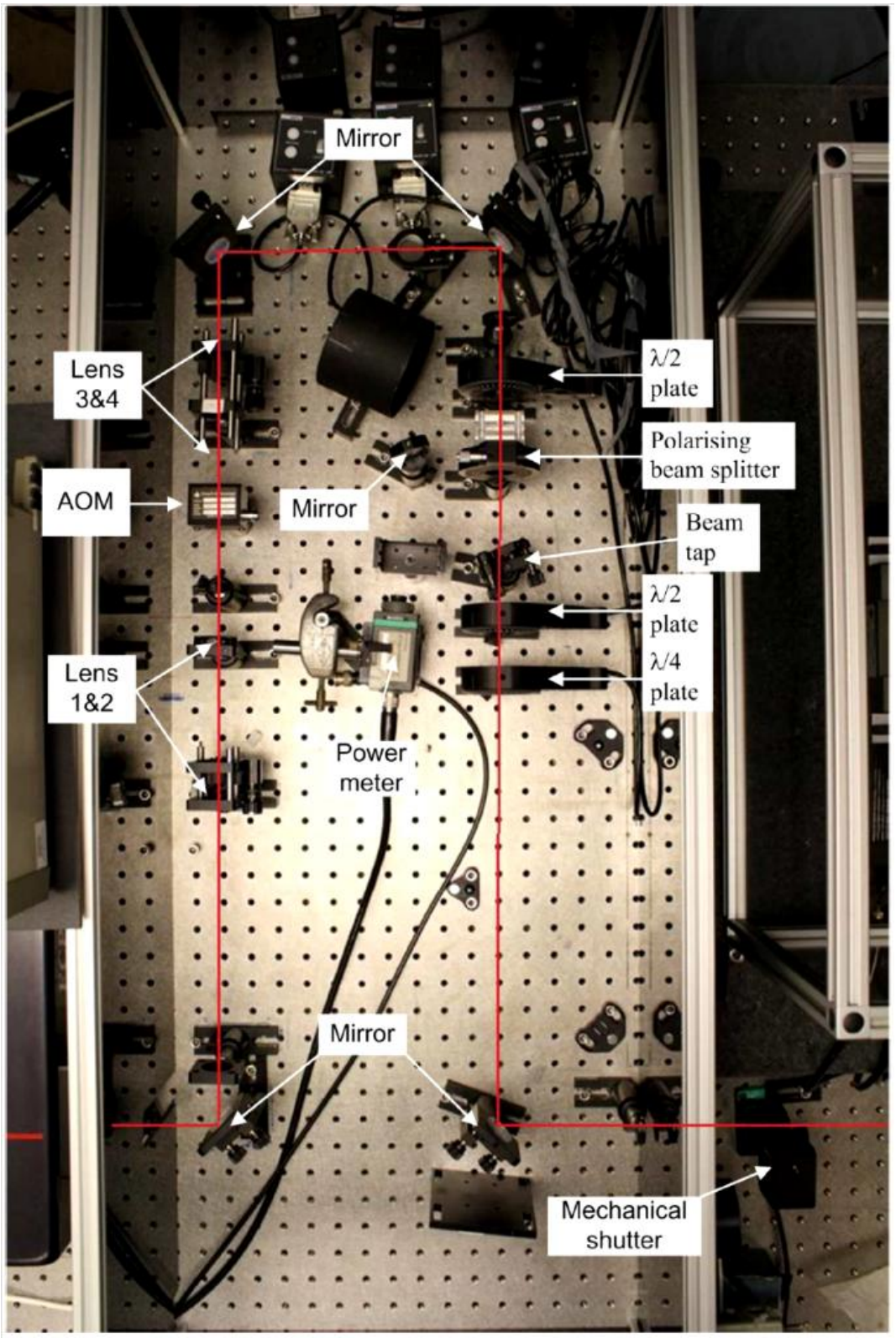

Figure 3.4. IMRA laser beam path displaying power and polarisation control components and AOM for inscription beam modulation.

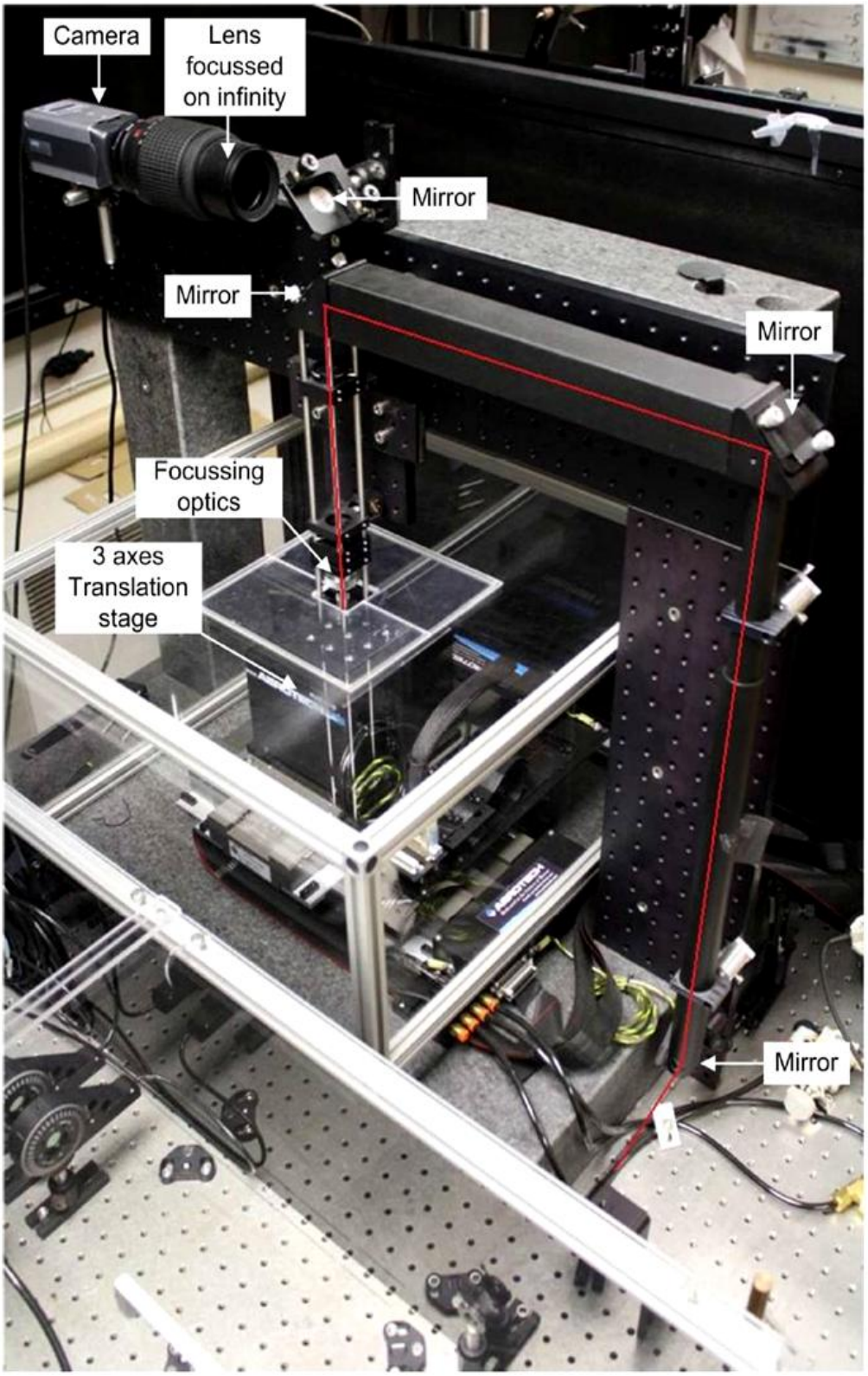

Figure 3.5. Inscription beam path and Aerotech translation stage geometry displaying steering mirrors, imaging system and inscription lens.

3.2 Femtosecond laser inscription

In order to fabricate waveguides in ZnSe using ULI a parameter range must be determined to successfully modify the refractive index of ZnSe. The initial fabrication attempts were carried out using the Fianium fibre laser set up described above in Section 3.1.1. The samples used were all polycrystalline ZnSe measuring 10 x 30 x 3 mm and polished on all faces. The fabrication beam provided 720 nJ, 350 fs pulses at 500 kHz with circular polarisation and was focused with a 0.6 NA lens, 100 µm below the surface of the material. Multiscan structures were written using 20 overlapping scans separated by 400 nm. A range of sample translation velocities from 0.25 – 6 $mm{\cdot}s^{-1}$ were investigated and the resulting structures were observed under an optical microscope in transmission mode with white light illumination. Figure 3.6 shows the optical micrograph of the structures' end facets. It can be seen that only the lower velocities of $1.5mm{\cdot}s^{-1}$, $1mm{\cdot}s^{-1}$, $0.5mm{\cdot}s^{-1}$ and $0.25mm{\cdot}s^{-1}$ produced observable changes in the material and that all the structures present highly asymmetric regions of modification.

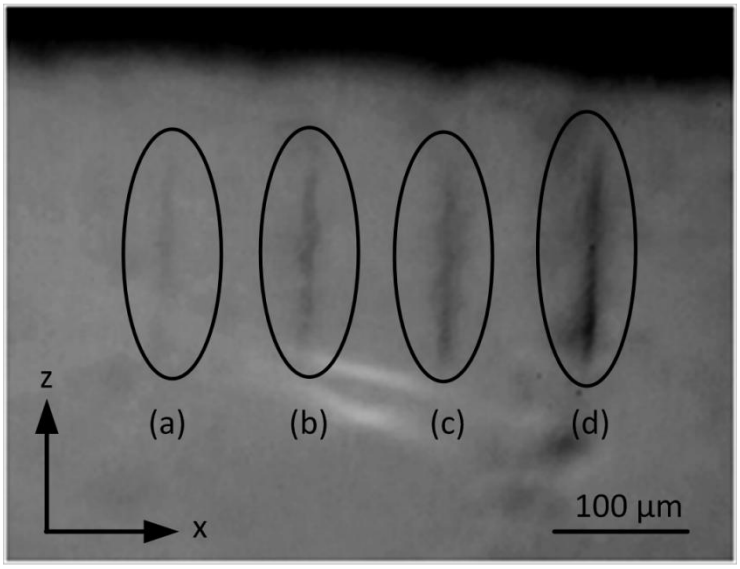

Figure 3.6. Transmission microscope optical micrograph of ZnSe sample end facet showing an array of elongated structures inscribed using translation velocities of (a) 1.5 $mm{\cdot}s^{-1}$ (b) 1.0 $mm{\cdot}s^{-1}$ (c) 0.5 $mm{\cdot}s^{-1}$ (d) 0.25 $mm{\cdot}s^{-1}$.The inscription beam was incident from above the structures in the z-axis. Contrast in the observed structures increases with decreasing translation speed suggesting a greater change in the material.

The same multiscan technique was used to write at 0.1 $mm{\cdot}s^{-1}$ in an attempt to obtain a greater degree of modification of the material. The structure written at a translation speed of 0.1$mm{\cdot}s^{-1}$, shown in Figure 3.7, displayed stronger modification than previous structures, shown in Figure 3.6, but when light was coupled to the structure end facet with a fibre and no guiding was observed as a result of any structure.

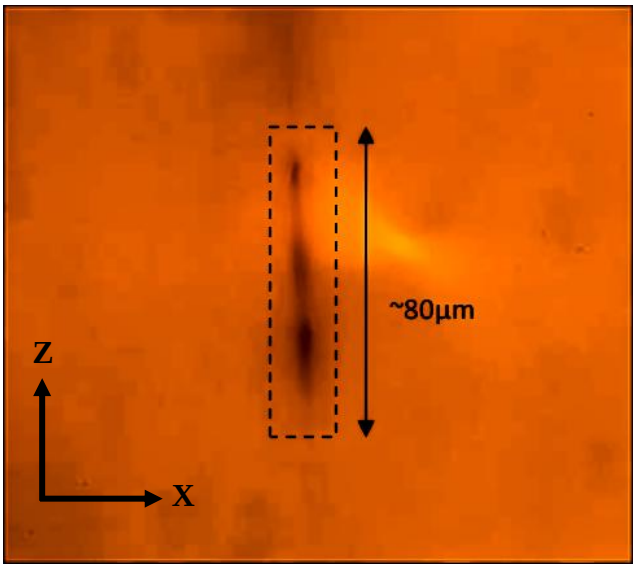

Figure 3.7. Transmission microscope optical micrograph of the ZnSe sample end facet displaying modification of ZnSe with multiscan technique at a writing speed of 0.1 $mm.s^{-1}$. The inscription beam was incident from above the image in the Z-axis.

The cross-section of the observed structure shown above in Figure 3.7 demonstrates that some modification is occurring over a length much greater than the intended focal volume (inscription confocal parameter). The expected inscription confocal parameter of the system is approximately 9 microns whereas this filament-like structure propagates in the z-axis, i.e. the inscription beam axis, for approximately 80 microns inside the ZnSe substrate and exhibits multiple localised points with increased modification. The width of the structure varies between 2 – 3 microns which is narrower than the expected 9 micron wide multiscan structure suggesting a collapse of the inscription beam. This is similar to the filamentation process in transparent media described by Couairon *et al.* [34], which is highlighted in Figure 3.8 alongside the filament-like structure in ZnSe. This observation suggests that the high nonlinear

refractive index, n_2, value of ZnSe is still causing the unwanted nonlinear, self-focusing effects to dominate.

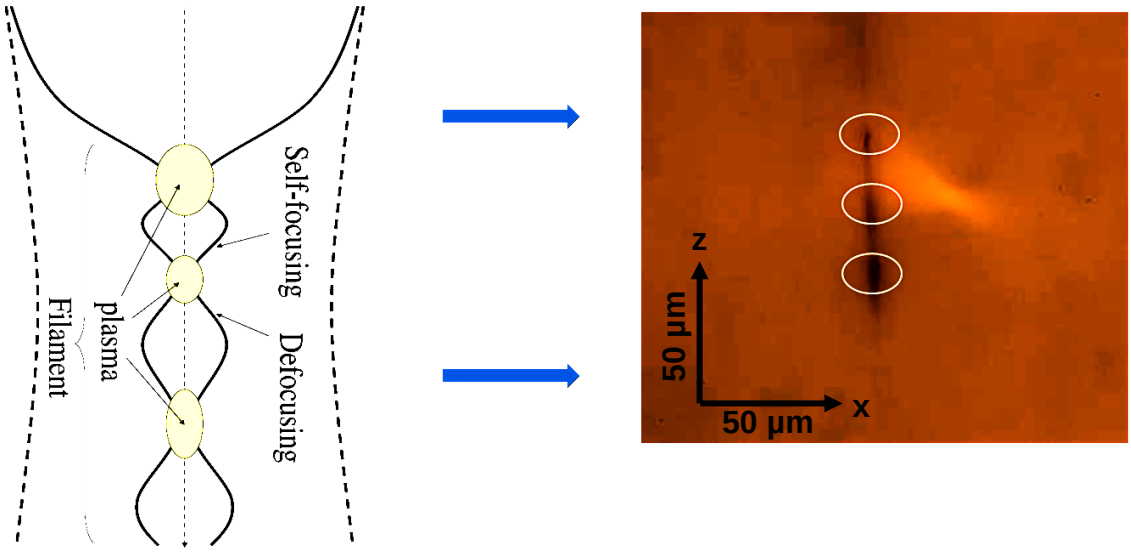

Figure 3.8. (a) graphical representation of refocusing cycle caused by self-focusing and plasma defocusing. Image taken from Couairon et al [34]. (b) Inscribed structure showing elongation in the inscription beam axis damage comparable to the refocusing cycle displayed in (a).

As the process of self-focusing is dependent on the peak power of the incident radiation, inscription with longer pulse durations was proposed as a method for overcoming these detrimental nonlinear effects. Longer pulse durations and their effect on the inscription process could be investigated using the IMRA inscription laser system described in Section 3.1.2 which provides pulse durations from 400 femtoseconds to 3 picoseconds.

3.3 Picosecond laser inscription of type I waveguides

The investigation of pulse duration has previously been applied, although not extensively, in an effort to improve the quality of waveguides fabricated in other nonlinear crystals such as $LiNbO_3$. Nejadmalayeri *et al.*[30], suggested that the use of longer pulses reduced nonlinear pulse break up and hence enabled sufficient energy to be deposited for the required modification. Through the use of longer pulse durations the pulse energy may remain unchanged while reducing the peak power incident upon the target substrate, in order to avoid filamentation. The aforementioned multiscan technique can also be useful in overcoming nonlinear effects as it allows a modified area to be built up while using lower pulse energies to irradiate smaller focal volumes..

3.3.1 Structure inscription and characterisation

As part of the characterisation of these structures it is important to know what optical loss is incurred through the use of a waveguide. The total loss incurred is referred to as the insertion loss and is defined as below:

$$L_I = L_P + L_C \qquad \textit{Equation 3.1}$$

where L_I is the total insertion loss, L_P is the loss incurred as light propagates through the waveguide and L_C is the coupling loss of the system which comprises of the Fresnel reflections and any mode mismatch, [84], between the incident mode and the waveguide mode.

Using the IMRA fabrication laser setup, a wider range of parameters could be investigated by including pulse duration as a key parameter. The fabrication beam was provided by the commercial Yb-doped master oscillator power amplifier (MOPA) laser system (IMRA µJewel D400), as detailed in Section 3.1.2. Importantly, this laser system utilised an external pulse compressor which allowed control of the pulse duration between 350 fs – 2.5 ps. For the work outlined here, pulse repetition rates from 500 kHz to 3 MHz were investigated, the pulse duration was varied between 500 fs to

2.0 ps and a range of pulse energies from 70 – 200 nJ were investigated. The polarisation of the laser beam was adjusted to circular as shown to provide lower loss structures in other crystalline materials [30]. To reduce the risk of surface ablation from the large pulse energies being investigated, the beam was focused 100 µm below the surface of the sample using an aspheric lens with an NA of 0.67. The sample was then translated perpendicular to the laser beam propagation direction using translation speeds ranging from 0.25 $mm.s^{-1}$ to 4 $mm.s^{-1}$ on high precision air bearing stages (Aerotech, shown in Section 3.1). A multiscan structure was inscribed constructed from 20 overlapping modified regions separated by 400 nm, the same design used for the femtosecond inscription study.

Structures inscribed using pulse durations < 1.0 ps exhibited material modification, but were found to result in filamentation as for the results obtained with the femtosecond inscription in Section 3.2. In contrast, when the pulse duration was increased to > 1.0 ps, it was observed that the filament like structures could be avoided and this was observed over a wide range of inscription parameters upon increasing the pulse duration to above 1.5 ps. An example of the structures formed by > 1 ps pulses is shown in Figure 3.9. In order to measure the insertion loss of these waveguides, an 800 nm signal from a CW Ti:sapphire laser was coupled into one end of the waveguide with a 0.07 NA objective. This objective was chosen for the insertion loss measurement so the incident focal spot diameter of the signal was comparable to that of the waveguide mode at 800 nm, therefore reducing the coupling loss. The emergent light at the opposite end of the waveguide was gathered using a 0.25 NA objective and imaged onto a camera. An aperture was used to block any excess scattered light outside the waveguide and the isolated waveguide mode was then imaged onto a power meter. The output power measured was then compared to a reference signal. This reference signal was taken from the same system aligned without the waveguide and aperture. Figure 3.10 shows the apparatus arrangement for the insertion loss characterisation of waveguides at 800 nm.

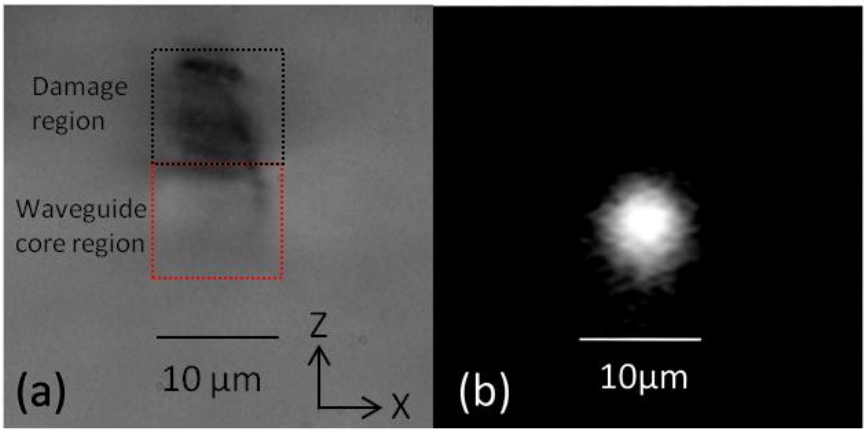

Figure 3.9. (a) Optical micrograph of waveguide end facet inscribed using 1.5 ps pulses. The image was taken using an optical microscope in transmission mode. Guiding region highlighted by red square with a dark damage region located above the waveguide core. (b) 800 nm single mode supported by adjacent waveguide. The field view of both images (a) and (b) is 35 µm × 35 µm and the inscription laser was incident from above the image in the z-axis.

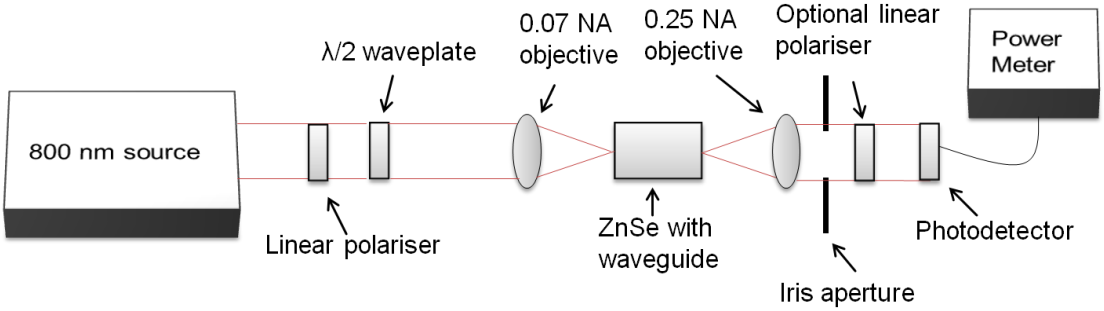

Figure 3.10. Characterisation apparatus and arrangement for waveguide insertion loss measurements.

It can be seen that the filamentation has been overcome through use of longer pulses as the structure in Figure 3.9 is more symmetric in cross-section and of similar dimensions to that of the desired 9 × 9 µm multiscan structure. The waveguide core highlighted in Figure 3.6 with a red box is approximately 9 µm in width but the cross-section of the core is not clear due to the poor definition of the structure in the z-axis. The darkened region above the core is material damage. This damage formation has been observed in the fabrication of type I waveguides in other crystalline materials however the origin of this is not evident [31]. The structure fabricated using 1.5 ps pulses shows a uniform

symmetrical structure and the associated mode field for 800 nm guiding is also shown in Figure 3.9 to be symmetrical and 10 µm in diameter. This structure was written at a translation velocity of 1 $mm.s^{-1}$ with 85 nJ pulses at a repetition rate of 3 MHz and exhibited a free space total insertion loss of 3.1 dB for a 29 mm waveguide, which was the lowest for all the waveguides at 800 nm. This is comparable to other low insertion loss ULI waveguides written in crystals, [62, 85].

Waveguiding of 1550 nm radiation was also investigated as a necessary step towards applications at the longer wavelengths ZnSe is transparent over. One example of such an application would be waveguides in Cr^{2+}: ZnSe as the pump source would be required to be between 1500 nm and 2000 nm [86]. The requirements for single mode guiding at 1550 nm are substantially different from that of 800 nm and waveguides fabricated with higher pulse energies were inscribed with a view to achieving a higher index contrast at the modified region. Structures fabricated with pulse energies greater than 100 nJ were found to guide at 1550 nm. Optimisation of the fabrication process was performed by a more in depth investigation of a range of pulse energies, 60-200 nJ, with writing speeds of 0.5, 1, 1.5 mms^{-1}. A limited investigation of pulse widths from 1.5 – 2.5 ps was carried out in this case as it had been established from our previous work that pulses widths > 1.5 ps achieved the desired material modification. As before, circular polarisation and a 0.67 NA objective were used with the IMRA fabrication arrangement.

Insertion losses were measured using a 1550 nm source in a free space setup similar to the 800 nm characterisation, see Figure 3.10. The lowest loss waveguide at 1550 nm demonstrated a total insertion loss of 5.0 dB for a 29 mm waveguide. The higher insertion loss is expected to be due to increased scattering losses which arises from the overlap of the guided mode with damage regions in the structure. Figure 3.11 shows the waveguide facet image taken with a microscope in a transmission mode using white light illumination and the waveguide's associated mode field at 1550 nm.

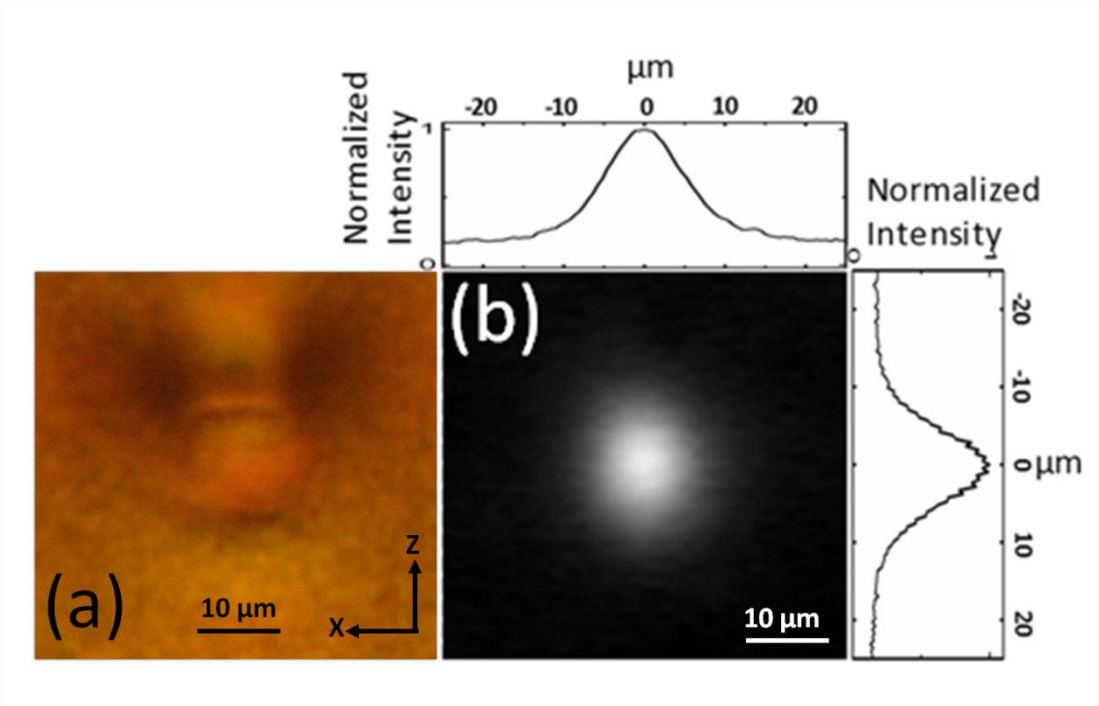

Figure 3.11. (a) Optical micrograph taken using a microscope in transmission mode with white light illumination showing 1550 nm waveguide facet with (b) associated mode field, near field CCD camera image. The inscription beam was incident from above the image, propagating in the z-axis. The field view of both (a) and (b) is 50 µm x 50 µm.

It can be seen when comparing the area of the 1550 nm mode compared to that of the structure guiding region that the mode will overlap with a portion of the material damage, observed as the darkened regions in Figure 3.11 (a). This could lead to increased scattering losses and is suspected to be the reason for the higher insertion loss at 1550 nm compared to 800 nm.

3.4 Fabry-Pérot Characterisation

The insertion loss measurements carried out on the waveguides provide a loss value incorporating the coupling loss and the waveguide propagation loss. As the coupling loss can be reduced by appropriate selection of input lens and AR coating of the crystal facets it is important to determine the propagation losses of the waveguide. The Fabry-Pérot fringe technique allows the propagation losses of a waveguide to be measured by treating the waveguide as a Fabry-Pérot etalon where the Fresnel reflections of the waveguide end facets act as the etalon mirrors. Tuning the wavelength of the light entering the etalon produces a fringe set from which the internal loss of the etalon (the waveguide) can be inferred [31].

Light from a tuneable, 1498-1581 nm Er: fibre laser source (Anritsu MG9638A) was coupled into the waveguide and collected at the opposite end using a pair of 10x magnification, 0.25 NA objectives. The output was then coupled into a near-infrared spectrum analyser (Advantest Q8384) which could be used to record the output signal power and wavelength. The tuneable light source was then scanned across 0.2 nm in steps of 3 pm in order to construct the Fabry-Pérot fringe pattern. The line-width of the tuneable laser source was 700 kHz (5.6 fm) so the fringes could be easily resolved. The contrast between the fringe maxima and minima could then be used to determine the propagation losses of the waveguide. Figure 3.12 shows an example of a Fabry-Pérot fringe set.

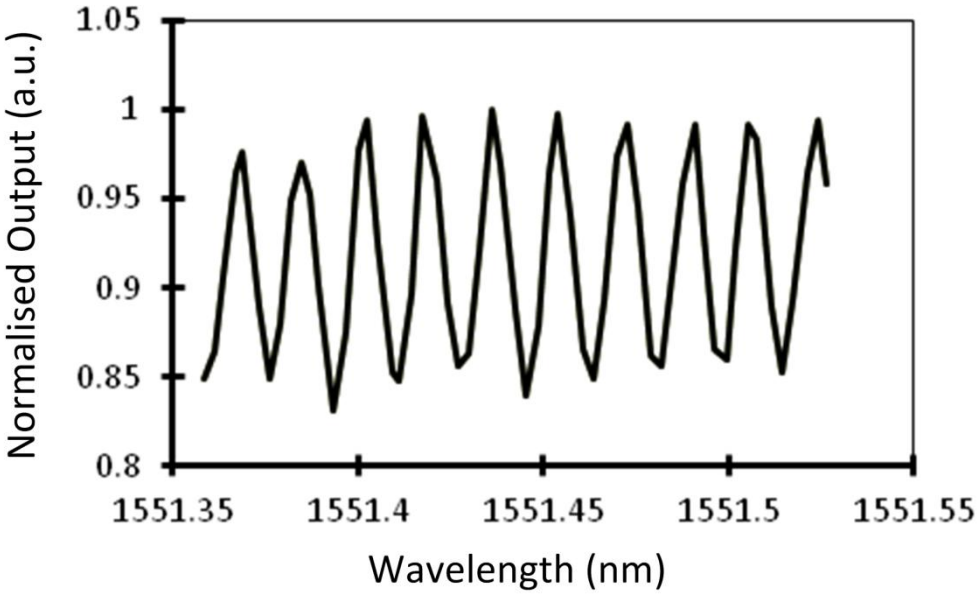

Figure 3.12. Example of Fabry-Pérot fringe set used for propagation loss calculations. The data displayed is a normalised plot of the wavelength against waveguide power output.

The contrast of these fringes is defined by Equation 3.2. This value can then be used to determine the value of the propagation losses as in [87].

$$K = \frac{I_{\max} - I_{\min}}{I_{\max} + I_{\min}} \qquad \textit{Equation 3.2}$$

where I_{max} and I_{min} are the maximum and minimum transmitted output respectively and K is defined as the fringe contrast. Equation 3.3 shows how this is calculated using an adaptation of the formula for the transmitted intensity in a symmetric Fabry-Pérot resonator.

$$R\exp(-\alpha L) = \frac{1}{K}(1 - \sqrt{(1-K^2)}) \qquad \textit{Equation 3.3}$$

where α represents the propagation loss per unit length, L, and R is the effective mirror reflectivity which is determined from the Fresnel reflections. It is for this reason that the waveguide facets must be very well polished. Poorly polished facets would result in lower reflectivity and, therefore, error in the loss measurement.

Repeated Fabry-Pérot fringe measurements were taken over a range of wavelengths (1498-1581 nm) and an average propagation loss of 1.1 with standard deviation ± 0.1 dB.cm^{-1} was determined. This is comparable to ULI inscribed waveguides in other crystalline materials, such as lithium niobate and double tungstates [31, 62], and marks an important milestone in the development of directly written optical devices in ZnSe. The insertion losses measured were a minimum of 5.0 dB for a 29 mm waveguide. As the insertion loss is composed of the propagation loss, coupling loss and Fresnel loss, we can attribute 1.7 dB to the Fresnel losses and 0.2 ± 0.2 dB to the coupling loss. This value for the coupling loss is in good agreement with the theoretical 2-D Gaussian field mismatch value, 0.19 dB, calculated as described by Marcuse [84].

3.5 Conclusions

This chapter has shown successful refractive index modification of polycrystalline ZnSe using ULI. The detrimental nonlinear effect of self-focusing in the crystalline medium was found to be overcome through utilising picoseconds pulses instead of femtosecond pulses allowing an investigation into waveguide inscription in ZnSe using ULI. A broad range of inscription parameters were investigated, spanning: pulse energy; pulse duration; pulse repetition rate; and sample translation velocity. This ultimately yielded the successful fabrication of optical waveguides which demonstrated guiding of 800 nm and 1550 nm radiation with the latter exhibiting propagation losses as low as 1.1 (±0.1) dB·cm^{-1}. This value is comparable with that of other laser inscribed waveguides in crystalline materials although there is potential for achieving lower propagation losses through further optimisation of inscription parameters. The low losses obtained for these structures would permit their use for nonlinear and integrated optical systems and allow the nonlinear properties of ZnSe to be exploited in a compact, guided-wave geometry. Furthermore, the development of successful ULI parameters in ZnSe allows the progression of work into mid-infrared devices in ZnSe with a view to potential applications in transmission metal doped ZnSe.

Chapter 4 –Mid-infrared waveguides in ZnSe and Cr^{2+}: ZnSe

The waveguides detailed in Chapter 3 proved to be viable for near-infrared applications with low propagation losses and near symmetric mode profiles at 800 nm and 1550 nm. Importantly, ZnSe is also well suited to applications in mid-infrared photonics with high optical transparency stretching from 500 nm – 22 µm, see Figure 3.1. Most commonly this is exploited for the fabrication of mid-infrared optical components including lenses and windows. However, the material has also received a lot of attention in other areas of photonics including semiconductor lasers and nonlinear optics.

The fabrication of II-VI semiconductor blue-green laser diodes utilises ZnSe in combination with the growth of other II-VI materials to engineer structures with tailored band-gaps [88]. The layering of different materials forms an interface known as a heterojunction, or heterostructure for more than one interface, which is fabricated with the view to creating a desired band-gap energy[89]. Some examples include the combination of ZnSe with other materials with ZnMgSSe [90] or ZnCdSe [91], to form quantum wells or dots for the fabrication of blue and green laser diodes. The motivation to develop such semiconductor lasers in the visible spectral region was driven by many mass market technologies and products such as visual display technology and optical recording and printing [92, 93]. A significant challenge to this technology however has been the power limitations and operation lifetime of devices due to degradation of the heterojunctions [94].Ultimately the development of inexpensive blue laser diodes using GaN [95] led to their domination of the market over II-VI semiconductor diodes.

As previously discussed, ZnSe is also a highly nonlinear material with the potential for applications in nonlinear optical systems. The development of the Z-scan technique for measuring material nonlinearities [96, 97] allowed many of the nonlinear material properties to be measured. Investigation and analysis of properties such as two-photon absorption coefficients [98, 99], third order nonlinear susceptibility, $\chi^{(3)}$ [99, 100], and nonlinear refraction [99, 101, 102] has allowed catalogue of data to be compiled for ZnSe. Consequently, the material is now often used as a standard for many nonlinear optical measurements such as the Z-scan technique. This work has resulted in Z-scan

becoming a universal experimental method for the characterisation of nonlinear material properties producing one of the highest cited papers, over 1000 citations, in the history of the IEEE [97].

The $\chi^{(2)}$ nonlinearity of ZnSe has been measured at 1047 nm to be 43 pm·V^{-1} [80], which is significantly larger than that of the ubiquitous nonlinear crystal lithium niobate, 27 pm·V^{-1} [103]. This property of ZnSe has been utilised to demonstrate frequency conversion using orientation patterned ZnSe [104]. Further applications that utilise the material nonlinearities include spectral broadening [105], arising from the $\chi^{(3)}$ nonlinearities, and passive devices for limiting the maximum fluence and irradiation of a laser beam, known as optical limiters [106].

The ability to confine light in a small cross-sectional area over distance makes waveguide geometry well suited to nonlinear applications. High irradiances can be maintained over much greater lengths than that which can be achieved at a beam focus, allowing the nonlinear properties of the waveguide core material to be exploited. Waveguide fabrication in semiconductors is most commonly performed in planar geometry but several new channel waveguide technologies are emerging in important materials for the mid-infrared. Fibre drawing of chalcogenide glasses and unitary semiconductors deposited in capillaries have both provided access to mid-infrared waveguides meters long [77, 78, 107, 108]. More recently, ZnSe was also successfully demonstrated as a compound semiconductor waveguide in fibre geometry [18] representing a major achievement towards the realisation of nonlinear photonics in compound semiconductor waveguides.

ULI has been demonstrated in Chapter 3 as a successful method for waveguide fabrication in ZnSe. Extending this to beyond the near-infrared region would provide the capability to fabricate integrated nonlinear photonic devices operating in the mid-infrared. In addition to these potential nonlinear passive devices, direct ULI inscription of mid-infrared waveguides in ZnSe could be extended to Cr^{2+} and Fe^{2+} doped substrates to realise mid-infrared waveguide laser cavities. Transition metal doped II-VI semiconductors such as Cr^{2+}: ZnSe, Cr^{2+}: ZnS, Cr^{2+}: CdSe and Cr^{2+}: $Cd_{1-x}Mn_xTe$ have demonstrated many desirable properties such as large bandwidths for absorption and emission, large emission cross-sections, no excited state absorption and room

temperature operation [8-10, 13, 86]. In particular, Cr^{2+}: ZnSe lasers possess emission cross-sections of $1.2x10^{-18}$ cm^2, approximately 3 times larger than that of Ti:sapphire, absorption bandwidths spanning 1500 – 2100 nm, and emission bandwidths of 1900-3400 nm. These attributes have led to Cr^{2+}: ZnSe having demonstrated room temperature CW output powers of 14 W [15], gain switched pulsed operation at 18.5 W [109] and continuously tuneable CW output from 1973-3349 nm [110]. Figure 4.1 shows a measurement of the emission and absorption cross-sections for a sample of Cr^{2+}: ZnSe. Despite these promising advancements, the power scaling of II-VI chromium lasers has long been held back by the high thermo-optic coefficient, $\frac{\partial n}{\partial T}$, of the host materials [86]. High irradiances lead to thermal lensing and self-focusing in the host material causing cavity instability and even optical damage in the gain medium. Consequently, thermal management is of upmost importance when power scaling these sources. Pump wavelength, crystal geometry and MOPA systems have all been investigated as potential means of managing the thermal lensing problem but the record CW power output remains capped at 14W [15]. A waveguide geometry offers an attractive solution to this problem by substantially reducing the effect of thermal lensing within the gain medium [111]. Perhaps more appealing is the compact and vibration insensitive nature of waveguide lasers. Direct diode pumping and optical coating of substrates could lead to the realisation of compact monolithic laser sources operating in the mid-infrared without components sensitive to misalignment through vibrations. These qualities are ideally suited to the applications outside of the laboratory and in some of the extreme environments that the aforementioned applications demand. ZnSe fibres have been fabricated with low propagation losses [18], but to date there have been no published results with Cr^{2+} doping. By extending ULI waveguide technology to Cr^{2+}: ZnSe media, waveguides could be inscribed in commercially available bulk samples. The integration of waveguide structures with direct diode pumping hold the potential for a whole range of compact, robust mid-infrared laser sources could be realised in applications outside of the laboratory.

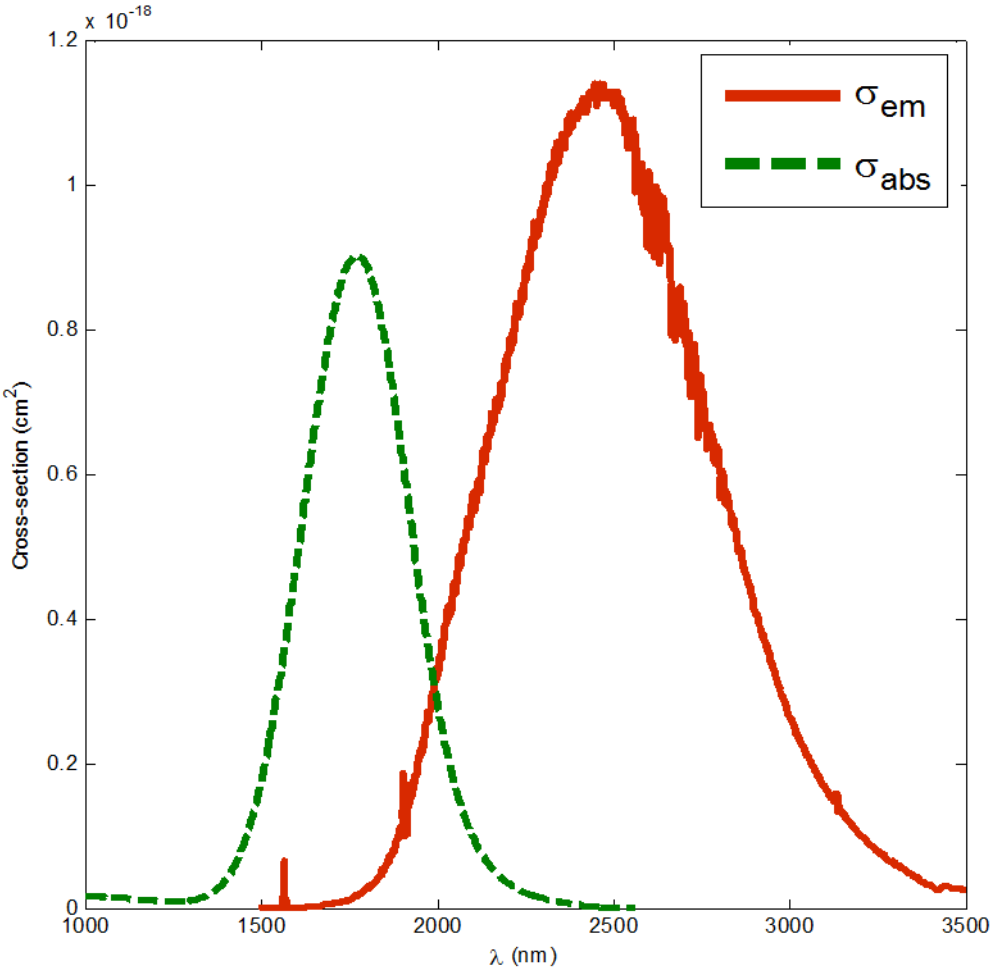

Figure 4.1. Absorption (green) and emission (red) cross-section measurements for Cr^{2+}: ZnSe. The absorption cross-section is a plot of a calculated value from the measured absorption coefficient and Cr ion concentration.

4.1 Waveguide design

Building from the work in Chapter 3, the type I waveguides were characterised at mid-infrared wavelengths using a 1928 nm Tm: Fibre laser source (AdValue Photonics) Unfortunately, a well confined mode was not observed and further development of the waveguide structures was therefore required to produce mid-infrared devices. Supporting longer wavelengths in the waveguide requires an effective lowering of the waveguide cut-off frequency. Assuming a step index contrast, the cut-off frequency is dependent on the waveguide index contrast and cross-sectional area. Therefore guiding at longer wavelengths can be achieved through either an increased refractive index

contrast or an increased cross-section. We can consider the implications of these two design modifications separately for simplicity. As index contrast is increased the confinement of longer wavelengths is possible and the number of waveguide modes at a given wavelength increases. For a single-mode structure, the mode size of a given wavelength supported by the waveguide decreases. This brings many benefits for nonlinear applications as smaller mode sizes provide access to higher irradiances. An increase in waveguide cross-section would also increase the number of waveguide modes at a given wavelength, however for single-mode structures the mode size increases resulting in decreased irradiances. It is important to note that for a fixed index contrast there exists an optimum cross-section for achieving the minimum mode size. Decreasing the cross-section further beyond this point will conversely increase the mode size resulting in large proportions propagating in the cladding region. We can also consider the implication of these effects for the fabrication of a waveguide laser cavity. Smaller mode sizes provide greater irradiances and therefore lower laser thresholds through greater gain at lower pump powers. Furthermore, the mode overlap of differing frequencies increases with index contrast. Consequently, it is important to find a waveguide design that correctly balances these factors for the viability of the end product.

Scaling of the waveguide cross-sectional area could employ a 2 x 2 array of multiscan modification blocks but this is prevented by the material damage observed above the waveguide core region. As this damage was present in all inscribed type I waveguides, an investigation into alternative inscription parameters that would yield a greater refractive index change was required.

4.1.1 Inscription parameter investigation

The ZnSe waveguides introduced in Chapter 3 demonstrated the lowest losses for a guided signal of 1550 nm when inscribed at the upper limit (190 nJ) of the available pulse energy using repetition rates of 2-3 MHz from the inscription laser. As the aim of the parameter investigation was to affect a higher index contrast it was necessary to access higher pulse energies, i.e. > 200 nJ. In order to access higher pulse energies from the IMRA laser system it was necessary to use lower repetition rates. The maximum

pulse energy available from the IMRA µJewel D400 inscription laser was 2.55 µJ however this required the laser to be operated at a repetition rate of 100 kHz due to the nature of the pulse picker system. A range of multiscan structures were inscribed in ZnSe at this repetition rate with the pulse energy varied from 100 nJ to 2.5 µJ. Pulse duration was once more considered as a key variable in the investigation however the limit of the pulse compressor on the IMRA laser system restricted maximum pulse durations to 1 ps at 100 kHz. Consequently, pulse durations of over the range of 500 fs - 1 ps were investigated. Inscription with pulse durations of 500 fs showed filament structures in agreement with previous results obtained using comparable pulse durations at higher repetition rates detailed in Chapter 3. However, structures fabricated using 750 fs and 1 ps pulses showed a range of substrate modification across a subset of the investigated pulse energies. The successful material modification at 750 fs is in contrast with the results at 2-3 MHz, however the results at 100 kHz still demonstrate a requirement for inscription using longer pulse durations of over 500 fs to avoid detrimental filamentation. Figure 4.2 shows the array of inscribed regions demonstrating the most uniform modification cross-sections achieved for 100 kHz repetition rates. These structure were inscribed using pulses energies ranging from 200 -900 nJ with pulse durations of 750 fs

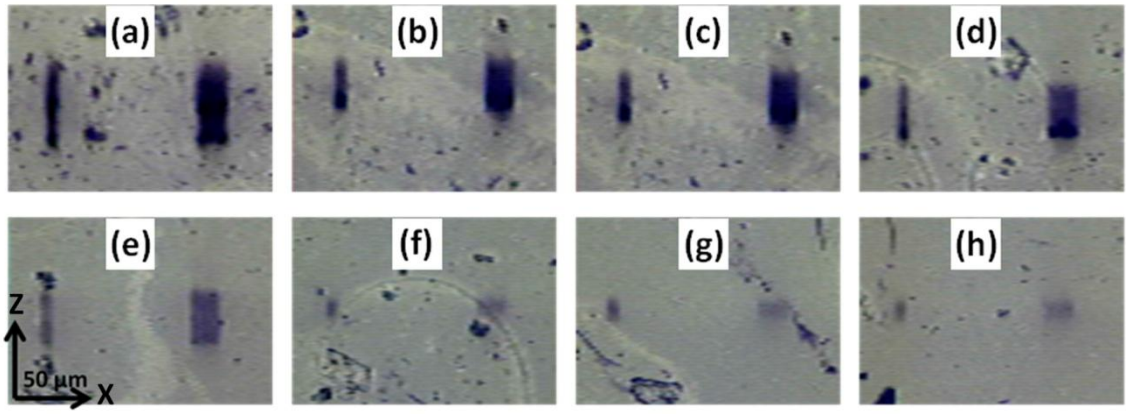

Figure 4.2. Montage image of modification with varying pulse energies. Each image section shows 2 overlapping scan (left) and 20 overlapping scans (right). The image shows a selection of modification regions decreasing in cross-section and apparent contrast with decreasing pulse energy . The pulse energies displayed are (a) 900 nJ, (b) 660 µJ, (c) 590 nJ, (d) 430 nJ, (e) 390 nJ, (f) 350 nJ, (g) 260 nJ and (h) 200 nJ.

In order to investigate the nature of the material modification the guiding properties of the structures were studied in a similar manner to the waveguide characterisation described in Section 3.3.1. This involved coupling a 1550 nm light source into a structure and imaging the emergent light at the opposite end facet onto an infrared camera. Upon characterisation no guiding was observed within the structures, they appeared dark with lower light intensities inside the modified region. In order to confirm whether the modification was manifesting as a reduction in refractive index it was proposed that ULI could be used to inscribe the waveguide cladding region rather than the core. Cladding-written waveguides of this nature have been demonstrated with ULI through inducing a localised reduction the material refractive index around an unmodified core region [56]. This creates a cladding waveguide structure with a cross-sectional area that can be easily tailored through control of the cladding dimensions.

4.2 Depressed cladding waveguides for the mid-infrared

The fabrication of a waveguide utilising a negative refractive index change requires the inscription of a cladding rather than a core region as is the case in type I waveguides. Such a structure consists of an unmodified region surrounded by a region of modified material with a localised reduction in refractive index. This type of structure is commonly referred to as a depressed cladding or w-type waveguide and the properties of such a structure need to be considered. For simplicity we will consider a one dimensional cross-section of one such waveguide. In this case we have a waveguide design that consists of inscribed cladding ‘walls’ surrounding an unmodified core which Figure 4.3 displays as a generalised refractive index profile.

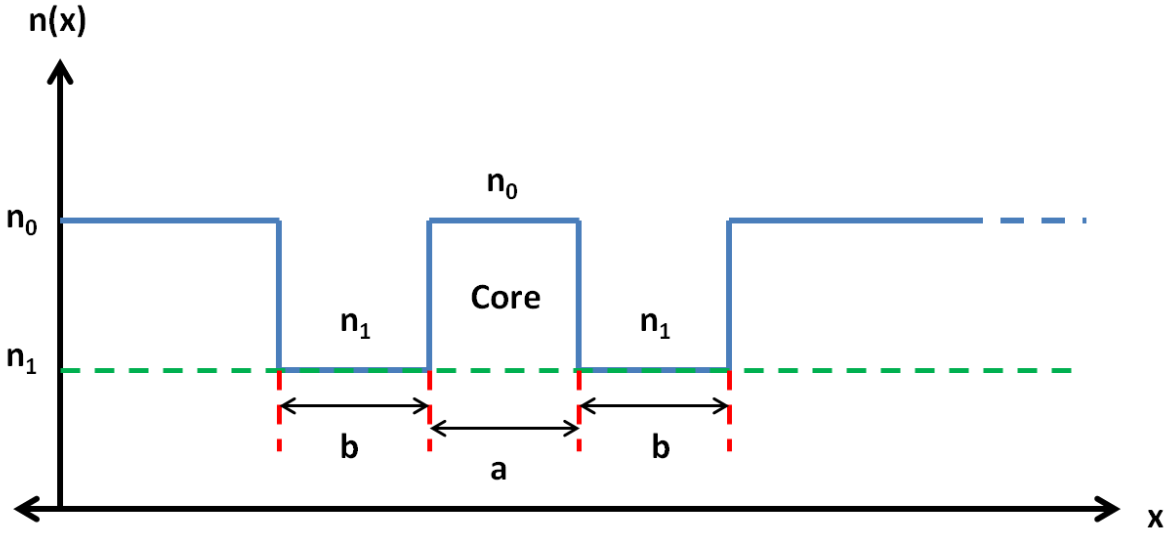

*Figure 4.3. Refractive index profile of a depressed cladding waveguide. **a** and **b** are the widths of the core and cladding region respectively.*

Through extensive modelling and theoretical analysis by Snyder and Love, and Hu and Menyuk, [112, 113] it has been shown that these depressed cladding waveguides do not support guided modes but instead support intensity distributions that while remaining similar in spatial distribution close to the core region, decay in intensity even in the absence of absorption or scattering. These decaying modes have been termed 'leaky' or 'tunnelling' modes [112-114]. It is useful to consider two limits to the case presented in Figure 4.3. In the first we will consider $b \rightarrow \infty$, under these conditions the structure becomes a conventional step index waveguide capable of supporting a number of lossless modes dependent on its core size and index contrast. In the other limiting case we can consider as $b \rightarrow 0$ and the medium becomes homogenous, supporting no guided modes but instead a spatial intensity distribution that diffracts as it propagates. For the work presented in this thesis leaky modes can be considered as behaving similarly to guided modes but with the important distinction that these leaky modes have an inherent exponential attenuation of intensity in the waveguide core. This means that a perfect depressed cladding waveguide which experiences no propagation losses due to absorption or scattering will still experience an exponential attenuation of the signal intensity in the core. This exponential attenuation is directly linked to the proportional dimensions of the cladding region and core region labelled **a** and **b** in Figure 4.3 [113].

For this reason the relative dimensions of the cladding and core regions must be considered in the waveguide design.

Depressed cladding structures fabricated through ULI have been previously demonstrated in polycrystalline Nd^{3+}: YAG by Okhrimchuk *et al.* [56]. This example used overlapping regions of modification which contained localised points of reduced refractive index. The multiscan modification regions demonstrated in ZnSe, Figure 4.2, are well suited to this structure design due to well defined rectangular cross-sections achieved. In order to limit the parameter range required for the optimisation of this structure, the waveguide cross-section was designed for ZnSe by multiplexing individual multiscan blocks with a translational offset between blocks orthogonal to the waveguide axis as illustrated in Figure 4.4.

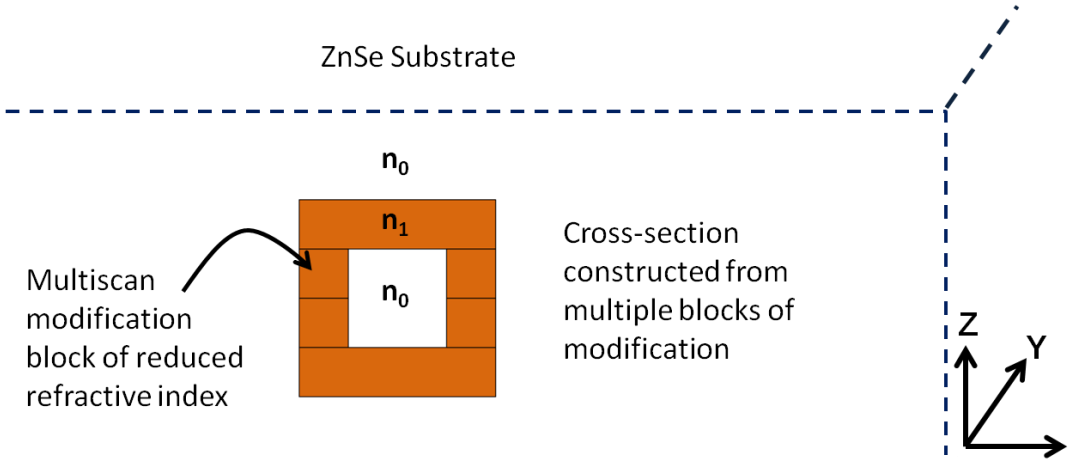

Figure 4.4 Cladding structure design constructed using an array of multiscan inscribed regions. A scale is not shown as this would vary with a given set of inscription parameters.

The structure design in Figure 4.4 could therefore be inscribed using the multiscan parameter space determined for 100 kHz repetition rate inscription and the dimensions of this structure could then be varied as part of the waveguide optimisation.

4.2.1 ZnSe mid-infrared waveguide inscription parameters

The cladding region of the waveguide was inscribed with the parameters corresponding to the modification shown in Figure 4.2. This required the investigation of pulse energies of 300-600 nJ in order to avoid the significant damage observed at higher pulse energies. As before the repetition rate was set to 100 kHz with a horizontally polarised beam. The individual scans in the multiscan structure were separated by 600 nm and the sample was translated through the inscription beam at 1.0 $mm \cdot s^{-1}$ in order to replicate modification observed in the inscription parameter investigation. The large multiscan blocks at the top and bottom of the structure were composed of 80 overlapping scans and the blocks used in the side wall regions were composed of 20 overlapping scans. These dimensions were designed to obtain a waveguide core with comparable dimensions to the cladding regions. The vertical offset of each block was a key design parameter with separations of 8 - 12 µm investigated across a range of structures. This parameter was investigated because the overlap of individual modification regions was expected to influence the final material modification. In effect, the overlapped areas can be compared to a region that has been subject to two separate, repeated inscription scans. The structure was inscribed starting with the lower block so as to avoid aberrations arising from focusing through modified material. Some variation was expected in the modification at different depths of inscription due to aberration in the focused inscription beam but this was not compensated for. Figure 4.5 shows the end facet of one such structure.

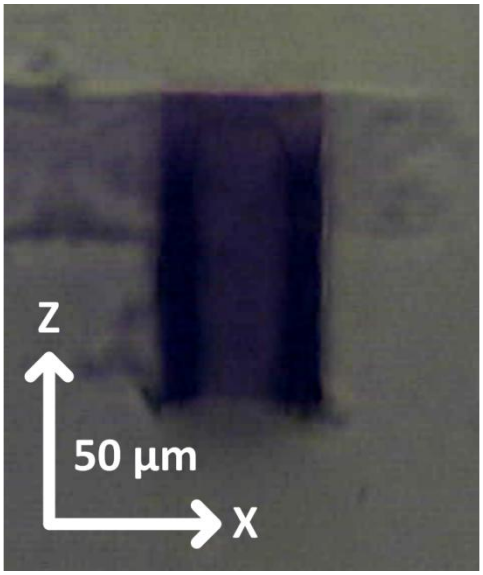

Figure 4.5. Microscope image taken in white light transmission displaying end facet of cladding written structure inscribed in ZnSe. The dimensions of the cladding measure 48 × 90 µm. The core region appears darkened as light from the microscope condenser lens could not be coupled into the small waveguide cross-section. Both Z and X axis arrows represent 50 µm.

4.2.2 Mid-infrared characterisation

Initial characterisation was carried out using a HeNe laser source operating at 3390 nm. As depicted in Figure 4.6, a $\frac{\lambda}{2}$ wave-plate and a linear polariser were used to control the power and linear polarisation axis of the 3390 nm source. The ZnSe sample was mounted on an XYZ microblock stage and the light was coupled into one end of the waveguide structure using a ZnSe objective (Innovation photonics LFO 5-12-2.0). The emergent light was collected at the opposite end of the waveguide and imaged onto an infrared camera (FLIR SC7000). After the alignment of the waveguide, the infrared camera was replaced with a photodetector and power meter for the subsequent insertion loss measurements.

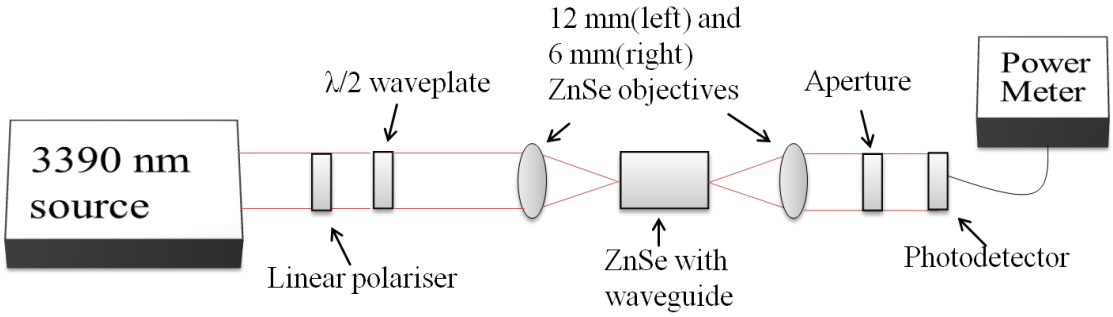

Figure 4.6. Experimental arrangement for mid-infrared waveguide characterisation at 3390 nm.

The structures were observed to support guiding of 3390 nm light with single-mode guiding demonstrated in the waveguide displayed in Figure 4.7. The mode showed a near 2-D Gaussian distribution with a slight asymmetry and dimensions measuring 25 x 36 µm to the $\frac{1}{e^2}$ intensity level.

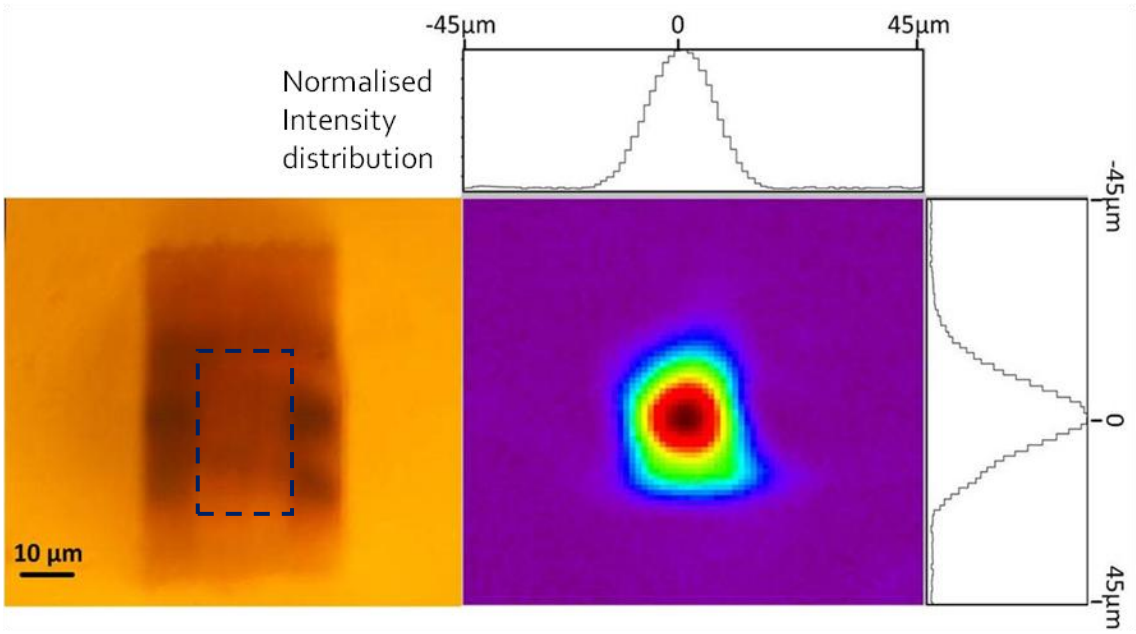

Figure 4.7. Cladding inscribed waveguide with central guiding region highlighted by blue dashed line box (left) and associated 3390 nm mode field intensity distribution of 25 x 36 µm to $\frac{1}{e^2}$ level (right). The core region of the waveguide appears dark as the microscope light source could not be coupled to the waveguide.

The propagation loss of the above waveguide was calculated to be 1.9 dB·cm^{-1}. This value was determined by subtracting the theoretical coupling losses from the measured total insertion loss. A detailed description of the total insertion loss measurement can be found in Section 3.2. Polarisation dependant propagation losses were investigated across only linear polarisation states by adjusting the $\frac{\lambda}{2}$ plate after the laser output. The power transmission through the waveguide was measured throughout a complete cycle of the $\frac{\lambda}{2}$ plate which showed polarisation dependant propagation losses to be 0.1 dB.

4.3Mid-infrared waveguides in Cr^{2+}: ZnSe

The successful fabrication of mid-infrared waveguides in ZnSe was a major milestone towards a host of integrated optical devices, and one which opens the door to the investigation of ULI waveguides in Cr^{2+}: ZnSe. The depressed cladding waveguides fabricated in undoped ZnSe were shown to be capable of guiding wavelengths over the entire emission range of Cr^{2+}: ZnSe (~ 2-3 μm). This is an important achievement that indicates the viability of the waveguides for use in tuneable waveguide laser cavities. Since guiding was observed at both extremes of the Cr^{2+}: ZnSe gain bandwidth this suggests the waveguide is potentially capable of laser output across the entire gain bandwidth.

In order to replicate the depressed cladding structures demonstrated in undoped ZnSe, the same parameters were applied to a polycrystalline Cr^{2+}: ZnSe substrate. The sample was fabricated by IPG photonics with a Cr^{2+} ion dopant concentration of 1 x 10^{19} cm^{-3}. However, the resultant structures were observed to be different that those fabricated in undoped ZnSe with the extent of modification appearing reduced in area. This is shown in a direct comparison of two structures fabricated using identical paramaters, displayed in Figure 4.8.

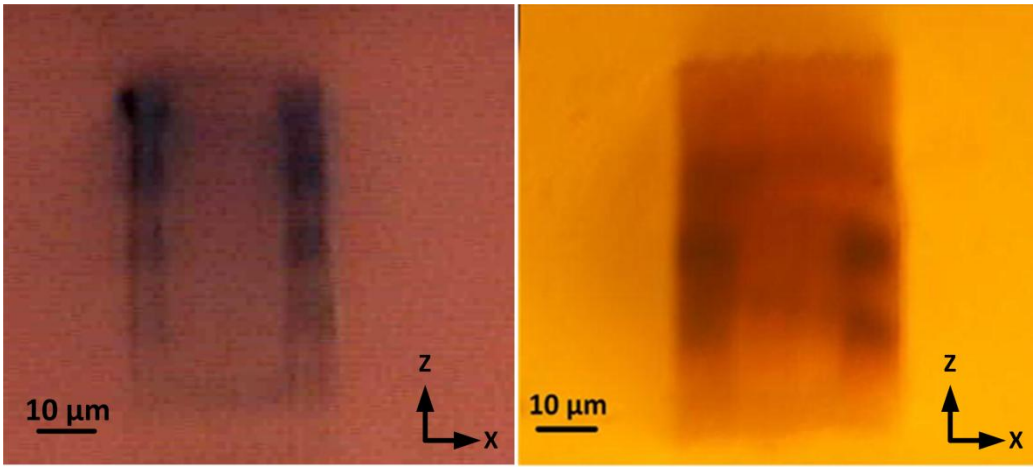

Figure 4.8. Comparison of depressed cladding waveguide structures fabricated using the same inscription parameters in Cr^{2+}: ZnSe (left) and undoped ZnSe (right). A distinct difference in the resultant structure in each material can be seen. The Cr^{2+}: ZnSe does not appear to have been modified to the same extent as the undoped ZnSe. For both micrographs the inscription beam was incident from above the image in the z-axis.

The waveguide structure in Cr^{2+}: ZnSe shown in Figure 4.8 did not demonstrate the same guiding properties of the structure in undoped ZnSe. Although confinement of light was observed in the horizontal direction, the vertical axis did not exhibit strong confinement and the supported mode was highly asymmetric, see Figure 4.9.

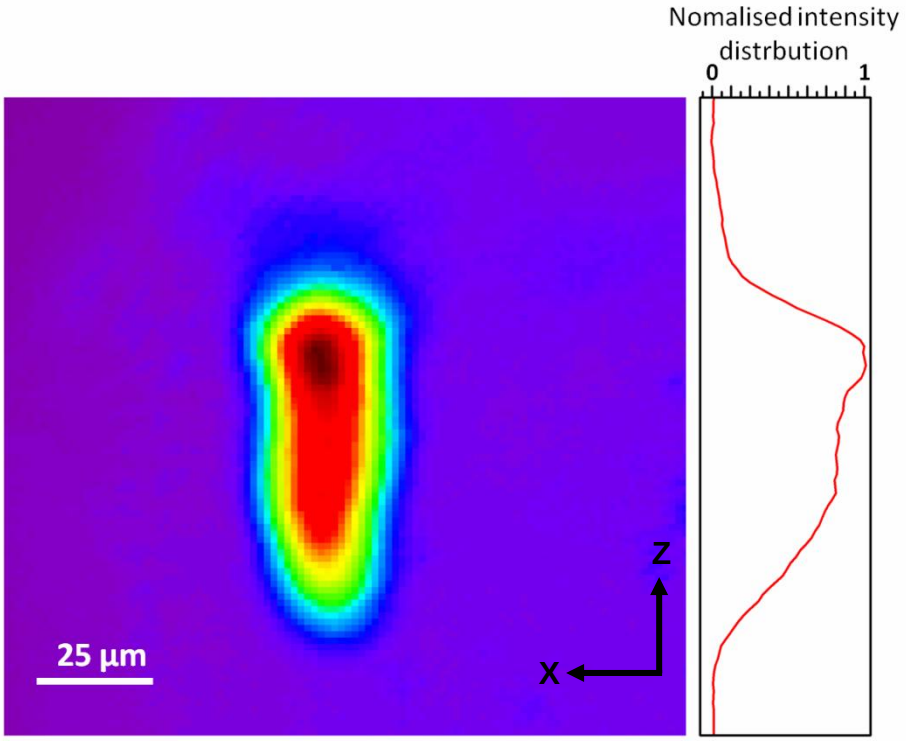

Figure 4.9. Highly asymmetric mode supported by depressed cladding waveguide in Cr^{2+}: ZnSe substrate. The poor confinement in the vertical z-axis is suspected to be due to the change in modification from ZnSe to Cr^{2+}: ZnSe shown in Figure 4.8.

On comparison with the waveguide cross-section image this it can be observed that the top and bottom cladding regions appear to exhibit a lesser degree of modification to that of the vertical regions on the left and right of the core, see Figure 4.8. A poorly confined mode in the vertical axis can therefore be explained by insufficient index contrast and cladding width in the vertical axis.

The origin of this substantial difference in material modification is not evident. The addition of Cr^{2+} ions as a dopant could contribute to this although as the Cr^{2+} ion concentration is low, approximately 0.04% atomic, this may not be the dominant factor. An additional factor in this discrepancy could be changes to the material as a result of the doping process in which the material undergoes heating to temperatures of 800-1100 °C [115]. As a consequence of this disparity in doped and undoped material modification, it was necessary to develop a new set of parameters for inscription in Cr^{2+}: ZnSe. As with the undoped ZnSe sample, an array of modification regions was

written over a range of pulse energies spanning 100 nJ to 2.5 µJ. This was carried out with the same parameters detailed in Section 4.1.1 and Figure 4.2 in order to serve as a direct comparison between the two materials. Through visual inspection and comparison of the resultant modification regions in Cr^{2+}: ZnSe and undoped ZnSe it was observed that the extent of modification was greater in undoped ZnSe than in Cr^{2+}: ZnSe for identical inscription parameters. The modification in Cr^{2+}: ZnSe suggests that higher pulse energies are needed to modify Cr^{2+}: ZnSe compared to that for undoped ZnSe A direct comparison of one such modified region highlights this and is shown in Figure 4.10.

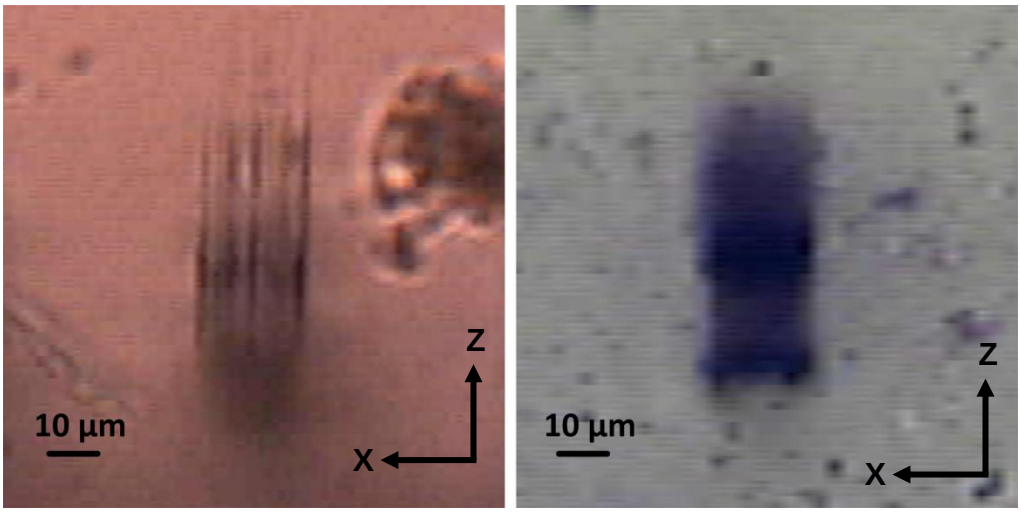

Figure 4.10. Comparison of multiscan structures fabricated using the same inscription parameters in Cr^{2+}: ZnSe (left) and undoped ZnSe (right). The Cr^{2+}: ZnSe can be seen to have a lesser degree of modification to that of undoped ZnSe. The difference in colour is a result of the Cr^{2+} doping.

Here we see that the modification in undoped ZnSe appears greater than the extent in Cr^{2+}: ZnSe. Visual inspection and comparison of the modified regions under optical transmission microscope allowed selection of inscription parameters that best suited the structure fabrication in Cr^{2+}: ZnSe. As the modification appears weaker in the Cr^{2+}: ZnSe inscription parameters Although no one modification region could be selected without quantitative measurements such as index profiling, the comparison of

structures in Cr^{2+}: ZnSe provided a narrower parameter space to investigate towards the fabrication of mid-infrared waveguides in Cr^{2+}: ZnSe.

4.3.1 Cr^{2+}: ZnSe mid-infrared waveguide inscription parameters

The inscription parameters developed from the visual comparison of doped and undoped ZnSe provide the grounding for waveguide fabrication in a Cr^{2+}: ZnSe sample. The observation that increased pulse energies were required motivated the investigation of 300-500 nJ pulses. These pulse energies could now be applied to the inscription process and the depressed cladding waveguide design fabricated in ZnSe to replicate the structures in Cr^{2+}: ZnSe. Aside from pulse energy, identical parameters to those employed for ZnSe inscription were used, i.e. 100 kHz, horizontal polarisation, 750 fs pulses and 1.0 $mm \cdot s^{-1}$ sample translation velocity.

The resultant structures were characterised at 3390 nm for comparison with the first Cr^{2+}: ZnSe depressed cladding structures. Figure 4.11 displays the mode profiles from the initial Cr^{2+}: ZnSe cladding structure compared to the new structures fabricated with pulse energies of 450 nJ. It can be observed that the vertical confinement in the new structures has only marginally improved with a reduction in the vertical mode axis of 20 µm. The mode remains asymmetric and, upon characterisation at 3390 nm, exhibited high propagation losses, $> 5\ dB \cdot cm^{-1}$, which would make laser operation highly inefficient even if the required gain could be achieved in the waveguide.

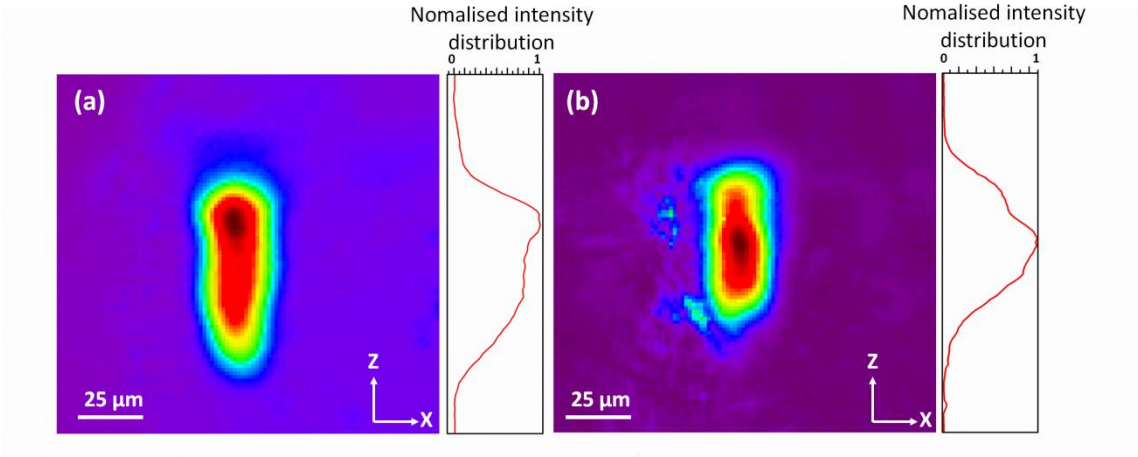

Figure 4.11. Comparison of waveguide modes from depressed cladding structures written with (a) low pulse energies, 300 nJ and (b) high pulse energies, 450 nJ. The structure fabricated using 450 nJ pulses, (b), demonstrates better confinement of the 3390 nm mode with a 20 µm reduction in the mode field z-axis diameter.

In order to reduce propagation losses an additional cladding region was proposed to improve performance, Figure 4.12. This design implemented a secondary outer wall, inscribed with greater pulse energies, to reduce tunnelling losses by increasing the cladding/core width ratio in the waveguide. The inscription of the outer cladding would utilise higher pulse energies than the inner cladding so as to achieve greater index contrast and further reduce tunnelling losses [113]. The investigated inscription parameters were again chosen through reference to the pulse energy investigation and the generated array of modification regions, a subset of which are displayed in Figure 4.2 and Figure 4.10. As no quantitative data of the refractive index contrast was available, the visual comparison under optical microscope provided the grounds for selecting a suitable parameter space. The inscription of the inner cladding wall was performed with low pulse energies, 300 – 500 nJ with the same cross-sectional design as previous structures in order to preserve the desirable features of a low refractive index contrast such as single mode like performance and low scattering losses. Added to this was the outer cladding subject to inscription with higher irradiances using pulse energies of 1 µJ.

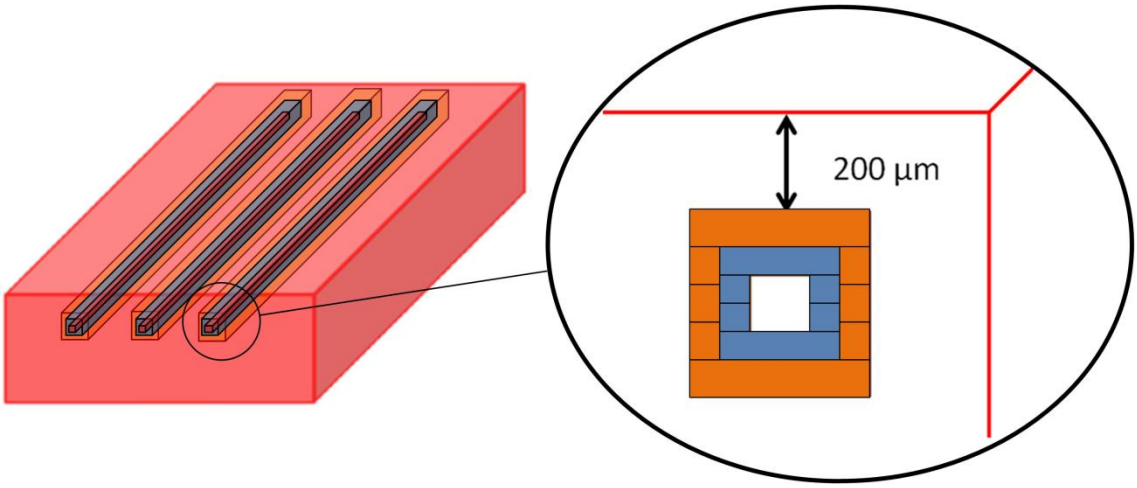

Figure 4.12. Illustration of double depressed cladding structures displaying two distinct cladding regions constructed from an arrangement of multiscan structures.

A vertical offset between adjacent multiscan blocks of 10 – 15 microns was investigated for the outer cladding as overlap between modified regions would be analogous to repeated inscription over the same region of material. As such, overlap of the multiscan blocks may contribute to the extent of the material modification.

The resultant structures demonstrated guiding at both the pump wavelength, 1928 nm, and the long wavelength limit of the Cr^{2+}: ZnSe emission band, 3390 nm. The mode field intensity images of these modes are shown in Figure 4.13.

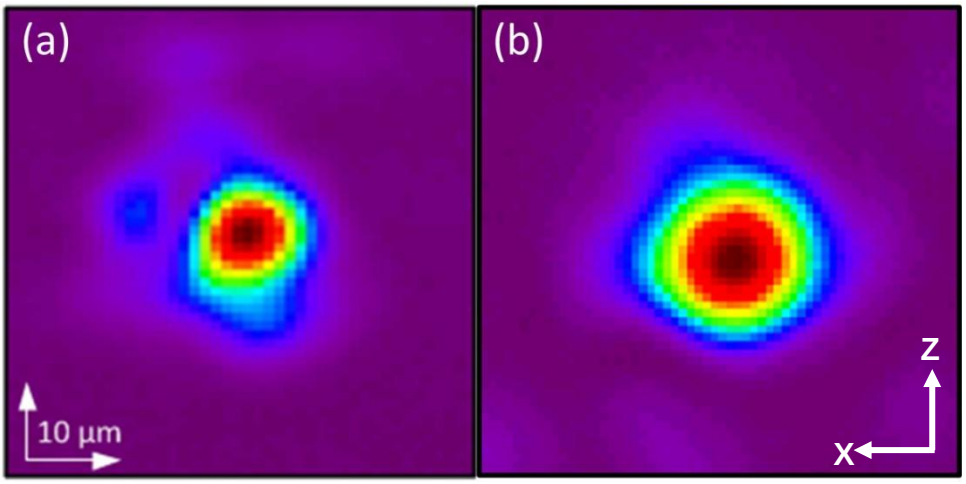

Figure 4.13. (a) Near-field image of the 1928 nm waveguide mode. (b) Near-field image of the 3390 nm waveguide mode, showing wavelengths beyond the emission band of Cr^{2+}: ZnSe

4.3.2 Mid-infrared Fabry-Pérot characterisation

As the waveguides demonstrated single mode guiding the propagation losses of the waveguide could be measured using the Fabry-Pérot method, Section 3.4. In this case, the Fabry-Pérot method utilised thermal tuning of the cavity length rather than a tuneable laser source. 2300 nm light supplied by a 30 mW CW laser diode (m2k lasers) was coupled into the waveguide using an AR coated ZnSe objective (Advanced Photonics). The emergent light was gathered at the opposite end of the waveguide using an identical ZnSe objective and collimated onto a pyroelectric power meter. The Cr^{2+}: ZnSe was mounted upon a heat sink connected to a closed loop chiller system which was used to vary the temperature of the sample and generate the Fabry-Pérot fringe set. From the recorded fringe sets a propagation loss of 3.5 $dB \cdot cm^{-1}$ was inferred. This is substantially higher than the 1.9 $dB \cdot cm^{-1}$ losses measured for the single cladding structures fabricated in undoped ZnSe. Upon inspection under optical microscope it was observed that the waveguide cladding suffered from substantial microcracking along the length of the waveguide. This cracking could account for the relatively high propagation losses in the double clad structures. Figure 4.14 displays a microscope image of the waveguide perpendicular to the direction of light propagation, showing microcracking throughout the cladding.

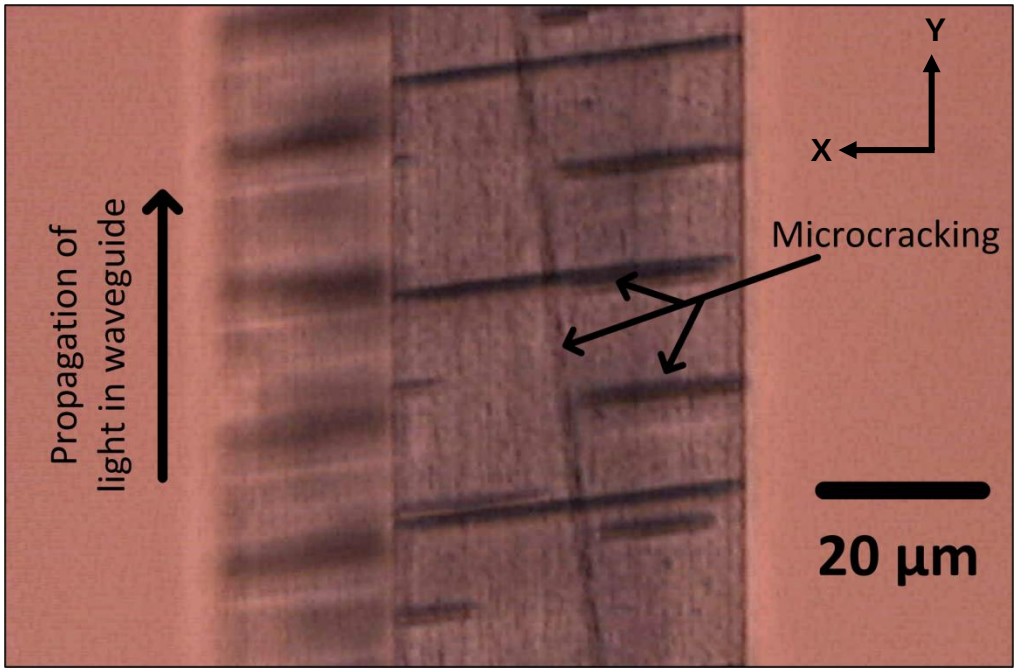

Figure 4.14. Microscope image taken with white light transmission of double clad waveguide structure displaying microcracking throughout the cladding.

The microcracking within the waveguide structures were investigated with a study into the influence of an outer cladding on their formation. This was conducted in undoped ZnSe due to limited sample space in Cr^{2+}: ZnSe.

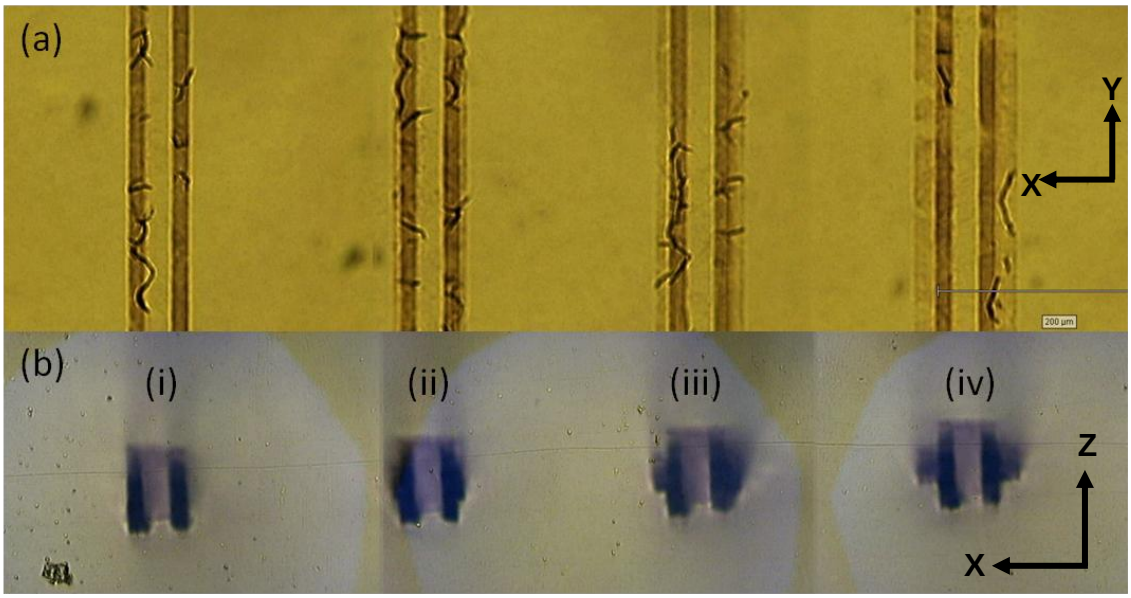

Figure 4.15. Microcracking in ZnSe waveguides with varying widths of outer cladding regions. Microscope white light transmission image are displayed (a) orthogonal to the waveguide propagation direction and (b) waveguide end facets with varying outer cladding regions inscribed (i) no outer cladding ,(ii) 5 µm,(iii) 10 µm and (iv) 20µm.

It can be observed in Figure 4.15 that microcracking occurs even in the case of no outer cladding. Moreover cracking appears predominantly in the side walls of the cladding and not in the central areas of the top and bottom cladding walls. This suggests that the cracking is linked to the vertical overlap of the multiscan modification blocks that form the depressed cladding. As this is an integral part of the waveguide structural design, investigations into alternative depressed cladding structures were also performed based on structures reported by Okhrimchuk *et al* [116].

4.4 Circular cross-section mid-infrared waveguides in Cr^{2+}: ZnSe

Depressed cladding waveguides fabricated using ULI have been demonstrated in other polycrystalline materials [56, 72] with propagation losses as low as 0.12 $dB \cdot cm^{-1}$ reported in Nd: YAG [116]. These waveguides in YAG substrates all feature a circular cross-section composed of many individual ‘lines’ of modification as illustrated in Figure 4.16.

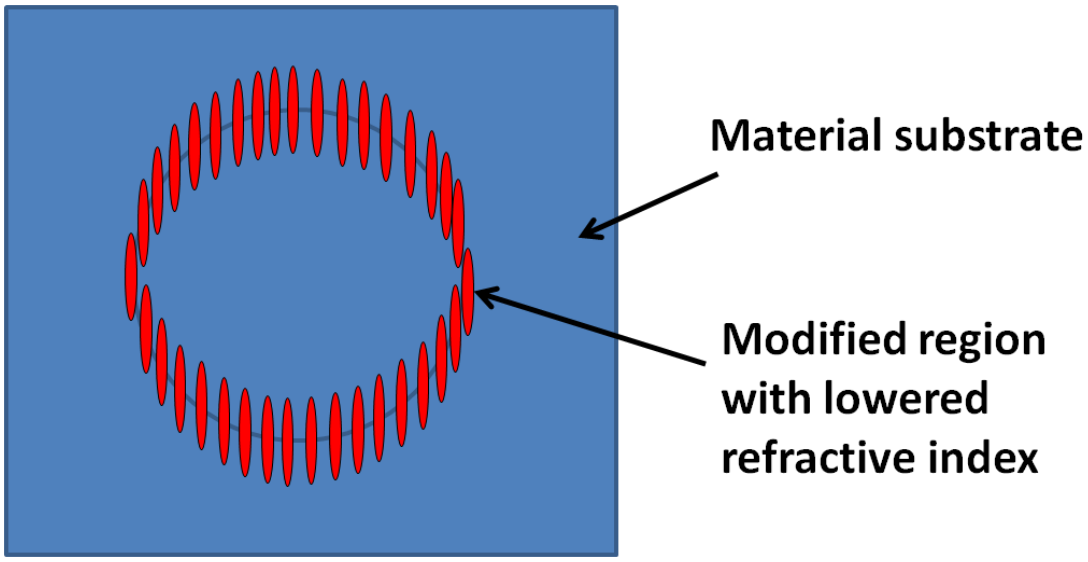

Figure 4.16. Illustration of circular cross-section depressed cladding waveguide composed of individual lines of modification.

The investigation of this structure design benefitted from the prior knowledge of the required inscription parameters, i.e. obtaining a negative refractive index change. A circular cross-section with elements equally separated in angle from the waveguide centre also offers a substantial reduction in the required parameter space for investigation by removing the scan separation parameter of multiscan structures as a key area of the structure optimisation.

4.4.1 Circular cladding fabrication

Before fabricating a circular cladding waveguide it was necessary to indentify the fabrication parameters of the individual modification elements that would be used to construct the intended waveguides. To this end, an array of single scan elements were inscribed in Cr^{2+}: ZnSe with pulse energies of 2.5 µJ at a range of sample translation velocities, 1 - 24 mm·s^{-1}. The maximum available pulse energies of 2.5 µJ were chosen to affect as much material modification as possible in a single sample translation. All other parameters remained unchanged from the negative refractive index modification investigation, using 100 kHz, horizontal polarisation, and 750 fs pulses. It was observed

that the height of the inscribed element cross-section was related to the translation velocity of the laser with higher velocities producing shorter modified regions.

A microscope image of this height variation is displayed in Figure 4.17. The origin of this effect is unclear however the structures appear to increase in length counter propagating to the inscription beam. This suggests that the initial material modification is seeding the growth of this structure in the Z-axis. As the spatial separation between pulses from the inscription laser is smaller for low translation velocities (10 nm at 1 $mm \cdot s^{-1}$) many pulses can be incident on the focal volume allowing a potential growth in the modification element. Further investigation of this effect is therefore required to fully explain this structure formation mechanism.

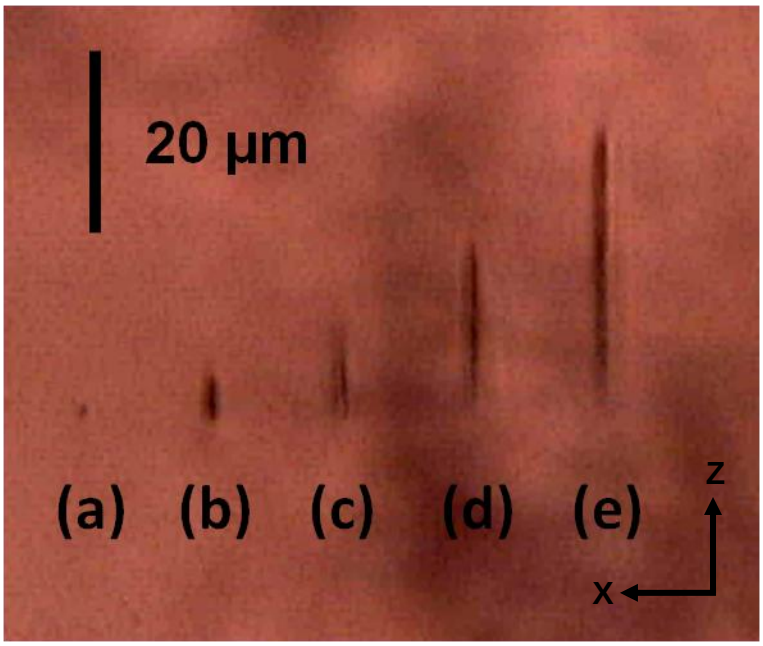

Figure 4.17. Microscope image of single scan modification elements inscribed with a range of sample translation velocities. (a) 27 $mm \cdot s^{-1}$, (b) 9 $mm \cdot s^{-1}$, (c) 3 $mm \cdot s^{-1}$, (d) 1 $mm \cdot s^{-1}$ (e) 0.3 $mm \cdot s^{-1}$. The inscription beam is incident from above the image in the z-axis showing that the modified elements increase in length counter to the beam propagation.

The ability to control the vertical dimension of the individual inscription elements provides more control over the fabrication of a waveguide structure with arbitrary

diameter. The modification achieved with a translation velocity of 9 mm·s^{-1} was chosen as it represented a compromise between the cladding thickness that could be achieved and the minimum structure diameter that could be inscribed without vertical overlap of the elements. Following this, a series of structures were fabricated with diameters ranging from 60 – 160 µm. An additional inscription parameter investigated in the fabrication of these structures was the number of repeated inscription scans over the same region, i.e. 'overscans'. This parameter differs from the multiscan in that each successive scan in inscribed over the same material region without an incremental offset in the horizontal axis. Overscan values of 1 - 50 were investigated for each structure. The pulse energy, polarisation and sample translation velocity are fixed to the parameters acquired in the investigation of the singular modification elements. Consequently, the effective parameter space for investigation was greatly reduced from previous structure fabrication.

4.4.2 Circular cross-section waveguide characterisation

The circular cross-section depressed cladding waveguides were characterised at wavelengths of 1928 and 2300 nm as representative pump and signal wavelengths for Cr^{2+}: ZnSe laser sources. The same system as described in Section 4.3.2 was used for imaging the mode field intensity distribution, i.e. 1928 and 2300 nm laser sources coupled into the waveguide and imaged onto a IR camera array using an f = 20 mm CaF_2 aspheric lens . Figure 4.18 displays images of a 120 µm diameter waveguide, a pair of waveguides with diameters of 80 µm and the mode field intensity distributions associated with the second 80 µm diameter structure.

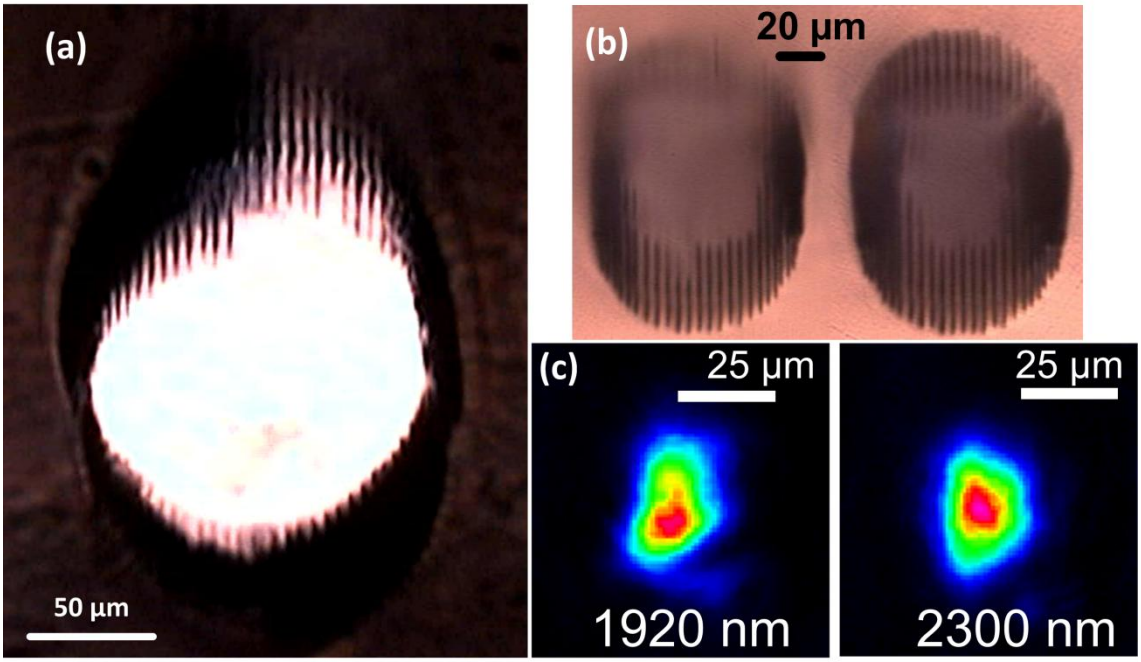

Figure 4.18. Circular cross-section depressed cladding waveguide. (a) Image of 120 µm diameter waveguide end facet taken by optical microscope in white light transmission mode. White light has been coupled into the waveguide from the microscope condenser lens. (b) 80 µm diameter waveguides inscribed with 10 overscans per element (left) and 25 overscans per element (right) (c) Modes supported by an 80 µm diameter waveguide at 1928 and 2300 nm representing pump and signal wavelengths of Cr^{2+}: ZnSe.

Figure 4.18(c) shows the observed modes at 1928 and 2300 nm with the waveguide and camera alignment unchanged in order to compare the spatial intensity distribution of the two modes. This demonstrates a good degree of spatial overlap for the representative pump and signal modes. Since the majority of these waveguide structures demonstrated multi-mode like behaviour, the propagation losses of the waveguides were not determined using the Fabry-Pérot method. The temperature tuning of these multi-mode waveguide cavities caused slight changes in modality and therefore would not produce simple Fabry-Pérot fringe sets. A Fabry-Pérot characterisation was attempted for the near single mode waveguides but the measurements were unrepeatable due to changes in waveguide modality with temperature variation. As a direct measurement of the propagation loss through Fabry-Pérot was not possible the decision was made to test the waveguide in a laser cavity and infer the propagation loss through the Findlay-Clay method [117]. The Findlay-Clay method allows the losses of a 4-level laser system to be determined through the analysis of a laser cavity threshold with varying proportions of

output coupling. The comparison of laser thresholds where cavity gain is balanced with cavity loss, the propagation losses of the waveguide can be determined.

4.5 Conclusions

This chapter has detailed the development of the first mid-infrared channel waveguides in ZnSe fabricated with ULI. Inscription parameter investigation at higher pulse energies > 200 nJ at 100 kHz were discovered to affect a localised negative change (i.e. a reduction) in the material refractive index. This allowed the fabrication of depressed cladding structures for the guiding of mid-infrared light. Single-mode like guiding was demonstrated for 3390 nm light with propagation losses as low as 1.9 $dB \cdot cm^{-1}$ making the structures viable for use in nonlinear optical applications in the mid-infrared such as spectral broadening for mid-infrared continuum generation. The achievement of mid-infrared guiding in ZnSe substrates also provides a potential fabrication method for mid-infrared waveguide laser sources in transition metal doped ZnSe media.

The fabrication of mid-infrared waveguides in Cr^{2+}: ZnSe was reported with two independent waveguide designs demonstrated. Successful inscription parameters previously developed in undoped ZnSe failed to replicate comparable waveguide structures in Cr^{2+}: ZnSe. An investigation into inscription parameters in Cr^{2+}: ZnSe and their comparison with undoped ZnSe parameters was therefore carried out. This yielded a modification regime in Cr^{2+}: ZnSe comparable by visual inspection to that observed in undoped ZnSe. The results demonstrated that an increase in pulse energy of approximately 50% was required for Cr^{2+}: ZnSe inscription compared to undoped ZnSe. Using these reoptimised parameters double depressed cladding waveguides were fabricated in Cr^{2+}: ZnSe demonstrating guiding at either limit of the material emission range, 1928 and 3390 nm. This suggests the structures are suitable for use in a waveguide laser cavity, although a propagation losses of 3.5 $dB \cdot cm^{-1}$ could prove limiting for the performance of the waveguide laser.

Further to this, a circular cross-section waveguide was investigated based on a design demonstrated by Okhrimchuk *et al.*[116]. These structures were successfully demonstrated with a range of diameters from 60 – 160 μm, and both multi-mode and single-mode like performance observed at pump and signal wavelengths of Cr^{2+}: ZnSe at 1928 and 2300 nm. Although a direct loss measurement of propagation losses was not possible, the waveguides supported the required mid-infrared wavelengths with good spatial overlap of each respective guided mode.

The development of mid-infrared waveguides in Cr^{2+}: ZnSe marks an important milestone in progress toward a mid-infrared Cr^{2+}: ZnSe waveguide laser source. The waveguides demonstrate guiding properties across a wavelength range that render them suitable for application as waveguide laser cavities and pave the way for the first Cr^{2+}: ZnSe channel waveguide laser.

Chapter 5 will discuss the laser gain medium Cr^{2+}: ZnSe and the construction and demonstration of a waveguide laser cavity using the two types of ULI waveguide presented in this chapter.

Chapter 5 - Mid-infrared Cr^{2+}: ZnSe waveguide lasers

Laser sources in the mid-infrared region of the electromagnetic spectrum were initially sparse in number without the range of sources that emerged through semiconductor diode laser technology. The limited sources available fell into two main categories: Gas lasers such as CO, CO_2 and HeNe; and lead salt lasers. HeNe lasers offer a mid-infrared emission at 3.39 µm, CO at 4.8 – 8.3 µm and CO_2 offers output at 9.4 or 10.6 µm which could be frequency doubled to access wavelengths around 5 µm. Lead salt lasers could provide much wider tuneability ranges than those offered by gas lasers but require cryogenic temperatures to operate. For example, PbSnTe has demonstrated tuneability over 8.5 – 15.9 µm but this requires temperature tuning over the range of 50K to 110K [118]. These broad tuneability ranges were also possible through indirect nonlinear systems such as optical parametric oscillators (OPOs) and difference frequency generation (DFG) systems [119-122], but the systems are generally complex and highly environmentally sensitive with large area footprints making them impractical for many applications outside of the laboratory. Consequently, the development of the quantum cascade laser (QCL) effectively replaced lead salt diode technology and many nonlinear systems for applications in the mid-infrared.

QCLs brought higher efficiencies and later room temperature operation with wall plug efficiencies of over 10% [123] and 40% at cryogenic temperatures [124]. These properties, along with the variety of wavelengths available, allowed the devices to become more readily used in applications outside of the laboratory. Despite the benefits of QCL technology, average powers of > 1W are not available and sources below 4 µm are challenging to manufacture [125]. Recent progress in transition metal doped II-VI semiconductors has provided access to commercially available sources capable of operating at room temperature in the 2 - 3 µm region with CW powers up to 13 W [16]. Multi-watt tuneable sources have been developed demonstrating over 400 nm of CW tuneabilty at average powers exceeding 1W across the tuning range [15]. Tuneable laser sources in the mid-infrared are required for a number of spectroscopy based applications. The location of many molecular absorption lines over 2 – 5 µm make tuneable sources in this region powerful tools for technologies such as breath analysis

[126], laser surgery [127], and pollutant detection [128-130] to name a few. Currently, these applications predominantly employ QCLs as the tuneable mid-infrared laser source. However, to date QCL technology does not offer a complete package of high power > 100 mW, wide tuneability e.g. > 20% central wavelength, and room temperature operation at wavelengths below 5 µm. TM doped II-VI semiconductors already offer improved performance in the 2 – 3.5 µm region with various materials offering pulsed and CW tuneable sources such as Cr^{2+} doped ZnSe, CdSe and ZnS [9, 13-15, 131]. The wide gain bandwidth of Cr^{2+}: ZnSe has been exploited in bulk laser systems to achieve tuning ranges as large as 1973-3349 nm [110]. In comparison to QCL sources in this 2-3.5 µm region, Cr^{2+}: ZnSe laser offer advantages in access to higher powers and wider tuneability.

5.1.1 Cr^{2+}: ZnSe mid-infrared emission

Cr^{2+}: ZnSe has been dubbed by many as "the Ti: Sapphire of the mid-infrared" due to the many similarities of the gain media characteristics. The wide gain bandwidth offered by both these materials is due to vibronic broadening in the material in which photon emission is closely coupled to emission of vibrational phonons in the crystal lattice. This photon-phonon coupling allows the formation of energy sublevels which create an energy band allowing laser transitions to take place over a range of energies and hence providing broad tuneability [132, 133]. This photon-phonon coupling occurs over a fast enough timescale (<< radiative decay) for each ion to contribute to the laser emission in a homogenously broadened system. In Cr^{2+}: ZnSe, the energy transitions occur between the $^5T_2$ state and the first excited ^5E states providing output around the 2 - 3 µm region [134, 135]. Figure 5.1 displays a schematic energy level diagram for the Cr^{2+} ion in ZnSe and the sublevel energy bands created in a vibronic gain medium. Splitting of the ^5D state by the crystal field provides the $^5T_2$ and ^5E states with further splitting arising from the Jahn-Teller effect [136].

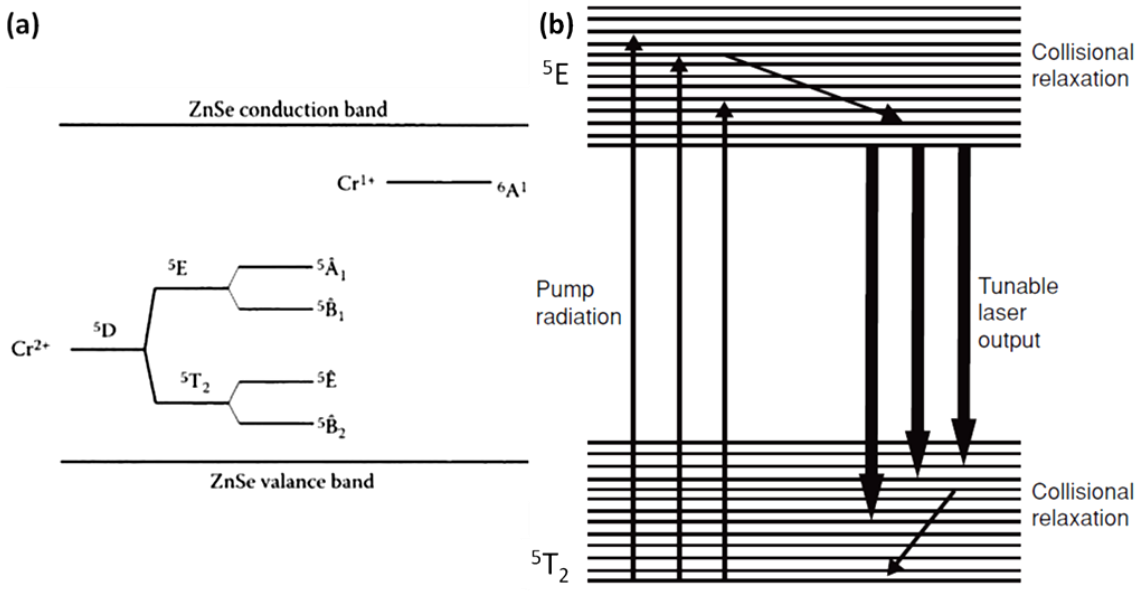

Figure 5.1. Energy level diagram of the Cr^{2+} ion in Cr^{2+}: ZnSe. (a) shows the splitting of the ^5D level due to the crystal field and Jahn-Teller effect. (b) shows a schematic diagram of the energy sublevels present in vibronic medium with the two laser emission states of Cr^{2+}: ZnSe, ^5E and $^5T_2$. Images taken and edited from (a) [137] (b)[133].

The broad absorption bandwidth, 1500 – 2150 nm, in Cr^{2+}: ZnSe provides flexibility in choosing a pump source with Tm^{3+}: fibre and Ho^{3+}: YAG lasers operating towards the long wavelength side at 1800 – 2100 nm and Er^{3+}: fibre lasers towards the short wavelength side at 1500 – 1600 nm. Direct diode pumping is also possible with the development of high power InGaAsP laser diodes emitting in the 1450 – 1800 nm region [138], see Figure 4.1 for the absorption and emission cross-sections of Cr^{2+}: ZnSe. In addition to wide tuneability the wide gain bandwidth is also beneficial for the generation of short pulses [133]. The comparison with Ti: sapphire sources remains cogent in this area with Cr^{2+}: ZnSe lasers producing sub-100 fs pulses through Kerr-lens mode-locking based on the understanding of these phenomena gained from Ti: sapphire lasers in the near-IR. [139, 140]. Table 5.1 displays a comparison of various Ti: sapphire and Cr^{2+}: ZnSe material properties.

	Cr^{2+}: ZnSe	Ti: Sapphire
Thermal conductivity	$18 W \cdot m^{-1} K^{-1}$	$28 W \cdot m^{-1} \cdot K^{-1}$
Thermo-optic coefficient, $\frac{\partial n}{\partial T}$,	$7.0 \times 10^{-5} K^{-1}$	$1.2 \times 10^{-5} K^{-1}$
Third order nonlinearity (at 1.6 μm)	$180 \times 10^{-20} m^2 \cdot W^{-1}$	$3 \times 10^{-20} m^2 \cdot W^{-1}$
Second order nonlinearity	$30 pm \cdot V^{-1}$	Absent (centrosymmetric)
Band-gap	2.83 eV	8 eV
Peak emission cross section, σ_{ems} at wavelength λ_0	$13 \times 10^{-19} cm^2$ at 2450 nm	$4.5 \times 10^{-19} cm^2$ at 780 nm
Fluorescence bandwidth, $\Delta\lambda$	~1300 nm	~ 450 nm
Relative bandwidth, $\frac{\Delta\lambda}{\lambda_0}$	0.53	0.58
Peak pump cross-section, σ_{ems} at λ_{abs}	$11 \times 10^{-19} cm^2$ at 1780 nm	$0.65 \times 10^{-19} cm^2$ at 500 nm
Upper state lifetime at room temperature	6 μs	3 μs

Table 5.1. Comparison of material properties with Cr^{2+}: ZnSe and Ti: sapphire. Data taken from Slobodchikov and Moulton [141].

A major challenge associated with the power scaling of Cr^{2+} lasers has been the high thermo-optic coefficient, $\frac{\partial n}{\partial T}$, of the II-VI host materials. Cr^{2+}: ZnSe has a thermo-optic coefficient of $7 \times 10^{-5} K^{-1}$ [86], which is approximately 4 times that of YAG and almost 6 times that of sapphire. As discussed in Chapter 4, high incident irradiances cause thermal lensing in the host medium and self-focussing which can lead to cavity instability and even optical damage [15]. This has been overcome in part through careful consideration of thermal management and system configuration [15, 131], but a waveguide geometry can greatly reduced the effect of thermal lensing [111], providing a route to higher powers than the current record of 14 W.

As Cr^{2+}: ZnSe sources reach maturity it would be advantageous to develop robust systems and products in order to bring these laser sources to more applications outside of the laboratory. In addition to alleviation of the thermal lensing problems waveguide laser sources can offer superior environmental stability to bulk lasers potentially

allowing for directly diode pumped monolithic mid-infrared sources. The overlap between the emission spectrum of Cr^{2+}: ZnSe with atmospheric absorption lines has created difficulties for short pulse modelocked sources, destabilising modelocking. This problem can also be greatly reduced for waveguide lasers as freespace sections can be removed [141]. For tuneable CW applications, the use of external cavity configurations similar to those pioneered for dye lasers [142], and more recently exploited for external cavity diode lasers (ECDLs) [143, 144], could provide compact waveguide lasers capable of nearly equalling the tuneable ranges for bulk systems. The previous chapters have demonstrated the viability of ULI for the fabrication of mid-infrared waveguides in Cr^{2+}: ZnSe, in this chapter these waveguides are built into a cavity and laser performance is investigated.

5.2 Double depressed cladding Cr^{2+}: ZnSe waveguide laser

The double clad waveguides described in Chapter 4, Section 4.3 demonstrated the required guiding properties at wavelengths suitable for a Cr^{2+}: ZnSe laser source. In order to study laser operation and performance of these waveguides, a simple cavity was constructed by butt-coupling a dichroic input mirror and an output coupler (Layertec GmbH) to opposite end facets of the waveguide. The input dichroic mirror was anti-reflection coated for the pump wavelength, 1928 nm, and highly reflective (HR) for 2050 -2430 nm. The output coupler was 80% reflective over the wavelength range of 1700 – 2700 nm. Both mirrors and the Cr^{2+}: ZnSe sample were mounted on a water cooled copper heat sink and each mirror was fixed to the waveguide end facets using an optical coupling compound (Thorlabs G608N3). Figure 5.2 and Figure 5.3 show an illustration of the mounted laser cavity and the eintire laser charcterisation arrangement.

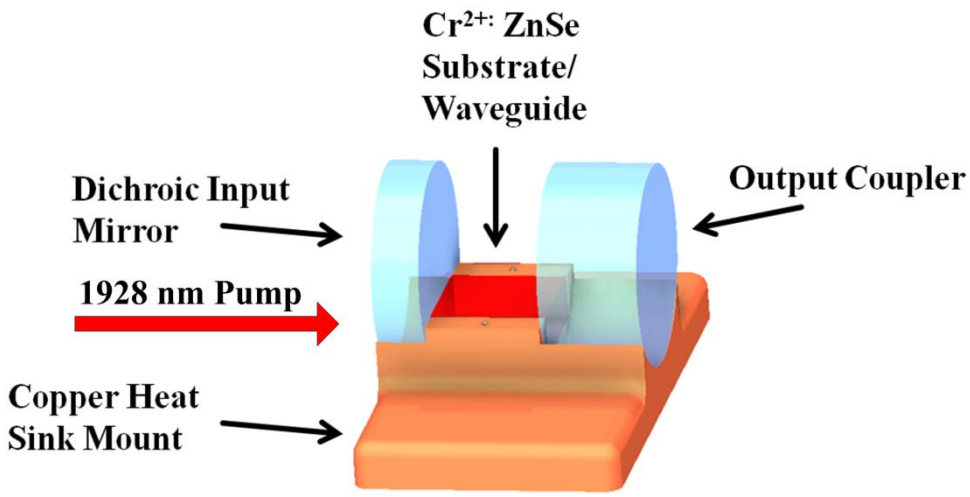

Figure 5.2. Illustration of passively aligned waveguide laser cavity. Mirrors are butt-coupled to the waveguide end facets using an optical coupling compound and held in scallops in the copper heat sink.

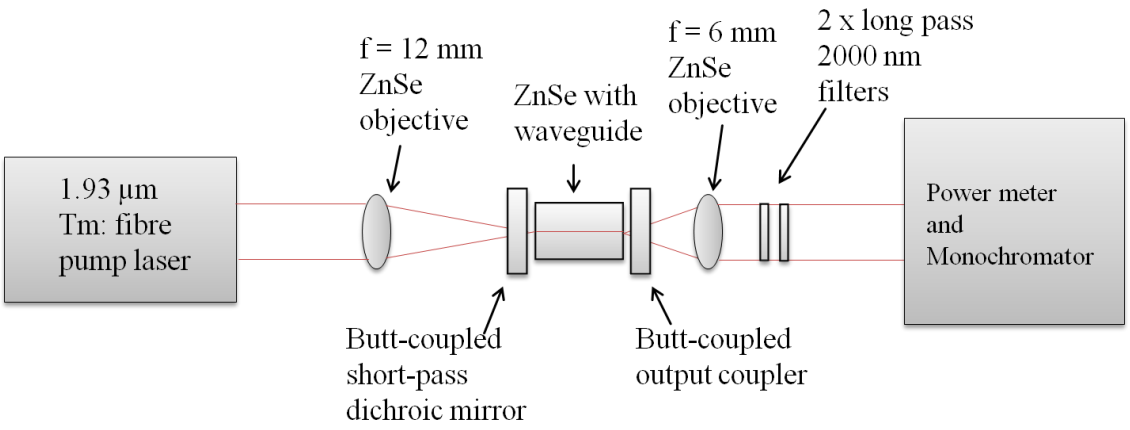

Figure 5.3. Schematic of Cr^{2+}: ZnSe passively aligned waveguide laser cavity, pump and characterisation equipment.

The 1928 nm pump was coupled into the waveguide using an AR coated 12 mm focal length ZnSe objective (Innovation Photonics). The emergent unabsorbed pump light was then gathered using an AR coated 6 mm focal length ZnSe objective and imaged onto an infrared camera array (FLIR SC7000). For power measurements the camera was replaced with a pyroelectric power meter (Laser Probe Inc. RKP-575) and two long pass filters (Spectrogon LP2000) were used to filter >99.99% of the residual 1928 nm pump. Initial alignment was performed by maximising the intensity of the imaged mode at

1928 nm. Following this initial alignment, the amplified spontaneous emission signal was imaged onto the camera and final alignment adjustments were made to optimise this signal. As the pump power was increased a threshold for lasing was observed at 700 mW of incident pump power. The laser output spectrum was analysed using a 300 mm monochromator (Gilden Photonics) and demonstrated an output peak centred at 2573 nm with a full width half maximum (FWHM) line-width of 2 nm. This is shown alongside the 2573 nm mode intensity distribution imaged by the FLIR IR camera in Figure 5.4.

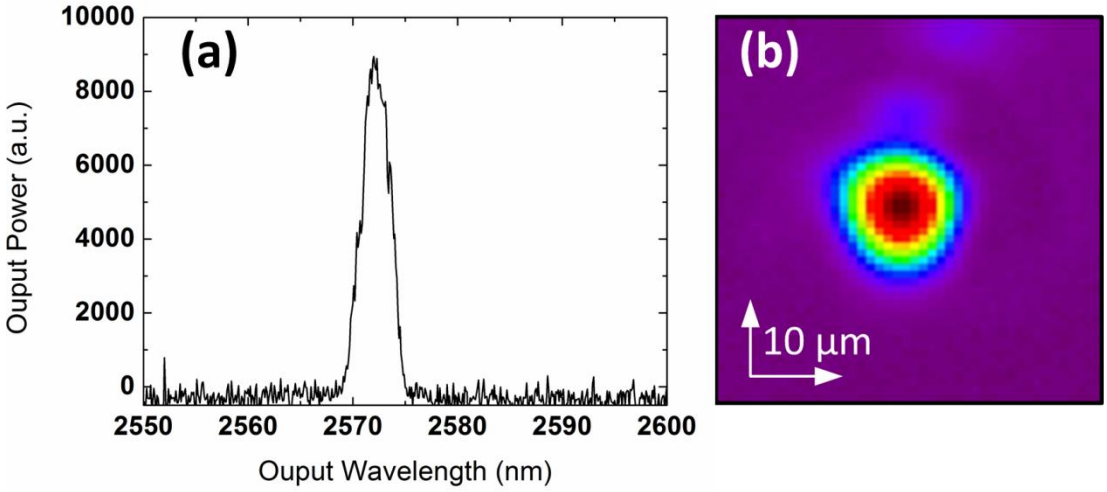

Figure 5.4. (a) Laser output spectrum centred at 2573 nm with FWHM line-width of 2 nm. (b) 2573 nm laser output mode profile.

The laser output power was then measured for a range of pump powers to determine the laser slope efficiency of 2.5% and a maximum output power of 18.5 mW for 1210 mW of pump, see Figure 5.5. It should also be noted that the incident pump power after subtraction of Fresnel reflections is presented rather than the absorbed pump power. Given that the coupling loss of the system could not be easily measured, the value of incident pump was quoted, providing a minimum value for the efficiency of the laser system.

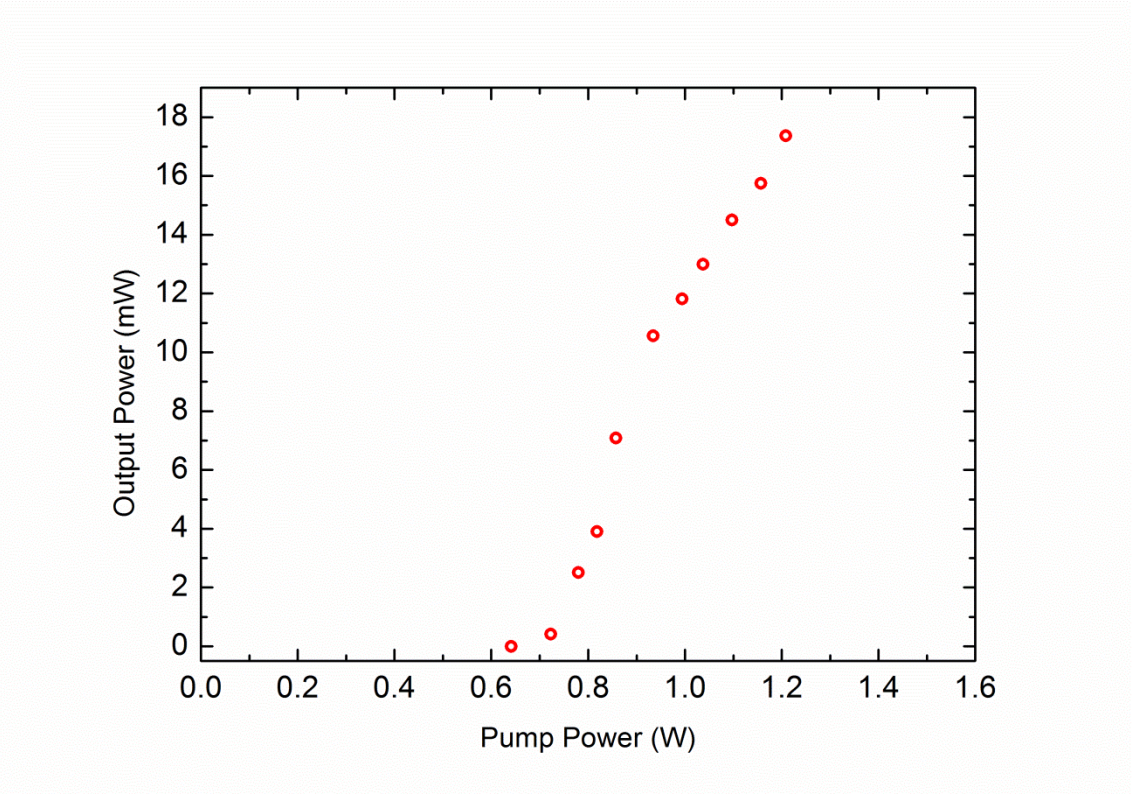

Figure 5.5. Input-Output characteristics of the double depressed cladding Cr^{2+}: ZnSe waveguide laser. The slope efficiency is taken from the 6 data points at the highest pump powers.

The laser characteristics demonstrate a clear change in slope efficiency for data points above 900 mW of pump power. This is likely to be due to alterations in pump light coupling and waveguide modality arising from thermal effects such as the thermo-optic effect and thermal expansion. The thermo-optic effect will change the refractive index profile of the waveguide, raising the refractive index in region of highest intensity, this in turn has an effect on the modes supported by the structure, potentially affecting pump and signal mode overlap and causing additional propagation losses due to changes in the refractive index profile along the length of the waveguide. The thermal expansion of the waveguide will increase the length of the sample, this has two effects. The first is that the mirrors will have a force exerted on them by the sample, they will likely lose alignment with the waveguide as they are butt-coupled off-centre on the mirrors. The second is that the pump light will no longer be focussed at the waveguide end facet, reducing coupling efficiency into the waveguide. As such an initial slope efficiency of 4.8% was obtained for pump powers of 700 – 900 mW while a slope efficiency of 2.5%

was determined from the final 6 data points above 900 mW. The maximum output power of 18.5 mW equates to an optical to optical efficiency of 1.5%.

Laser threshold was achieved in a Cr^{2+}: ZnSe channel waveguide laser for the first time. The low slope efficiency of 2.5% is due to large cavity round trip losses. These round trip losses are dominated by the high propagation loss of 3.5 $dB \cdot cm^{-1}$ contributing 4.2 dB to round trip losses for the 6mm waveguide. Reduction of the propagation loss through further optimisation of the waveguide inscription process would provide a significant increase in laser efficiency.

5.3. Circular depressed cladding Cr^{2+}: ZnSe waveguide laser

The double clad waveguides introduced in chapter 4 were built into a working laser in section 5.2.However, the system demonstrated low efficiencies of 2.5% and further optimisation of these structures was difficult due to the long inscription time for each waveguide, approximately 180 minutes, and the very large number of parameters. For this reason an alternative structure was investigated based on the circular cross-section depressed cladding structures demonstrated by Okhrimchuk *et al.*[56] in Nd^{3+}: YAG. These featured large diameters of >100 µm and proved suitable for high power operation, they were also highly multimodal [116]. Propagation losses as low as 0.12 $dB \cdot cm^{-1}$ were demonstrated making the structures a very attractive prospect for waveguide laser fabrication. The demonstration of these highly multi-mode structures at 1 µm soon led to their extension to longer wavelengths in the near-infrared and mid-infrared at 1.9 µm and 3.39 µm [145]. This work also encompassed the development of circular cross-section waveguides with greatly reduced diameters of 36 µm offering single mode guiding in the mid-infrared at 3.39 µm. Subsequent application of these structures by Ren *et al.*[72] to Tm^{3+}: YAG substrates led to the demonstration of a 2 µm laser operating with a 27% slope efficiency.

5.3.1 Laser cavity construction

The successful realisation of circular cladding structures in Cr^{2+}: ZnSe comparable to those demonstrated in YAG [116, 145] was detailed in Chapter 4. This allowed the construction of a waveguide laser cavity using the 80 and 120 µm diameter waveguides reported in Section 4.4. Due to the observed reduction in slope efficiency above 900 mW for the previous structure, see Figure 5.5, a new cavity design was implemented allowing for control of the pitch, yaw and z-axis (parallel to waveguide) of the mirrors. The mirrors were now also independently supported so expansion of the substrate would not change their angle. Figure 5.6 displays a schematic of the actively aligned Cr^{2+}: ZnSe waveguide cavity.

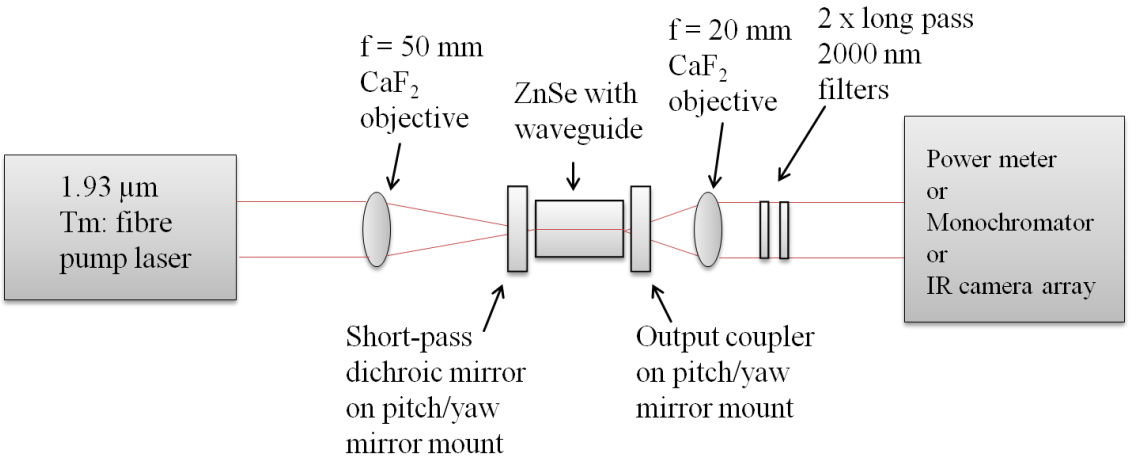

Figure 5.6. Schematic of Cr^{2+}: ZnSe actively aligned waveguide laser cavity using pitch, yaw and z-axis control mirror mounts for cavity mirror alignment.

The cavity aligned using an infrared camera array (FLIR SC7000) for initial signal optimisation. The laser performance was characterised with a dichroic input mirror, HR over 2050 - 2430 nm, and output couplers with 99%, 80%, 70% and 60% reflectivity (Layertec GmbH). Laser performance was also characterised without the use of a dielectric output coupler. For this cavity feedback was provided by the Fresnel reflection from the Cr^{2+}: ZnSe-air interface, giving a reflectivity of 18%. The highest output power and slope efficiency were achieved using the 60% reflective output

coupler reaching a maximum power of 285 mW for 1090 mW of 1928 nm pump and a slope efficiency of 45%. This corresponds to an optical to optical efficiency of 26%.

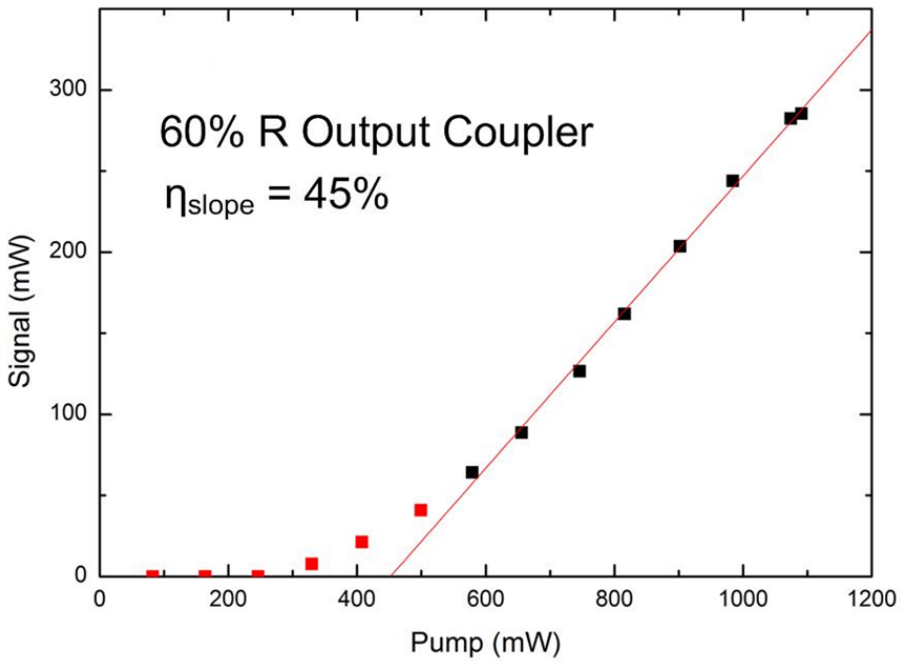

Figure 5.7. Laser performance with 60% reflective output coupler. Slope efficiency line has been fitted using the black data points

The optical to optical efficiency of 26% is a highly significant improvement from the value of 1.5% demonstrated by the passively aligned cavity. However, commercial Cr^{2+}: ZnSe bulk systems operate with optical to optical efficiencies as high as 70% [16]. In order to compare these waveguide lasers with commercial systems further characterisation will be required with a larger range of output coupling conditions. This could also be performed in a simulation of the system as is discussed further in Section 5.5.

A spectrum of the laser output was taken at full pump power a 300 mm monochromator (Gilden Photonics) and is displayed in Figure 5.8.

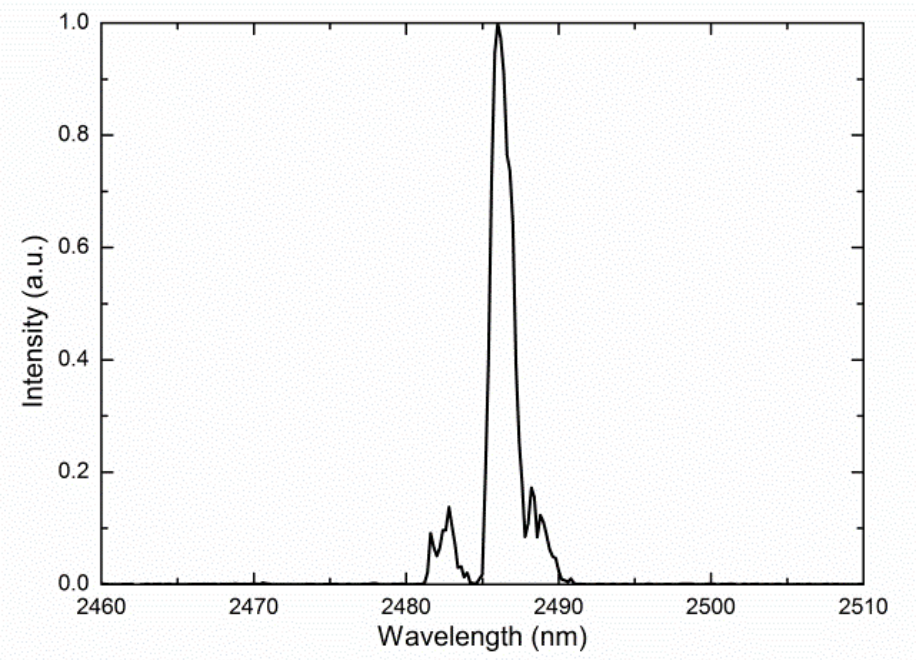

Figure 5.8. Laser output spectrum taken with 300 mm monochromator showing peak laser emission at 2486 nm with a FWHM line-width of 2 nm.

It can be seen in Figure 5.7 that for pump powers above threshold but less than 600 mW the gradient of the graph is not constant. This is the result of the cavity alignment being performed at high powers with the sample already under thermal load due to incident pump. The cavity is therefore not optimally aligned when the sample is cool. As the sample heats with increasing pump power the thermal expansion of the gain medium allows the cavity to return to the optimised alignment. Consequently, a low power alignment process was required for laser threshold measurements, this is presented in the next section.

5.3.2 Laser threshold measurements and Findlay-Clay analysis

Findlay-Clay analysis [117], offers a method of determining laser cavity losses through analysis of laser threshold powers at different values of output coupling. The analysis relies on laser threshold occurring when gain for one cavity round trip exactly balances cavity losses for one round trip. This can be expressed by Equation 5.1:

$$2g_T l = 2\alpha l - \ln(R_1 R_2) \qquad \textit{Equation 5.1}$$

where g_T is the gain at threshold, α is the cavity loss per unit length, R_1 and R_2 are the reflectivity values of the cavity mirrors and l is the cavity length. As the pump input mirror on our cavity is highly reflecting we can assume $R_1 = 1$. Since for an unsaturated gain medium the gain is directly proportional to the pump power we can rearrange Equation 5.1 into:

$$P_T = \beta(L - \ln R_{OC}) \qquad \textit{Equation 5.2}$$

where P_T is the pump power at threshold, β is a constant for the system, R_{OC} is the output coupler reflectivity and L is the cavity round trip loss, equal to $2\alpha l$. This allows for the round trip loss of the cavity to be experimentally determined based on measurements of laser threshold with different, known, output couplers by plotting laser threshold against $\ln(R_{OC})$.

To perform the threshold measurements the cavities were realigned with the pump beam chopped at 25% duty cycle. This allowed threshold to be reached at an effectively lower average power and therefore reduced thermal load. The laser threshold values are plotted against $\ln(R_{OC})$ with errors in the x-axis derived from the manufacturer quoted error in the output coupler reflectivity. The resultant Findlay-Clay analysis with a least squares linear fit to the data is displayed in Figure 5.9.

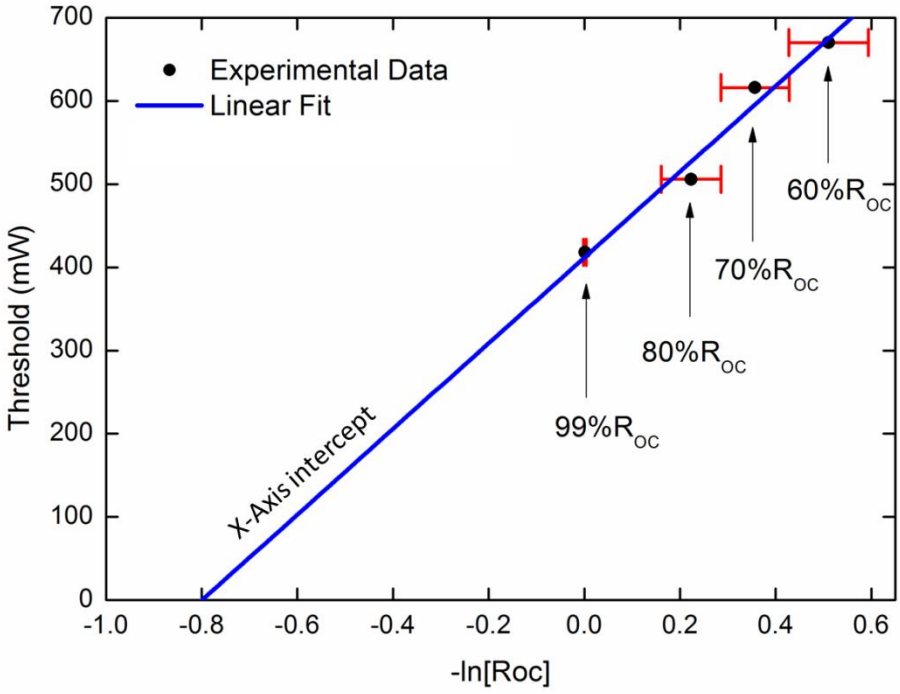

Figure 5.9. Findlay-Clay analysis plot displaying a round trip cavity loss of 0.8 dB. The error bars assigned to x-axis values are calculated from the manufacturer quoted errors in the output coupler reflectivity.

Round trip losses of 0.8 ± 0.1 dB were inferred from x-axis intercept of the least squares fit to the experimental data. As the waveguide measured 6 mm in length this corresponded to a waveguide propagation loss of 0.7 ± 0.1 dB·cm^{-1}. This is substantially lower than the value obtained for the double clad waveguides, 3.5 dB·cm^{-1}, accounting for the significant increase in laser performance.

5.3.3 M^2 measurement of beam quality

The M^2 measurement of beam quality is an industry standard held by the International Standardization Organization, ISO 11146 [146]. The ISO stipulates the requirements for the measurement and determining of the M^2 value for a laser beam. This requires the measurement of at least 10 beam widths inside and outwith the Rayleigh range of the subject beam. It is required that approximately half of the measurements should be within the Rayleigh range of the beam and approximately half beyond 2 Rayleigh lengths from the beam waist. Using this data the beam divergence angles, beam

propagation ratios and beam widths along the propagation axis are calculated through the fitting of a hyperbolic function specified in ISO 11146-3 [147]. For the work reported here, all beam profiles were measured using images a mid-infrared camera (FLIR SC7000).

The beam profile images are used to calculate the 1st order and 2nd order moments of the beam intensity distributions. The integrations required to determine these moments are performed on a subset of the data so as to prevent noise from overly affecting the integrals. The size and position of the integral window is determined by an iterative method stipulated by the ISO standard 11146-1. The experimental data with the associated hyperbolic function fit is displayed in Figure 5.10.

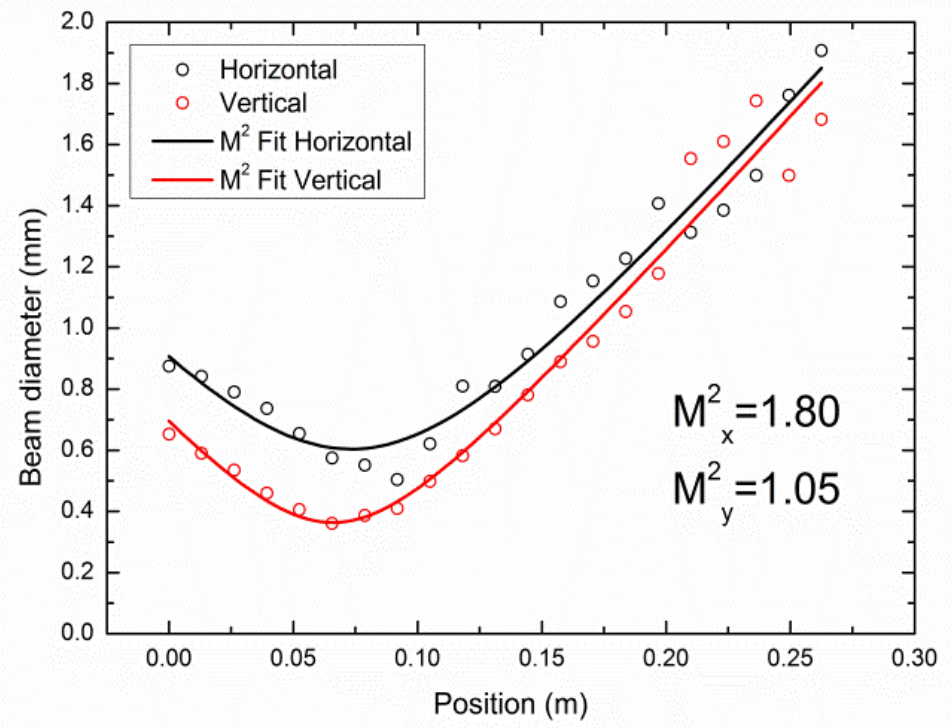

Figure 5.10. M^2 measurement data points and hyperbolic function fitted (solid line) for the perpendicular to the inscription laser propagation direction (black, labelled horizontal) and parallel to the inscription laser propagation direction (red, labelled vertical). The hyperbolic functions correspond to an M^2 value of 1.80 for the horizontal axis and 1.05 for the vertical axis.

The hyperbolic functions obtained from the data correspond to M^2 values of 1.05 in the vertical axis and 1.80 in the horizontal axis. This high beam quality corresponds to near diffraction limited performance, most especially in the vertical axis with an M^2 of 1.05

which is comparable even to fibre laser products [148]. An asymmetry in the M^2 value for each axis was expected due to the asymmetric nature of the waveguide supported modes, see Figure 4.18.

5.4. External cavity tuneble Cr^{2+}: ZnSe laser

5.4.1 External cavity design

An external cavity waveguide laser is a laser featuring a section of the cavity where light is guided by a waveguide structure and a section where the light is not confined propagates in a homogenous media. These devices aim to exploit advantages of both waveguide and bulk laser systems. Examples include external cavity diode lasers (ECDL) and high brightness multi-mode planar waveguide lasers [149]. The ECDLs make use of the high gain properties of a guided mode gain element and the simple, adjustable, wavelength selectivity of a diffraction grating or prism. Coupling between the guided mode and free space sections can be achieved with a lens or curved mirror. The two main configurations used to achieve this are known as the Littrow configuration and the Littman-Metcalf configuration, shown in Figure 5.11.

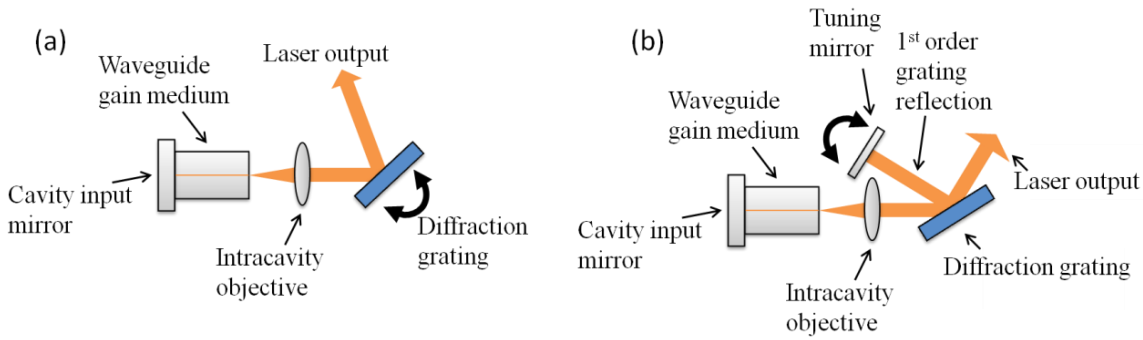

Figure 5.11. Schematic diagrams of (a) Littrow configuration and (b) Littman-Metcalf configuration for external cavity lasers.

The Littrow configuration is the simpler of the two, using the diffraction grating as a cavity end mirror to provide the feedback for the laser cavity. The first diffraction order is aligned so as to couple back into the waveguide and the laser output is taken from the zero-order. Rotation of the diffraction grating allows a chosen wavelength within the

material gain bandwidth to be reflected back to the waveguide providing laser output at that selected wavelength. As the grating is rotated the laser output direction also changes by an angle twice that of the grating rotation. This is problematic if large rotations are required to tune across the gain bandwidth as is the case for the large emission bandwidths in Cr^{2+}: ZnSe of approximately 1.3 µm.

The Littman-Metcalf configuration overcomes this problem with the use of an additional cavity mirror, see Figure 5.11(b). In this configuration the additional mirror is adjusted to control the feedback wavelength while the diffraction grating remains static. As the grating does not undergo any rotation, the output beam, again taken from the zero-order, remains static. However, this configuration has the drawback that the zero-order diffraction of the reflected beam from the tuning mirror is lost, resulting in a loss of efficiency in comparison to the Littrow configuration.

Despite the lower efficiency, the Littman-Metcalf configuration was chosen for the assembly of a tuneable Cr^{2+}: ZnSe laser cavity due to the significant benefit of a static beam output for laser characterisation.

5.4.2 Tuneable laser cavity assembly

A tuneable laser cavity was constructed using the 80 µm circular waveguide characterised in Section 5.2. The waveguide had been shown to support guiding at within the Cr^{2+}: ZnSe gain bandwidth with near 2-D Gaussian distribution modes observed at both 1928 and 2300 nm, see Figure 4.18. The waveguide has also demonstrated laser operation with 26% optical to optical efficiency and so was seen as a good candidate for use in as a tuneable waveguide laser. A Littman-Metcalf cavity was constructed using a 600 lines·mm^{-1}, 1600 nm blaze grating (GR13-0616) and a 2-inch silver tuning mirror as per the arrangement displayed in Figure 5.12. The input dichroic mirror used for the fixed wavelength waveguide laser cavity described in Section 5.3 was AR coated for the 1928 nm pump wavelength and HR from 2050 – 2430 nm. However, to allow access to longer wavelengths a new dichroic input mirror was used with AR coating at the 1928 nm pump wavelength and HR over 2400 – 3100 nm.

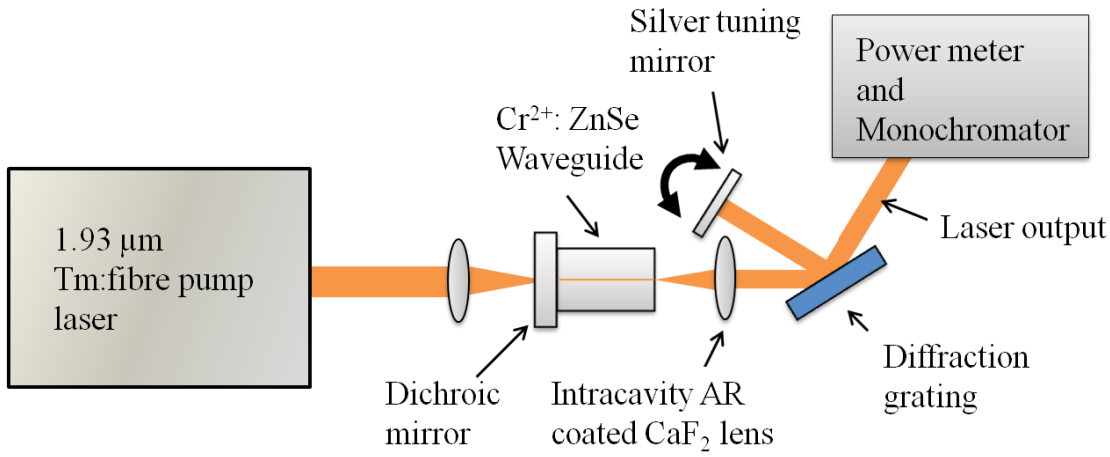

Figure 5.12. Schematic of Cr^{2+}: ZnSe tuneable laser cavity in the Littman-Metcalf configuration.

The Cr^{2+}: ZnSe crystal was uncoated so it was expected that the Fresnel reflections from the waveguide output facet would cause laser threshold to be reached without feedback from the grating. Threshold for the waveguide laser was previously reached at 670 mW pump without an output coupler. It was therefore expected that laser operation close to the gain peak from the Fresnel reflections would occur if the laser was tuned to regions of too low gain, far from the gain peak.

5.4.3 Tuneable laser performance

The laser cavity was pumped with the 1928 nm Tm^{3+}: fibre laser used for the fixed wavelength waveguide laser. Incremental rotation of the tuning mirror allowed the laser output power and wavelength to be recorded for a range of wavelengths. Figure 5.13 shows the laser output power measured against wavelength and the reflectivity of the input dichroic mirror. The data for the mirror reflectivity is taken from the manufacturer (Layertec) quoted specifications and has maximum 5% error. This data is also overlaid with the normalised emission cross-section of Cr^{2+}: ZnSe.

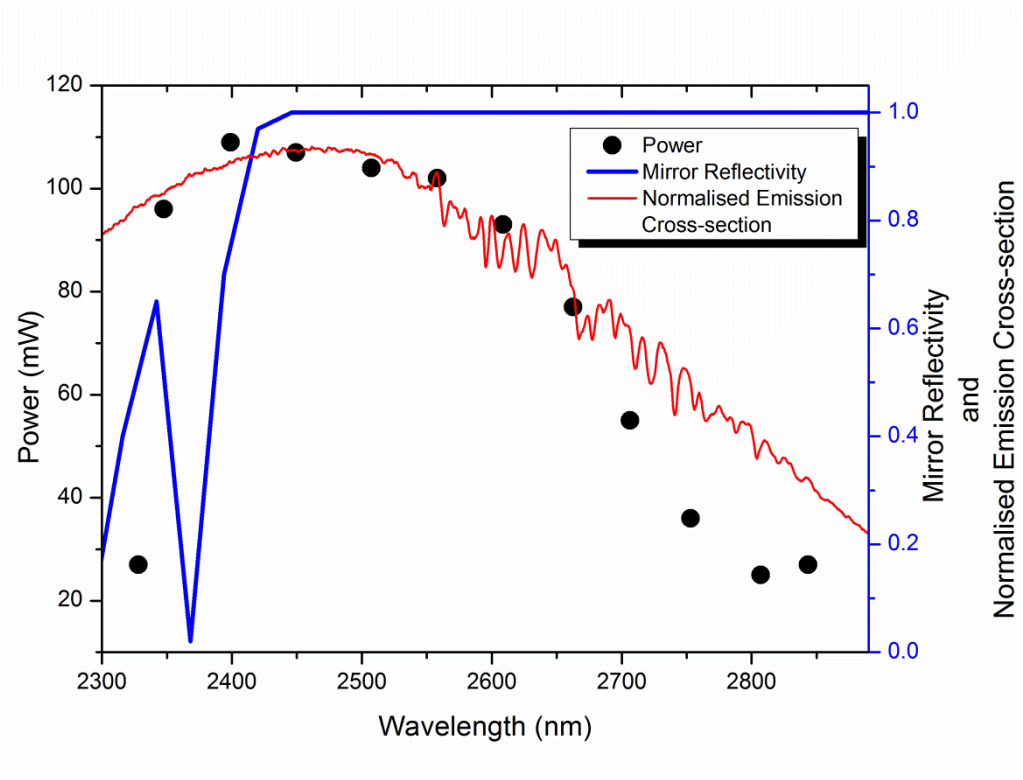

Figure 5.13. Cr^{2+}: ZnSe tuneable laser performance. Data points and left axis show measured power at specific wavelengths. Blue curve and right axis shows reflectivity of pump input mirror.Red curve and right axis show normalised emission cross-section of Cr^{2+}: ZnSe.

The maximum tuning range achieved was 510 nm from 2330 to 2840 nm with a maximum output power of 110 mW at 2399 nm and over 25 mW across the entire range. It is important to note that the short wavelength is likely limited by the reflectivity of the cavity mirror which has a cut-off at 2400 nm whereas the long wavelength end decreases in line with the emission cross-section, see Figure 5.13. It can also be seen that the output power at either limit of the tuning range does not tail off to lower powers than 25 mW. This was due to the Fresnel reflections causing laser operation at 2486 nm, as for the fixed wavelength laser, without dependence on the diffraction grating feedback. This was an expected problem as discussed in subsection 5.4.2 and could be addressed through the application of a broadband AR coating on the sample end facet to reduce the Fresnel reflections. The line-width of the tuneable laser output was measured at each wavelength using a 300 mm monochromator. The laser exhibited a FWHM line width of between 0.6 and 1.0 nm across the entire tuning range with the minimum line-width of 0.6 nm obtained across the range from 2550-2650 nm.

Figure 5.14 displays the recorded spectral data for output at 2600 nm. This measurement is at the resolution limit of the monochromator so a higher resolution instrument is required to determine the actual line-width of the tuneable laser. Although not performed this could easily be achieved by the use of a longer monochromator.

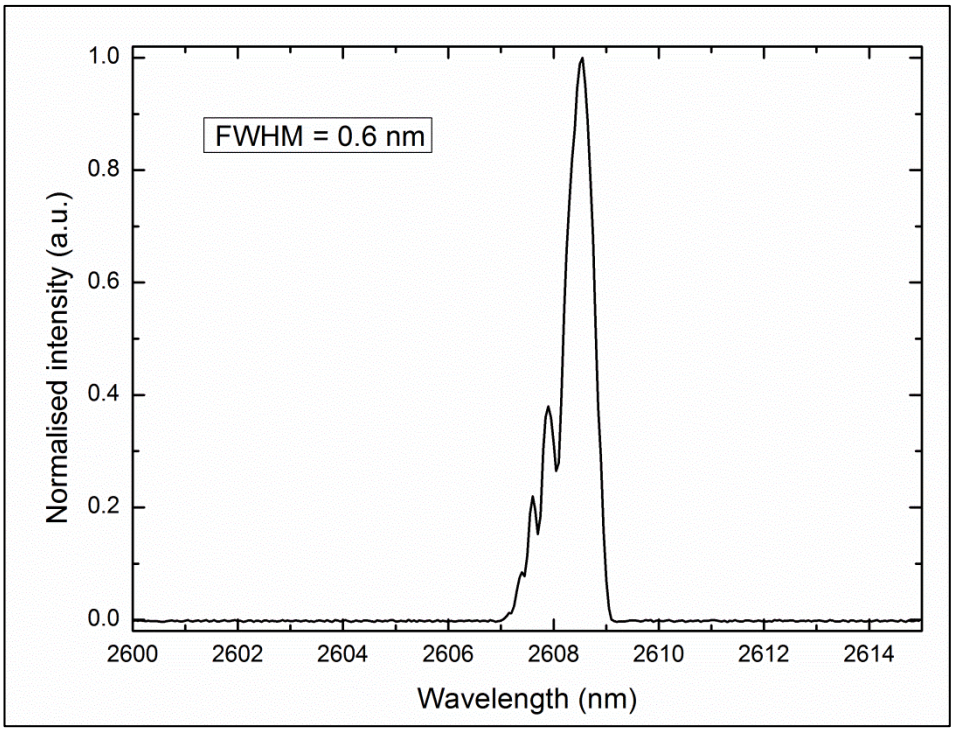

Figure 5.14 Output spectrum of tuneable Cr^{2+}: ZnSe waveguide laser operating at 2608 nm with a FWHM line-width of 0.6 nm.

5.5 Modelling laser efficiency and waveguide cavity losses

It is important to consider the propagation losses of the waveguides used in laser cavities and the limitations this might impose on device performance. The high propagation losses of 3.5 $dB \cdot cm^{-1}$ demonstrated by the rectangular cross-section waveguide (see Section 4.3) will have been a key factor in the limited laser slope efficiency of 2.5% demonstrated by this waveguide structure. A substantial improvement was achieved using the circular cross-section waveguides (see Section 5.3). These waveguides exhibited propagation losses of only 0.7 $dB \cdot cm^{-1}$ and demonstrated laser slope efficiencies as high as 45%. A useful study would be to model the maximum theoretical output power and efficiency of the waveguide laser

cavities for various propagation loss values. This could be achieved through numerically solving an adaptation of the theoretical model developed for Cr^{2+}: ZnSe systems by Berry *et al.* [15]. The model would require the addition of waveguide propagation losses and an adapted pump irradiance distribution to suit waveguide geometry.

As the propagation losses of the waveguides have such a significant impact on the performance of any constructed waveguide laser it could be beneficial to develop a model to aid waveguide design. The radiation losses of a particular waveguide could be modelled using the beam propagation method [150] however this would require a refractive index profile of the ULI waveguides to be known. Such a model would also not account for scattering losses in the waveguide structure but could at least provide information on the expected signal radiation from the waveguide for a given cross-sectional design.

5.6 Conclusions

This chapter has detailed the construction and performance of the first Cr^{2+}: ZnSe channel waveguide lasers. Initial operation of a double depressed cladding structure was demonstrated in a simple, passively aligned cavity. This was constructed by butt-coupling a dichroic input mirror and output coupler to opposite facets of the waveguide. Laser operation was achieved at 2573 nm with a FWHM line-width of 2 nm and the system achieved a pump limited maximum output power of 18.5 mW with a slope efficiency of 2.5% for an incident pump power of 1.2 W. This corresponds to an optical efficiency of 1.6%. The low efficiency of the device was attributed to high waveguide propagation losses of 3.5 $dB \cdot cm^{-1}$, however the demonstration of laser operation provides confirmation of the technology's viability. This initial report of a Cr^{2+}: ZnSe channel waveguide laser has been published in Applied Physics Letters journal [151].

Significant improvements in Cr^{2+}: ZnSe waveguide laser performance were achieved through the use of a circular cross-section depressed cladding waveguide design. An actively aligned cavity was implemented by placing the mirrors in optomechanics allowing for pitch, yaw and positional alignment. This laser emitted at 2486 nm with a FWHM line-width of 2 nm, and a maximum output power of 285 mW for 1090 mW of

pump. The slope efficiency of 45% and a total optical to optical efficiency of 26%. Laser operation with a range of output couplers of 60%, 80%, 70% and 99% allowed a Findlay-Clay analysis of the cavity losses which provided a value of 0.7±0.1 $dB \cdot cm^{-1}$ for the waveguide propagation losses. This was significantly lower loss than the 3.5 $dB \cdot cm^{-1}$ demonstrated for the double depressed cladding structures, explaining the substantial increase in laser performance. The M^2 beam quality of the laser was measured to ISO standards and was determined to be 1.80 in the horizontal axis and 1.05 in vertical axis.

Having demonstrated guiding at wavelengths of 1928 and 2300 nm and laser operation with optical to optical efficiencies of 26%, the circular depressed cladding structures were used to construct a tuneable external laser cavity. The cavity was constructed in the Littman-Metcalf configuration and provided tuneable output over 510 nm, from 2330 – 2840 nm. Beyond this range Fresnel reflections from the output facet dominated and the laser emitted at 2486 nm. The maximum power achieved for this laser was 110 mW at 2400 nm and >25 mW was produced across the entire tuning range. FWHM line-widths of between 0.6 and 1.0 nm were measured across the entire tuning range, all of which were narrower than that achieved with the fixed wavelength lasers due to the increased wavelength selectivity of the diffraction grating. Further improvement in both output power and tuning range is expected through AR coating of the waveguide output facet to reduce Fresnel reflections.

Chapter 6 – Conclusions and future work

6.1 Conclusions

The work reported in this thesis has focused on the development of mid-infrared waveguide laser sources in Cr^{2+}: ZnSe using ultrafast laser inscription to fabricate the required waveguide structures. Chapter 3 presents work on the challenges of applying ULI to ZnSe substrates and waveguide fabrication. Chapter 4 details the fabrication and characterisation of mid-infrared waveguides in ZnSe and Cr^{2+}: ZnSe. Finally, chapter 5 presents the demonstration CW and widely tuneable mid-infrared laser sources in Cr^{2+}: ZnSe. The following provides a summary of the work presented in each chapter.

Chapter 3 presents the first channel waveguides in ZnSe fabricated by ultrafast laser inscription. The challenge of self-focusing in the ULI process was highlighted for highly nonlinear substrates. This detrimental self-focusing in the inscription process was overcome through the investigation of inscription at picoseconds scale pulse durations avoiding the high peak powers produced by femtosecond pulses. Through this technique a positive refractive index change was achieved in ZnSe for the first time using ULI, allowing a study into the fabrication of ULI waveguides in ZnSe Characterisation of the structures was performed at 1550 nm demonstrating waveguide propagation losses as low as 1.1 $dB \cdot cm^{-1}$, with near 2-D Gaussian mode distributions.

These results offer ZnSe waveguide geometry with losses at 1550 nm comparable to that achieved in ZnSe optical fibres (1 $dB \cdot cm^{-1}$) demonstrated by Sparks *et al.* [18]. A key difference between the type I ULI waveguides and the fibres is the modality of the guided signal. The ZnSe fibres are multi-mode at 1550 nm whereas single-mode guiding is reported for the devices described in this thesis and therefore provide a higher spatial distribution beam quality. Although the type I waveguides do not offer guiding in the mid-infrared the low propagation losses at 1550 nm combined with the high optical nonlinearities of ZnSe make them well suited to photonic applications such as optical modulators and spectral broadening. The extension of ULI inscription

technology to single crystal ZnSe would also allow the high electro-optic and second order nonlinear coefficients of the material to be exploited for integrated optoelectronic devices.

Chapter 4 presents the first mid-infrared channel waveguides fabricated in ZnSe using ULI and the first channel waveguide in Cr^{2+}: ZnSe. Inscription parameter investigations at high pulse energies > 200 nJ yielded a negative refractive index change in a ZnSe substrate. The ability to reduce the refractive index of the ZnSe substrate in a localised volume was utilised to fabricate the cladding regions of waveguides structures, forming depressed cladding waveguide structures. Mid-infrared waveguides in ZnSe were demonstrated with propagation losses as low as 1.9 $dB \cdot cm^{-1}$ at 3390 nm. These structures were recreated in Cr^{2+}: ZnSe highlighting a discrepancy in the required pulse energy for successful material modification. Cr^{2+}: ZnSe was found to require over 50% increases in pulse energy to produce comparable material modification. The development of successful inscription parameters for Cr^{2+}: ZnSe allowed the fabrication of mid-infrared waveguides in the doped substrate. A novel ULI cladding structure employing an inner and outer cladding region was demonstrated to produce single-mode waveguides at 1928 and 3390 nm with passive losses at 3390 nm measured to be 3.5 $dB \cdot cm^{-1}$. These wavelengths represent the extreme limits of the Cr^{2+}: ZnSe gain bandwidth indicating the structure's suitability to application in a waveguide laser cavity.

The high losses of 3.5 $dB \cdot cm^{-1}$ however, are a limiting factor for the utilisation of these waveguide structures in laser cavities as the efficiency of any subsequent laser device will be reduced by the intracavity loss contributed by the waveguide losses. In order for the double depressed cladding design to be appropriate for use in a laser product the propagation losses of the structures must be reduced. This could be achieved through further investigation into the inscription parameters and technique with the aim of reducing micro-cracking in the structure and improving homogeneity of the modified region. An inscription method other than multiscan may be required to provide increased homogeneity in the individual modification blocks which are currently subject to optical damage at overlapping inscription 'scans' in the multiscan process (Figure 4.10).

In addition to the double cladding region waveguide, a circular cross-section depressed cladding waveguide was fabricated in Cr^{2+}: ZnSe. Cross-sectional diameters of 80-160 µm were inscribed with near 2-D Gaussian modes demonstrated at 1928 and 2300 nm, representative of pump and signal wavelengths for Cr^{2+}: ZnSe laser sources. Propagation losses in these structures could not be measured directly but were later inferred through Findlay-Clay analysis detailed in Chapter 5.

The range of waveguide cross-sectional areas possible with these structures compared to the double depressed cladding structures presents the possibility for single-mode or multi-mode structures. Where single-mode structures offer the small mode field diameters and high irradiances suitable for low threshold laser cavities, larger cross-section multi-mode structures are capable withstanding of higher pump input powers. It is important to consider the balance between the maximum pump irradiance on the waveguide facet and the amount of gain possible within the irradiated waveguide core and a simulation of the system would be beneficial to aid design of the optimum waveguide cavity.

Chapter 5 presents the first Cr^{2+}: ZnSe channel waveguide laser sources through the construction of waveguide laser cavities employing the waveguides developed in Cr^{2+}: ZnSe in Chapter 4. The cavities were constructed with an input dichroic mirror and output coupler positioned at either end facet of the waveguide. The first cavity, utilising the double cladding region waveguide was pumped at 1928 nm with a Tm^{3+}: fibre laser and demonstrated laser operation at 2573 nm with a FWHM line-width of 2 nm. A maximum output power of 18.5 mW CW for a pump power of 1210 mW was achieved using an 80% reflective output coupler with a laser slope efficiency of 2.5%. The low efficiency of the laser was attributed to the high (3.5 $dB \cdot cm^{-1}$) propagation losses of the waveguide.

A substantial improvement in laser performance was reported through the use of the circular cross-section waveguides, also reported in Chapter 4. Pumping with 1928 nm, laser output was observed at 2486 nm with a FWHM line-width of 2 nm and a maximum CW output power of 285 mW for 1090 mW of pump power. This corresponds to a slope efficiency of 45% and a high optical efficiency of 26%. Laser operation with a 60, 70, 80 and 99% reflectivity output coupler provided the data for a Findlay-Clay analysis of the cavity losses which yielded a maximum propagation loss

for the waveguide of 0.7 $dB \cdot cm^{-1}$. Finally, an M^2 beam quality measurement was performed to ISO standards and M^2 values of 1.80 and 1.05 were obtained for the horizontal and vertical axis respectively demonstrating near diffraction limited performance in the vertical axis.

Current commercial Cr^{2+}: ZnSe laser sources offer optical to optical efficiencies of up to 70% [16] which far exceeds the 26% efficiency achieved by the Cr^{2+}: ZnSe waveguide laser. However, the compact and robust nature of these waveguide sources places them in competition with QCL sources for applications outside of the laboratory. QCL products typically operate at room temperature wall plug efficiencies of approximately 10% [4] making the 26% optical to optical efficiency of the Cr^{2+}: ZnSe viable for product development. Moreover, tuneable waveguide laser products exploiting the wide (2 – 3.3 µm) gain bandwidth of Cr^{2+}: ZnSe is an attractive prospect for flexible spectroscopy technology.

The successful development of a widely tuneable Cr^{2+}: ZnSe waveguide laser was presented utilising ULI fabricated waveguides. The circular cross-section waveguides were constructed into an external cavity Littman-Metcalf configuration which demonstrated a maximum tuning range of 510 nm from 2330 – 2840 nm. A maximum CW output power of 110 mW was achieved at 2399 nm with over 25 mW of power available across the entire tuning range. FWHM line-widths of 0.6 – 1.0 nm were obtained over the wavelength range with a minimum FWHM line-width of 0.6 nm demonstrated at 2608 nm. The short wavelength limit of the tuning range was limited by the reflectivity bandwidth of the cavity input dichroic mirror which had an HR cut-off at 2400 nm. Additionally, the output facet of the waveguide was uncoated, providing 18% Fresnel reflections which also limited both the short and long wavelength range of the laser output. Therefore, AR coating of the waveguide facet and a broad bandwidth mirror for the 2-3.5 µm region is expected to significantly improve the performance of the tuneable laser.

The tuneable wavelength range offered by Cr^{2+}: ZnSe combined with the high average output powers > 100 mW provides a source for the molecular fingerprint region across 2 – 3 µm. The tuneability range of 510 nm achieved by the Cr^{2+}: ZnSe waveguide laser is already in excess of what is available from QCL technology with typical QCLs providing < 100 nm and < 100 mW tuneability in the region of 2 – 3 µm [152]. With the

potential improvements brought from optical coating of the waveguide facets the external cavity waveguide systems will be attractive products for the 2 – 3 μm wavelength range.

6.2 Future work

6.2.1 High power operation of Cr^{2+}: ZnSe waveguide laser

The successful demonstration of a Cr^{2+}: ZnSe waveguide laser with high optical efficiency of 26% opens the door to high power operation of these devices and a study into the problem of thermal lensing when operating in a waveguide geometry. As discussed in Chapter 4, thermal lensing in Cr^{2+}: ZnSe has long been a challenge to power scaling of these sources. Thermal lensing in the gain medium occurs at high irradiances causing cavity instability which has so far limited the maximum achieved output power to 14 W for Cr^{2+}: ZnSe. Waveguide geometry has been shown to offer protection from this detrimental effect with guided laser modes remaining unperturbed by the distortions in refractive index caused by thermal lensing [111]. Access to a high power pump source will be possible through a current collaboration allowing experimental evaluation of this property in the Cr^{2+}: ZnSe waveguides and potentially provide the means for increasing the record output power for a Cr^{2+}: ZnSe laser.

6.2.2 Direct diode pumping for monolithic Cr^{2+}: ZnSe waveguide lasers

Direct diode pumping of laser sources brings with it the benefits of more compact systems and higher wall plug efficiencies due the absence of an addition pump laser system. Cr^{2+}: ZnSe systems are generally pumped by Er^{3+} or Tm^{3+}: fibre systems however InGaAsP laser diodes have also been demonstrated as an effective pump source. The Cr^{2+}: ZnSe laser presented in Section 5.3 could be easily adapted to form a monolithic laser source through the use of InGaAsP pump diodes and an optical coating applied directly the waveguide end facets.

6.2.3 Fe^{2+}: ZnSe waveguide laser sources

The mid-infrared waveguides developed in Chapter 4 already demonstrate guiding properties suitable for applications in Fe^{2+}: ZnSe. Both waveguide designs support guiding in the mid-infrared and tailoring of structure dimensions could allow waveguides to be developed in Fe^{2+}: ZnSe over the material absorption and emission regions which span 2.2 – 5.0 µm. Fe^{2+}: ZnSe does not offer CW emission at room temperature due to the short upper-state lifetime of 370 ns but pulsed operation has been demonstrated [11] and CW operation at cryogenic temperatures has also been reported [153, 154]. The emission bandwidth of 3.5 – 5.0 µm is complementary to Cr^{2+}: ZnSe technology for spectroscopy applications with coverage of the 2-5 µm molecular fingerprint region offered by just two sources. As few direct laser sources are available in the 3-5 µm, and QCL fabrication remains challenging at these wavelengths, Fe^{2+}: ZnSe offers an attractive prospect of tuneable pulsed 3.5 – 5.0 µm sources. As with the Cr^{2+}: ZnSe technology, waveguide sources in Fe^{2+}: ZnSe could offer a compact and environmentally stable solution to many spectroscopy applications.

6.2.4 Bragg structures in ZnSe substrates

The fabrication of Bragg defects within waveguide structures will be investigated. An acousto-optic modulator can be employed to modulate the inscription laser beam, allowing periodic structures to be written within the waveguide, Figure 6.1. As the most effective modification of ZnSe is a negative refractive index change, the inscribed Bragg defects could be engineered to have a refractive index higher than that of the cladding but lower than that of the core. This would allow for a Bragg structure while minimising waveguide losses due to a lack of refractive index contrast. Realisation of this technology would open the door to integrated photonic devices such as compact single longitudinal mode Cr^{2+}: ZnSe sources.

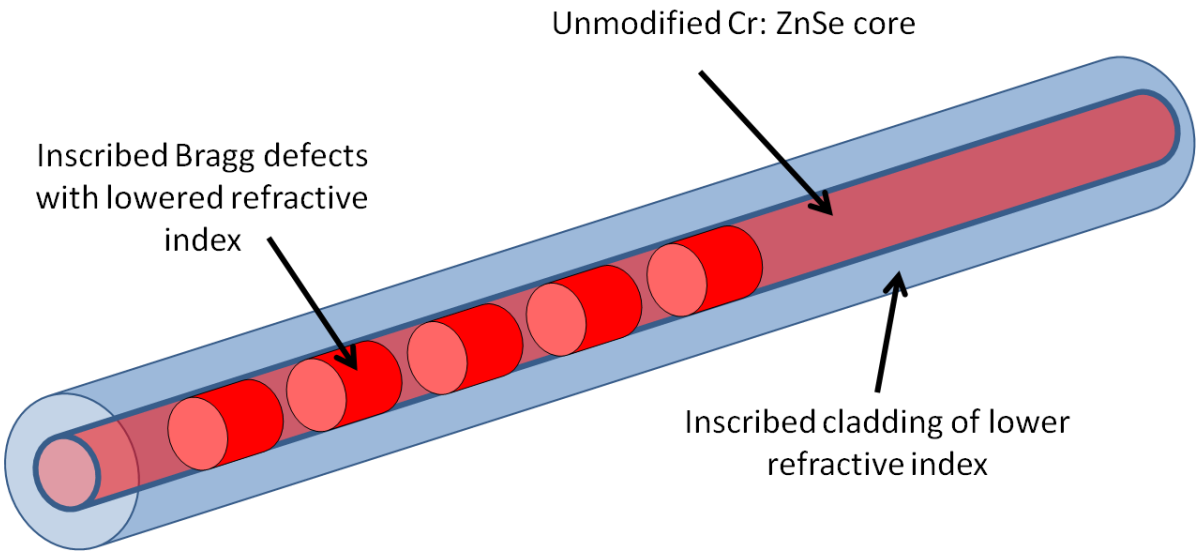

Figure 6.1. Example of Bragg defect written in a section of the Cr^{2+}: ZnSe circular cross-section waveguide.

The potential for ULI applications in transition metal doped II-VI semiconductors extends beyond just Cr^{2+}: ZnSe. As these laser sources are now reaching maturity the technology to fabricate integrated and monolithic sources exists in the highly flexible technique of ULI waveguide fabrication. The prospect of Bragg devices in active media brings with it the potential for narrow line-width, high power sources in the mid-infrared and the rapid prototyping capability of ULI is well placed to aid the production of a host of devices for a new generation of real world laser applications.

References

[1] T. H. Maiman, "Stimulated Optical Radiation in Ruby," *Nature,* **187**. 493-494, (1960).

[2] J. Faist, F. Capasso, D. L. Sivco, C. Sirtori, A. L. Hutchinson, and A. Y. Cho, "Quantum Cascade Laser," *Science,* **264**. 553-556, (1994).

[3] M. Beck, D. Hofstetter, T. Aellen, J. Faist, U. Oesterle, M. Ilegems, E. Gini, and H. Melchior, "Continuous Wave Operation of a Mid-Infrared Semiconductor Laser at Room Temperature," *Science,* **295**. 301-305, (2002).

[4] Y. Yao, A. J. Hoffman, and C. F. Gmachl, "Mid-infrared quantum cascade lasers," *Nat Photon,* **6**. 432-439, (2012).

[5] A. Hugi, R. Terazzi, Y. Bonetti, A. Wittmann, M. Fischer, M. Beck, J. Faist, and E. Gini, "External cavity quantum cascade laser tunable from 7.6 to 11.4 µm," *Applied Physics Letters,* **95**. 061103-3, (2009).

[6] D. M. Rines, P. F. Moulton, D. Welford, and G. A. Rines, "High-energy operation of a Co:MgF_2 laser," *Opt. Lett.,* **19**. 628-630, (1994).

[7] D. Welford and P. F. Moulton, "Room-temperature operation of a Co:MgF_2 laser," *Opt. Lett.,* **13**. 975-977, (1988).

[8] L. D. DeLoach, R. H. Page, G. D. Wilke, S. A. Payne, and W. F. Krupke, "Transition metal-doped zinc chalcogenides: spectroscopy and laser demonstration of a new class of gain media," *Quantum Electronics, IEEE Journal of,* **32**. 885-895, (1996).

[9] R. H. Page, K. I. Schaffers, L. D. DeLoach, G. D. Wilke, F. D. Patel, J. B. Tassano, Jr., S. A. Payne, W. F. Krupke, K. T. Chen, and A. Burger, "Cr^{2+}-doped zinc chalcogenides as efficient, widely tunable mid-infrared lasers," *Quantum Electronics, IEEE Journal of,* **33**. 609-619, (1997).

[10] U. Hömmerich, X. Wu, V. R. Davis, S. B. Trivedi, K. Grasza, R. J. Chen, and S. Kutcher, "Demonstration of room-temperature laser action at 2.5 µm from Cr^{2+}:$Cd_{0.85}Mn_{0.15}Te$," *Opt. Lett.,* **22**. 1180-1182, (1997).

[11] V. V. Fedorov, S. B. Mirov, A. Gallian, D. V. Badikov, M. P. Frolov, Y. V. Korostelin, V. I. Kozlovsky, A. I. Landman, Y. P. Podmar'kov, V. A. Akimov, and A. A. Voronov, "3.77-5.05 µm tunable solid-state lasers based on Fe^{2+}-doped ZnSe crystals operating at low and room temperatures," *Quantum Electronics, IEEE Journal of,* **42**. 907-917, (2006).

[12] I. T. Sorokina, E. Sorokin, S. Mirov, V. Fedorov, V. Badikov, V. Panyutin, and K. I. Schaffers, "Broadly tunable compact continuous-wave Cr^{2+}:ZnS laser," *Opt. Lett.,* **27**. 1040-1042, (2002).

[13] J. McKay, K. L. Schepler, and G. C. Catella, "Efficient grating-tuned mid-infrared Cr^{2+}:CdSe laser," *Opt. Lett.,* **24**. 1575-1577, (1999).

[14] U. Demirbas and A. Sennaroglu, "Intracavity-pumped Cr^{2+}:ZnSe laser with ultrabroad tuning range between 1880 and 3100 nm," *Opt. Lett.,* **31**. 2293-2295, (2006).

[15] P. A. Berry and K. L. Schepler, "High-power, widely-tunable Cr^{2+}:ZnSe master oscillator power amplifier systems," *Opt. Express,* **18**. 15062-15072, (2010).

[16] IPGPhotonics. (2013, 15th January). *Mid-infrared laser systems*. Available: http://www.ipgphotonics.com/Co2_ZnS.htm

[17] J. E. Williams, V. V. Fedorov, D. V. Martyshkin, I. S. Moskalev, R. P. Camata, and S. B. Mirov, "Mid-IR laser oscillation in Cr^{2+}:ZnSe planar waveguide," *Opt. Express,* **18**. 25999-26006, (2010).

[18] J. R. Sparks, R. He, N. Healy, M. Krishnamurthi, A. C. Peacock, P. J. A. Sazio, V. Gopalan, and J. V. Badding, "Zinc Selenide Optical Fibers," *Advanced Materials,* **23**. 1647-1651, (2011).

[19] J. Williams, J. Goldstein, D. Martyshkin, V. Fedorov, I. Moskalev, R. Camata, and S. Mirov, "Mid-IR Laser Oscillation In Cr:ZnSe Planar Waveguide Structures And In Cr:ZnSe/As_2S_3:As_2Se_3 Composite Materials," 2010, FThL3.

[20] K. C. Kao and G. A. Hockham, "Dielectric-fibre surface waveguides for optical frequencies," *Electrical Engineers, Proceedings of the Institution of,* **113**. 1151-1158, (1966).

[21] Corning. (2013, 20th January). *Optical Fiber*. Available: http://www.corning.com/opticalfiber/index.aspx

[22] NobelPrize.org. (2013, 25th February). *Nobel Prize in Physics 2009*. Available: http://www.nobelprize.org/nobel_prizes/physics/laureates/2009/

[23] P. K. Tien, "Light Waves in Thin Films and Integrated Optics," *Appl. Opt.,* **10**. 2395-2413, (1971).

[24] R. Shubert and J. H. Harris, "Optical Surface Waves on Thin Films and Their Application to Integrated Data Processors," *Microwave Theory and Techniques, IEEE Transactions on,* **16**. 1048-1054, (1968).

[25] R. G. Hunsperger, "Ch 4, Waveguide Fabrication Techniques," in *Integrated Optics: Theory and Technology*, ed: Springer, New York, (2009), Start Page.

[26] K. M. Davis, K. Miura, N. Sugimoto, and K. Hirao, "Writing waveguides in glass with a femtosecond laser," *Opt. Lett.,* **21**. 1729-1731, (1996).

[27] R. R. Thomson, S. Campbell, I. J. Blewett, A. K. Kar, and D. T. Reid, "Optical waveguide fabrication in z-cut lithium niobate ($LiNbO_3$) using femtosecond pulses in the low repetition rate regime," *Applied Physics Letters,* **88**. 111109-3, (2006).

[28] G. Li, X. Baoxi, and C. Tow Chong, "Microstructure in lithium niobate by use of focused femtosecond laser pulses," *Photonics Technology Letters, IEEE,* **16**. 1337-1339, (2004).

[29] N. D. Psaila, R. R. Thomson, H. T. Bookey, A. K. Kar, N. Chiodo, R. Osellame, G. Cerullo, G. Brown, A. Jha, and S. Shen, "Femtosecond laser inscription of optical waveguides in Bismuth ion doped glass," *Opt. Express,* **14**. 10452-10459, (2006).

[30] A. H. Nejadmalayeri and P. R. Herman, "Ultrafast laser waveguide writing: lithium niobate and the role of circular polarization and picosecond pulse width," *Opt. Lett.,* **31**. 2987-2989, (2006).

[31] H. T. Bookey, R. R. Thomson, N. D. Psaila, A. K. Kar, N. Chiodo, R. Osellame, and G. Cerullo, "Femtosecond Laser Inscription of Low Insertion Loss Waveguides in Z-Cut Lithium Niobate," *Photonics Technology Letters, IEEE,* **19**. 892-894, (2007).

[32] R. R. Thomson, H. T. Bookey, N. D. Psaila, A. Fender, S. Campbell, W. N. MacPherson, J. S. Barton, D. T. Reid, and A. K. Kar, "Ultrafast-laser inscription of a three dimensional fan-out device for multicore fiber coupling applications," *Opt. Express,* **15**. 11691-11697, (2007).

[33] C. B. Schaffer, A. Brodeur, and E. Mazur, "Laser-induced breakdown and damage in bulk transparent materials induced by tightly focused femtosecond laser pulses," *Measurement Science and Technology,* **12**. 1784, (2001).
[34] A. Couairon and A. Mysyrowicz, "Femtosecond filamentation in transparent media," *Physics Reports,* **441**. 47-189, (2007).
[35] G. Fibich and A. L. Gaeta, "Critical power for self-focusing in bulk media and in hollow waveguides," *Opt. Lett.,* **25**. 335-337, (2000).
[36] B. Amos, "Pinpoint of Light," ed: Science photo library.
[37] L. Keldysh, "Ionization in the field of a strong electromagnetic wave," *Soviet Physics JETP,* **20**, (1964).
[38] Y. Cheng, K. Sugioka, K. Midorikawa, M. Masuda, K. Toyoda, M. Kawachi, and K. Shihoyama, "Control of the cross-sectional shape of a hollow microchannel embedded in photostructurable glass by use of a femtosecond laser," *Opt. Lett.,* **28**. 55-57, (2003).
[39] M. Ams, G. Marshall, D. Spence, and M. Withford, "Slit beam shaping method for femtosecond laser direct-write fabrication of symmetric waveguides in bulk glasses," *Opt. Express,* **13**. 5676-5681, (2005).
[40] P. S. Salter, A. Jesacher, J. B. Spring, B. J. Metcalf, N. Thomas-Peter, R. D. Simmonds, N. K. Langford, I. A. Walmsley, and M. J. Booth, "Adaptive slit beam shaping for direct laser written waveguides," *Opt. Lett.,* **37**. 470-472, (2012).
[41] R. Osellame, S. Taccheo, M. Marangoni, R. Ramponi, P. Laporta, D. Polli, S. De Silvestri, and G. Cerullo, "Femtosecond writing of active optical waveguides with astigmatically shaped beams," *J. Opt. Soc. Am. B,* **20**. 1559-1567, (2003).
[42] R. R. Thomson, A. S. Bockelt, E. Ramsay, S. Beecher, A. H. Greenaway, A. K. Kar, and D. T. Reid, "Shaping ultrafast laser inscribed optical waveguides using a deformable mirror," *Opt. Express,* **16**. 12786-12793, (2008).
[43] R. D. Simmonds, P. S. Salter, A. Jesacher, and M. J. Booth, "Three dimensional laser microfabrication in diamond using a dual adaptive optics system," *Opt. Express,* **19**. 24122-24128, (2011).
[44] Y. Nasu, M. Kohtoku, and Y. Hibino, "Low-loss waveguides written with a femtosecond laser for flexible interconnection in a planar light-wave circuit," *Opt. Lett.,* **30**. 723-725, (2005).
[45] C. Hnatovsky, R. S. Taylor, E. Simova, V. R. Bhardwaj, D. M. Rayner, and P. B. Corkum, "Polarization-selective etching in femtosecond laser-assisted microfluidic channel fabrication in fused silica," *Opt. Lett.,* **30**. 1867-1869, (2005).
[46] J. R. Macdonald, P. A. Berry, K. L. Schelper, and A. Kar, "Directly Written Mid-Infrared Waveguides in Zinc Selenide," in *Advances in Optical Materials,* San Diego, USA, 2012, IF1A.3.
[47] J. R. Macdonald, R. R. Thomson, S. J. Beecher, N. D. Psaila, H. T. Bookey, and A. K. Kar, "Ultrafast laser inscription of near-infrared waveguides in polycrystalline ZnSe," *Opt. Lett.,* **35**. 4036-4038, (2010).
[48] S. M. Eaton, H. Zhang, M. L. Ng, J. Li, W.-J. Chen, S. Ho, and P. R. Herman, "Transition from thermal diffusion to heat accumulation in high repetition rate femtosecond laser writing of buried optical waveguides," *Opt. Express,* **16**. 9443-9458, (2008).

[49] S. Eaton, H. Zhang, P. Herman, F. Yoshino, L. Shah, J. Bovatsek, and A. Arai, "Heat accumulation effects in femtosecond laser-written waveguides with variable repetition rate," *Opt. Express*, **13**. 4708-4716, (2005).

[50] S. Rajesh and Y. Bellouard, "Towards fast femtosecond laser micromachining of fused silica: The effect of deposited energy," *Opt. Express,* **18**. 21490-21497, (2010).

[51] W. Yang, P. G. Kazansky, and Y. P. Svirko, "Non-reciprocal ultrafast laser writing," *Nat Photon,* **2**. 99-104, (2008).

[52] J. Burghoff, C. Grebing, S. Nolte, and A. Tünnermann, "Waveguides in lithium niobate fabricated by focused ultrashort laser pulses," *Applied Surface Science*, **253**. 7899-7902, (2007).

[53] A. Rodenas, L. M. Maestro, M. O. Ramirez, G. A. Torchia, L. Roso, F. Chen, and D. Jaque, "Anisotropic lattice changes in femtosecond laser inscribed Nd^{3+}:MgO:$LiNbO_3$ optical waveguides," *Journal of Applied Physics*, **106**. 013110-6, (2009).

[54] R. Mary, S. J. Beecher, G. Brown, R. R. Thomson, D. Jaque, S. Ohara, and A. K. Kar, "Compact, highly efficient ytterbium doped bismuthate glass waveguide laser," *Opt. Lett.*, **37**. 1691-1693, (2012).

[55] D. G. Lancaster, S. Gross, H. Ebendorff-Heidepriem, K. Kuan, T. M. Monro, M. Ams, A. Fuerbach, and M. J. Withford, "Fifty percent internal slope efficiency femtosecond direct-written Tm^{3+}:ZBLAN waveguide laser," *Opt. Lett.*, **36**. 1587-1589, (2011).

[56] A. G. Okhrimchuk, A. V. Shestakov, I. Khrushchev, and J. Mitchell, "Depressed cladding, buried waveguide laser formed in a YAG:Nd^{3+} crystal by femtosecond laser writing," *Opt. Lett.*, **30**. 2248-2250, (2005).

[57] N. Bellini, K. C. Vishnubhatla, F. Bragheri, L. Ferrara, P. Minzioni, R. Ramponi, I. Cristiani, and R. Osellame, "Femtosecond laser fabricated monolithic chip for optical trapping and stretching of single cells," *Opt. Express*, **18**. 4679-4688, (2010).

[58] M. Kim, D. J. Hwang, H. Jeon, K. Hiromatsu, and C. P. Grigoropoulos, "Single cell detection using a glass-based optofluidic device fabricated by femtosecond laser pulses," *Lab on a Chip*, **9**. 311-318, (2009).

[59] Y. Bellouard, A. Said, M. Dugan, and P. Bado, "Fabrication of high-aspect ratio, micro-fluidic channels and tunnels using femtosecond laser pulses and chemical etching," *Opt. Express*, **12**. 2120-2129, (2004).

[60] D. Choudhury, W. T. Ramsay, R. Kiss, N. A. Willoughby, L. Paterson, and A. K. Kar, "A 3D mammalian cell separator biochip," *Lab on a Chip*, **12**. 948-953, (2012).

[61] H. Ogilvy, M. Withford, P. Dekker, and J. Piper, "High repetition rate, q-switched and intracavity frequency doubled Nd:YVO4 laser at 671nm," *Opt. Express*, **12**. 3543-3547, (2004).

[62] F. M. Bain, A. A. Lagatsky, R. R. Thomson, N. D. Psaila, N. V. Kuleshov, A. K. Kar, W. Sibbett, and C. T. A. Brown, "Ultrafast laser inscribed Yb:$KGd(WO_4)_2$ and Yb:$KY(WO_4)_2$ channel waveguide lasers," *Opt. Express*, **17**. 22417-22422, (2009).

[63] S. M. Eaton, C. A. Merchant, R. Iyer, A. J. Zilkie, A. S. Helmy, J. S. Aitchison, P. R. Herman, D. Kraemer, R. J. D. Miller, C. Hnatovsky, and R. S. Taylor, "Raman gain from waveguides inscribed in $KGd(WO_4)_2$ by high repetition rate femtosecond laser," *Applied Physics Letters*, **92**. 081105-3, (2008).

[64] H. Liu, Y. Jia, J. R. Vázquez de Aldana, D. Jaque, and F. Chen, "Femtosecond laser inscribed cladding waveguides in Nd:YAG ceramics: Fabrication, fluorescence imaging and laser performance," *Opt. Express*, **20**. 18620-18629, (2012).

[65] S. J. Beecher, R. R. Thomson, B. P. Pal, and A. K. Kar, "Single Stage Ultrafast Laser Inscription of a Side-Polished Fiber-Like Waveguide Sensor," *Sensors Journal, IEEE*, **12**. 1263-1266, (2012).

[66] M. Ams, P. Dekker, G. D. Marshall, and M. J. Withford, "Dual wavelength waveguide lasers fabricated using femtosecond laser inscription in Yb doped phosphate glass," in *Lasers and Electro-Optics Europe (CLEO EUROPE/EQEC), 2011 Conference on and 12th European Quantum Electronics Conference*, 2011, 1-1.

[67] V. Ta'eed, N. J. Baker, L. Fu, K. Finsterbusch, M. R. E. Lamont, D. J. Moss, H. C. Nguyen, B. J. Eggleton, D.-Y. Choi, S. Madden, and B. Luther-Davies, "Ultrafast all-optical chalcogenide glass photonic circuits," *Opt. Express*, **15**. 9205-9221, (2007).

[68] R. R. Thomson, T. A. Birks, S. G. Leon-Saval, A. K. Kar, and J. Bland-Hawthorn, "Ultrafast laser inscription of an integrated photonic lantern," *Opt. Express*, **19**. 5698-5705, (2011).

[69] Y. Ren, N. Dong, J. Macdonald, F. Chen, H. Zhang, and A. K. Kar, "Continuous wave channel waveguide lasers in Nd:$LuVO_4$ fabricated by direct femtosecond laser writing," *Opt. Express*, **20**. 1969-1974, (2012).

[70] A. Rodenas, A. Benayas, J. R. Macdonald, J. Zhang, D. Y. Tang, D. Jaque, and A. K. Kar, "Direct laser writing of near-IR step-index buried channel waveguides in rare earth doped YAG," *Opt. Lett.*, **36**. 3395-3397, (2011).

[71] J. E. McCarthy, H. T. Bookey, N. D. Psaila, R. R. Thomson, and A. K. Kar, "Mid-infrared spectral broadening in an ultrafast laser inscribed gallium lanthanum sulphide waveguide," *Opt. Express*, **20**. 1545-1551, (2012).

[72] Y. Ren, G. Brown, A. Ródenas, S. Beecher, F. Chen, and A. K. Kar, "Mid-infrared waveguide lasers in rare-earth-doped YAG," *Opt. Lett.*, **37**. 3339-3341, (2012).

[73] S. J. Beecher, R. R. Thomson, D. T. Reid, N. D. Psaila, M. Ebrahim-Zadeh, and A. K. Kar, "Strain field manipulation in ultrafast laser inscribed BiB_3O_6 optical waveguides for nonlinear applications," *Opt. Lett.*, **36**. 4548-4550, (2011).

[74] F. Dreisow, J. Thomas, J. Burghoff, A. Ancona, M. Heinrich, S. Nolte, and A. Tunnermann, "Efficient frequency doubling in fs-laser written waveguides in PPLN and BBO," in *SPIE 425 Photonics West/LASE*, 2008, paper 6879A-34.

[75] J. Thomas, M. Heinrich, J. Burghoff, S. Nolte, A. Ancona, and A. Tunnermann, "Femtosecond laser-written quasi-phase-matched waveguides in lithium niobate," *Applied Physics Letters*, **91**. 151108-3, (2007).

[76] S. Campbell, R. R. Thomson, D. P. Hand, A. K. Kar, D. T. Reid, C. Canalias, V. Pasiskevicius, and F. Laurell, "Frequency-doubling in femtosecond laser inscribed periodically-poled potassium titanyl phosphate waveguides," *Opt. Express*, **15**. 17146-17150, (2007).

[77] B. R. Jackson, P. J. A. Sazio, and J. V. Badding, "Single-Crystal Semiconductor Wires Integrated into Microstructured Optical Fibers," *Advanced Materials*, **20**. 1135-1140, (2008).

[78] P. J. A. Sazio, A. Amezcua-Correa, C. E. Finlayson, J. R. Hayes, T. J. Scheidemantel, N. F. Baril, B. R. Jackson, D.-J. Won, F. Zhang, E. R. Margine,

V. Gopalan, V. H. Crespi, and J. V. Badding, "Microstructured Optical Fibers as High-Pressure Microfluidic Reactors," *Science,* **311**. 1583-1586, (2006).

[79] A. H. Nejadmalayeri, P. R. Herman, J. Burghoff, M. Will, S. Nolte, and A. Tünnermann, "Inscription of optical waveguides in crystalline silicon by mid-infrared femtosecond laser pulses," *Opt. Lett.,* **30**. 964-966, (2005).

[80] H. P. Wagner, M. Kühnelt, W. Langbein, and J. M. Hvam, "Dispersion of the second-order nonlinear susceptibility in ZnTe, ZnSe, and ZnS," *Physical Review B,* **58**. 10494-10501, (1998).

[81] P. Berry, J. MacDonald, A. Kar, and K. Schepler, "Ultrafast Laser Inscription of Waveguide Structures in Cr^{2+}:ZnSe," in *Advances in Optical Materials*, Istanbul, Turkey, 2011, AIFB5.

[82] A. Okhrimchuk, V. Mezentsev, H. Schmitz, M. Dubov, and I. Bennion, "Cascaded nonlinear absorption of femtosecond laser pulses in dielectrics," *Laser Physics,* **19**. 1415-1422, (2009).

[83] R. DeSalvo, A. A. Said, D. J. Hagan, E. W. Van Stryland, and M. Sheik-Bahae, "Infrared to ultraviolet measurements of two-photon absorption and n_2 in wide bandgap solids," *Quantum Electronics, IEEE Journal of,* **32**. 1324-1333, (1996).

[84] D. Marcuse, "Loss Analysis of Single-Mode Fiber Splices," *Bell Syst. Tech. J.,* **56**. 703-718, (1977).

[85] C. Zhang, N. Dong, J. Yang, F. Chen, J. R. Vázquez de Aldana, and Q. Lu, "Channel waveguide lasers in Nd:GGG crystals fabricated by femtosecond laser inscription," *Opt. Express,* **19**. 12503-12508, (2011).

[86] I. T. Sorokina, "Cr^{2+}-doped II–VI materials for lasers and nonlinear optics," *Optical Materials,* **26**. 395-412, (2004).

[87] R. Regener and W. Sohler, "Loss in low-finesse Ti:$LiNbO_3$ optical waveguide resonators," *Applied Physics B: Lasers and Optics,* **36**. 143-147, (1985).

[88] T. Numai, "Ch. 5. Fundamentals of semiconductor lasers," in *Fundamentals of semiconductor lasers*, ed: Springer New York, (2004), Start Page.

[89] J. Ding, H. Jeon, T. Ishihara, M. Hagerott, A. V. Nurmikko, H. Luo, N. Samarth, and J. Furdyna, "Excitonic gain and laser emission in ZnSe-based quantum wells," *Physical Review Letters,* **69**. 1707-1710, (1992).

[90] H. Okuyama, T. Miyajima, Y. Morinaga, F. Hiei, M. Ozawa, and K. Akimoto, "ZnSe/ZnMgSSe blue laser diode," *Electronics Letters,* **28**. 1798-1799, (1992).

[91] C. Boney, Z. Yu, W. H. Rowland, W. C. Hughes, J. W. Cook, J. F. Schetzina, G. Cantwell, and W. C. Harsch, "II-VI blue/green laser diodes on ZnSe substrates," *Journal of Vacuum Science & Technology B: Microelectronics and Nanometer Structures,* **14**. 2259-2262, (1996).

[92] D. B. Carlin and Y. Tsunoda, "Diode lasers for mass market applications: optical recording and printing," *Proceedings of the IEEE,* **82**. 469-481, (1994).

[93] S. Nakamura, S. Pearton, and G. Fasol, *The Blue Laser Diode: The Complete Story*: Springer, (2000).

[94] E. Kato, H. Noguchi, M. Nagai, H. Okuyama, S. Kijima, and A. Ishibashi, "Significant progress in Il-VI blue-green laser diode lifetime," *Electronics Letters,* **34**. 282-284, (1998).

[95] S. Nakamura, T. Mukai, and M. Senoh, "Candela-class high-brightness InGaN/AlGaN double-heterostructure blue-light-emitting diodes," *Applied Physics Letters,* **64**. 1687-1689, (1994).

[96] M. Sheik-bahae, A. A. Said, and E. W. Van Stryland, "High-sensitivity, single-beam n_2 measurements," *Opt. Lett.,* **14**. 955-957, (1989).

[97] M. Sheik-Bahae, A. A. Said, T. H. Wei, D. J. Hagan, and E. W. Van Stryland, "Sensitive measurement of optical nonlinearities using a single beam," *Quantum Electronics, IEEE Journal of,* **26**. 760-769, (1990).
[98] T. D. Krauss and F. W. Wise, "Femtosecond measurement of nonlinear absorption and refraction in CdS, ZnSe, and ZnS," *Applied Physics Letters,* **65**. 1739-1741, (1994).
[99] M. Balu, J. Hales, D. Hagan, and E. Van Stryland, "Dispersion of nonlinear refraction and two-photon absorption using a white-light continuum Z-scan," *Opt. Express,* **13**. 3594-3599, (2005).
[100] B. Derkowska, B. Sahraoui, X. Nguyen Phu, and W. Bala, "Nonlinear optical properties of monocrystal ZnSe," in *Transparent Optical Networks, 1999. International Conference on*, 1999, 185-188.
[101] M. Sheik-Bahae, D. C. Hutchings, D. J. Hagan, and E. W. Van Stryland, "Dispersion of bound electron nonlinear refraction in solids," *Quantum Electronics, IEEE Journal of,* **27**. 1296-1309, (1991).
[102] E. W. Van Stryland, M. Sheik-Bahae, A. A. Said, and D. J. Hagan, "Characterization of nonlinear optical absorption and refraction," *Progress in Crystal Growth and Characterization of Materials,* **27**. 279-311, (1993).
[103] F. Trager, "Part B - Fabrication and properties of optical componants," in *Springer handbook of lasers and optics*, ed: Springer New York, (2007), Start Page.
[104] G. S. Kanner, M. L. Marable, N. B. Singh, A. Berghmans, D. Kahler, B. Wagner, A. Lin, M. M. Fejer, J. S. Harris, and K. L. Schepler, "Optical probes of orientation-patterned ZnSe quasi-phase-matched devices," *Optical Engineering,* **48**. 114201-114201, (2009).
[105] P. B. Corkum, P. P. Ho, R. R. Alfano, and J. T. Manassah, "Generation of infrared supercontinuum covering 3-14 μm in dielectrics and semiconductors," *Opt. Lett.,* **10**. 624-626, (1985).
[106] E. W. V. Stryland, Y. Y. Wu, D. J. Hagan, M. J. Soileau, and K. Mansour, "Optical limiting with semiconductors," *J. Opt. Soc. Am. B,* **5**. 1980-1988, (1988).
[107] T. Kanamori, Y. Terunuma, S. Takahashi, and T. Miyashita, "Chalcogenide glass fibers for mid-infrared transmission," *Lightwave Technology, Journal of,* **2**. 607-613, (1984).
[108] J. S. Sanghera, L. B. Shaw, L. E. Busse, V. Q. Nguyen, P. C. Pureza, B. C. Cole, B. B. Harrison, I. D. Aggarwal, R. Mossadegh, F. Kung, D. Talley, D. Roselle, and R. Miklos, "Development and Infrared Applications of Chalcogenide Glass Optical Fibers," *Fiber and Integrated Optics,* **19**. 251-274, (2000).
[109] T. J. Carrig, G. J. Wagner, W. J. Alford, and A. Zakel, "Chromium-doped chalcogenide lasers," *SPIE Proceedings,* **5460**, (2004).
[110] E. Sorokin, I. T. Sorokina, M. S. Mirov, V. V. Fedorov, I. S. Moskalev, and S. B. Mirov, "Ultrabroad Continuous-Wave Tuning of Ceramic Cr:ZnSe and Cr:ZnS Lasers," in *Advanced Solid-State Photonics*, San Diego, USA, 2010, AMC2.
[111] J. Nilsson and D. N. Payne, "High-Power Fiber Lasers," *Science,* **332**. 921-922, (2011).
[112] A. W. Snyder and J. Love, "Ch. 24, Leaky Modes," in *Optical Waveguide Theory*, ed: Springer, (1983), Start Page.

[113] J. Hu and C. R. Menyuk, "Understanding leaky modes: slab waveguide revisited," *Adv. Opt. Photon.*, **1**. 58-106, (2009).
[114] R. G. Hunsperger, "Ch. 6. Losses in Optical Waveguides," in *Integrated Optics*, ed: Springer New York, (2009), Start Page.
[115] U. Demirbas, A. Sennaroglu, and M. Somer, "Synthesis and characterization of diffusion-doped Cr^{2+}:ZnSe and Fe^{2+}:ZnSe," *Optical Materials,* **28**. 231-240, (2006).
[116] A. Okhrimchuk, V. Mezentsev, A. Shestakov, and I. Bennion, "Low loss depressed cladding waveguide inscribed in YAG:Nd single crystal by femtosecond laser pulses," *Opt. Express,* **20**. 3832-3843, (2012).
[117] D. Findlay and R. A. Clay, "The measurement of internal losses in 4-level lasers," *Physics Letters,* **20**. 277-278, (1966).
[118] J. N. Walpole, A. R. Calawa, T. C. Harman, and S. H. Groves, "Double-heterostructure PbSnTe lasers grown by molecular-beam epitaxy with cw operation up to 114 K," *Applied Physics Letters,* **28**. 552-554, (1976).
[119] D. Richter, A. Fried, B. P. Wert, J. G. Walega, and F. K. Tittel, "Development of a tunable mid-IR difference frequency laser source for highly sensitive airborne trace gas detection," *Applied Physics B,* **75**. 281-288, (2002).
[120] W. Koechner, "Ch. 10. Nonlinear Devices," in *Solid-State Laser Engineering*, ed: Springer, (2006), Start Page.
[121] P. A. Budni, L. A. Pomeranz, M. L. Lemons, C. A. Miller, J. R. Mosto, and E. P. Chicklis, "Efficient mid-infrared laser using 1.9-µm-pumped Ho:YAG and $ZnGeP_2$ optical parametric oscillators," *J. Opt. Soc. Am. B,* **17**. 723-728, (2000).
[122] T. Dahinten, U. Plodereder, A. Seilmeier, K. L. Vodopyanov, K. R. Allakhverdiev, and Z. A. Ibragimov, "Infrared pulses of 1 picosecond duration tunable between 4 µm and 18 µm," *Quantum Electronics, IEEE Journal of,* **29**. 2245-2250, (1993).
[123] Y. Bai, S. Slivken, S. R. Darvish, and M. Razeghi, "Room temperature continuous wave operation of quantum cascade lasers with 12.5% wall plug efficiency," *Applied Physics Letters,* **93**. 021103-3, (2008).
[124] P. Q. Liu, A. J. Hoffman, M. D. Escarra, K. J. Franz, J. B. Khurgin, Y. Dikmelik, X. Wang, J.-Y. Fan, and C. F. Gmachl, "Highly power-efficient quantum cascade lasers," *Nat Photon,* **4**. 95-98, (2010).
[125] A. Bismuto, M. Beck, and J. Faist, "High power Sb-free quantum cascade laser emitting at 3.3 µm above 350 K," *Applied Physics Letters,* **98**. 191104-3, (2011).
[126] R. M. Matthew, B. Yury, W. Gerard, L. Rafal, and K. T. Frank, "Recent advances of laser-spectroscopy-based techniques for applications in breath analysis," *Journal of Breath Research,* **1**. 014001, (2007).
[127] Q. Ren, V. Venugopalan, K. Schomacker, T. F. Deutsch, T. J. Flotte, C. A. Puliafito, and R. Birngruber, "Mid-Infrared laser ablation of the cornea: A comparative study," *Lasers in Surgery and Medicine,* **12**. 274-281, (1992).
[128] J. Reid, J. Shewchun, B. K. Garside, and E. A. Ballik, "High sensitivity pollution detection employing tunable diode lasers," *Appl. Opt.,* **17**. 300-307, (1978).
[129] R. Claps, F. V. Englich, D. P. Leleux, D. Richter, F. K. Tittel, and R. F. Curl, "Ammonia Detection by use of Near-Infrared Diode-Laser-Based Overtone Spectroscopy," *Appl. Opt.,* **40**. 4387-4394, (2001).

[130] R. Lewicki, G. Wysocki, A. A. Kosterev, and F. K. Tittel, "Carbon dioxide and ammonia detection using 2 μm diode laser based quartz-enhanced photoacoustic spectroscopy," *Applied Physics B,* **87**. 157-162, (2007).
[131] I. S. Moskalev, V. V. Fedorov, and S. B. Mirov, "Tunable, Single-Frequency, and Multi-Watt Continuous-Wave Cr^{2+}:ZnSe Lasers," *Opt. Express,* **16**. 4145-4153, (2008).
[132] S. B. Mirov, V. V. Fedorov, I. S. Moskalev, and D. V. Martyshkin, "Recent Progress in Transition-Metal-Doped II-VI Mid-IR Lasers," *Selected Topics in Quantum Electronics, IEEE Journal of,* **13**. 810-822, (2007).
[133] W. Koechner, "Ch. 2. Properties of Solid-state Laser Materials," in *Solid-State Laser Engineering*
ed, (2006), Start Page.
[134] G. Grebe, G. Roussos, and H. J. Schulz, "Cr^{2+} excitation levels in ZnSe and ZnS," *Journal of Physics C: Solid State Physics,* **9**. 4511, (1976).
[135] A. Fazzio, M. J. Caldas, and A. Zunger, "Many-electron multiplet effects in the spectra of 3d impurities in heteropolar semiconductors," *Physical Review B,* **30**. 3430-3455, (1984).
[136] B. Nygren, J. T. Vallin, and G. A. Slack, "Direct observation of the Jahn-Teller splitting in ZnSe: Cr^{2+}," *Solid State Communications,* **11**. 35-38, (1972).
[137] A. Sennaroglu, *Solid-State Lasers and Applications*: Taylor & Francis, (2010).
[138] E. Sorokin and I. T. Sorokina, "Tunable diode-pumped continuous-wave Cr^{2+}:ZnSe laser," *Applied Physics Letters,* **80**. 3289-3291, (2002).
[139] M. N. Cizmeciyan, H. Cankaya, A. Kurt, and A. Sennaroglu, "Operation of femtosecond Kerr-lens mode-locked Cr:ZnSe lasers with different dispersion compensation methods," *Applied Physics B,* **106**. 887-892, (2012).
[140] M. N. Cizmeciyan, H. Cankaya, A. Kurt, and A. Sennaroglu, "Kerr-lens mode-locked femtosecond Cr^{2+}:ZnSe laser at 2420 nm," *Opt. Lett.,* **34**. 3056-3058, (2009).
[141] P. Moulton and E. Slobodchikov, "1-GW-Peak-Power, Cr:ZnSe Laser," in *CLEO:2011 - Laser Applications to Photonic Applications,* Baltimore, USA, 2011, PDPA10.
[142] M. G. Littman and H. J. Metcalf, "Spectrally narrow pulsed dye laser without beam expander," *Appl. Opt.,* **17**. 2224-2227, (1978).
[143] M. Fleming and A. Mooradian, "Spectral characteristics of external-cavity controlled semiconductor lasers," *Quantum Electronics, IEEE Journal of,* **17**. 44-59, (1981).
[144] C. J. Hawthorn, K. P. Weber, and R. E. Scholten, "Littrow configuration tunable external cavity diode laser with fixed direction output beam," *Review of Scientific Instruments,* **72**. 4477-4479, (2001).
[145] Y. Ren, S. J. Beecher, G. Brown, A. Rodenas, F. Chen, and A. K. Kar, "Near-IR to Mid-IR Multimode Waveguides in Rare-Earth doped YAG by Ultrafast Laser Inscription," 2012, CTU1J.3.
[146] ISOStandardscatalogue. (2005, 13th January). *ISO 11146-1*. Available: http://www.iso.org/iso/home/store/catalogue_tc/catalogue_detail.htm?csnumber=33625
[147] ISOStandardscatalogue. (2004, 13th January). *ISO 11146-3*. Available: http://www.iso.org/iso/home/store/catalogue_tc/catalogue_detail.htm?csnumber=33627

[148] IPGPhotonics. (2013, 15th January). *2 micron products*. Available: http://www.ipgphotonics.com/products_2microns.htm
[149] S. P. Ng and J. I. Mackenzie, "High-brightness 946 nm Nd:YAG planar waveguide laser," in *Lasers and Electro-Optics Europe (CLEO EUROPE/EQEC), 2011 Conference on and 12th European Quantum Electronics Conference*, 2011, 1-1.
[150] J. VanRoey, J. van derDonk, and P. E. Lagasse, "Beam-propagation method: analysis and assessment," *J. Opt. Soc. Am.*, **71**. 803-810, (1981).
[151] J. R. Macdonald, S. J. Beecher, P. A. Berry, K. L. Schepler, and A. K. Kar, "Compact mid-infrared Cr:ZnSe channel waveguide laser," *Applied Physics Letters*, **102**. 161110-3, (2013).
[152] T. Kruczek, K. A. Fedorova, G. S. Sokolovskii, R. Teissier, A. N. Baranov, and E. U. Rafailov, "InAs/AlSb widely tunable external cavity quantum cascade laser around 3.2 μm," *Applied Physics Letters*, **102**. 011124-3, (2013).
[153] J. W. Evans, P. A. Berry, and K. L. Schepler, "840 mW continuous-wave Fe:ZnSe laser operating at 4140 nm," *Opt. Lett.*, **37**. 5021-5023, (2012).
[154] A. A. Voronov, I. K. Vladimir, V. K. Yurii, I. L. Aleksandr, P. P. k. Yu, K. S. Ya, and M. P. Frolov, "A continuous-wave Fe^{2+}: ZnSe laser," *Quantum Electronics*, **38**. 1113, (2008).